

## Chapter 7

# Structure at the Nano Scale

### 7.1 Microparticle Characterization via Confocal Microscopy<sup>1</sup>

#### 7.1.1 A brief history of confocal microscopy

Confocal microscopy was invented by Marvin Minsky (FIGURE) in 1957, and subsequently patented in 1961. Minsky was trying to study neural networks to understand how brains learn, and needed a way to image these connections in their natural state (in three dimensions). He invented the confocal microscope in 1955, but its utility was not fully realized until technology could catch up. In 1973 Egger published the first recognizable cells, and the first commercial microscopes were produced in 1987.



**Figure 7.1:** American cognitive scientist in the field of artificial intelligence Marvin Lee Minsky (1927 - ).

---

In the 1990's confocal microscopy became near routine due to advances in laser technology, fiber optics, photodetectors, thin film dielectric coatings, computer processors, data storage, displays, and fluorophores. Today, confocal microscopy is widely used in life sciences to study cells and tissues.

<sup>1</sup>This content is available online at <<http://cnx.org/content/m34540/1.4/>>.

### 7.1.2 The basics of fluorescence

Fluorescence is the emission of a secondary photon upon absorption of a photon of higher wavelength. Most molecules at normal temperatures are at the lowest energy state, the so-called 'ground state'. Occasionally, a molecule may absorb a photon and increase its energy to the *excited state*. From here it can very quickly transfer some of that energy to other molecules through collisions; however, if it cannot transfer enough energy it spontaneously emits a photon with a lower wavelength Figure 7.2. This is fluorescence.

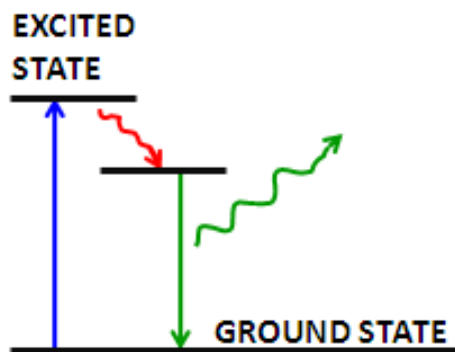


**Figure 7.2:** An energy diagram shows the principle of fluorescence. A molecule absorbs a high energy photon (blue) which excites the molecule to a higher energy state. The molecule then dissipates some of the extra energy via molecular collisions (red), and emits the remaining energy by emitting a photon (green) to return to the ground state.

In fluorescence microscopy, fluorescent molecules are designed to attach to specific parts of a sample, thus identifying them when imaged. Multiple fluorophores can be used to simultaneously identify different parts of a sample. There are two options when using multiple fluorophores:

- Fluorophores can be chosen that respond to different wavelengths of a multi-line laser.
- Fluorophores can be chosen that respond to the same excitation wavelength but emit at different wavelengths.

In order to increase the signal, more fluorophores can be attached to a sample. However, there is a limit, as high fluorophore concentrations result in them quenching each other, and too many fluorophores near the surface of the sample may absorb enough light to limit the light available to the rest of the sample. While the intensity of incident radiation can be increased, fluorophores may become saturated if the intensity is too high.

Photobleaching is another consideration in fluorescent microscopy. Fluorophores irreversibly fade when exposed to excitation light. This may be due to reaction of the molecules' excited state with oxygen or oxygen radicals. There has been some success in limiting photobleaching by reducing the oxygen available or by using free-radical scavengers. Some fluorophores are more robust than others, so choice of fluorophore is very important. Fluorophores today are available that emit photons with wavelengths ranging 400 - 750 nm.

### 7.1.3 How confocal microscopy is different from optical microscopy

A microscope's lenses project the sample plane onto an image plane. An image can be formed at many image planes; however, we only consider one of these planes to be the 'focal plane' (when the sample image

is in focus). When a pinhole screen is placed at the image focal point, it allows in-focus light to pass while effectively blocking light from out-of-focus locations Figure 7.3. This pinhole is placed at the conjugate image plane to the focal plane, thus the name "confocal". The size of this pinhole determines the depth-of-focus; a bigger pinhole collects light from a larger volume. The pinhole can only practically be made as small as approximately the radius of the Airy disk, which is the best possible light spot from a circular aperture Figure 7.4, because beyond that more signal is blocked resulting in a decreased signal-to-noise ratio.

NOTE: In optics, the Airy disk and Airy pattern are descriptions of the best focused spot of light that a perfect lens with a circular aperture can make, limited by the diffraction of light.

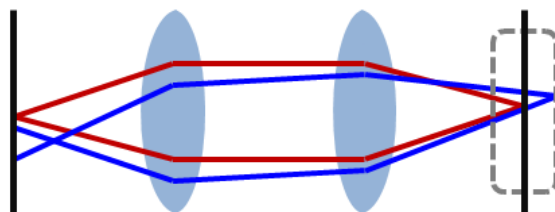


**Figure 7.3:** A schematic of a simplified microscope objective. Red and blue lines represent light rays refracted through the objective, indicating the focal points and corresponding image points.

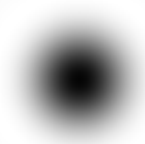


**Figure 7.4:** A representation of an Airy disk. An intense peak of light forms at the middle, surrounded by rings of lower intensity formed due to the diffraction of light. Adapted with permission from *Confocal Microscopy*, Eric Weeks

To further reduce the effect of scattering due to light from other parts of the sample, the sample is only illuminated at a tiny point through the use of a pinhole in front of the light source. This greatly reduces the interference of scattered light from other parts of the sample. The combination of a pinhole in front of both the light source and detector is what makes confocal unique.

### 7.1.4 Parts of a confocal microscope

A simple confocal microscope generally consists of a laser, pinhole aperture, dichromatic mirror, scanning mirrors, microscope objectives, a photomultiplier tube, and computing software used to reconstruct the image Figure 7.5. Because a relatively small volume of the sample is being illuminated at any given time, a very bright light source must be used to produce a detectable signal. Early confocal microscopes used zirconium arc lamps, but recent advances in laser technology have made lasers in the UV-visible and infrared more stable and affordable. A laser allows for a monochromatic (narrow wavelength range) light source that can be used to selectively excite fluorophores to emit photons of a different wavelength. Sometimes filters are used to further screen for single wavelengths.

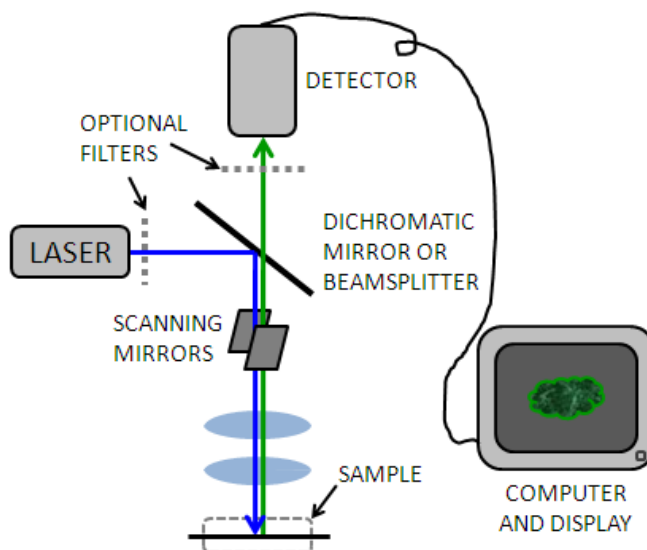


**Figure 7.5:** A schematic of a confocal microscope. Rays represent the path of light from source to detector.

The light passes through a dichromatic (or "dichroic") mirror Figure 7.5 which allows light with a higher wavelength (from the laser) to pass but reflects light of a lower wavelength (from the sample) to the detector. This allows the light to travel the same path through the majority of the instrument, and eliminates signal due to reflection of the incident light.

The light is then reflects across a pair of mirrors or crystals, one each for the  $x$  and  $y$  directions, which enable the beam to scan across the sample (Figure 7.5 ). The speed of the scan is usually the limiting factor in the speed of image acquisition. Most confocal microscopes can create an image in 0.1 - 1 second. Usually the sample is raster scanned quickly in the  $x$ -direction and slowly in the  $y$  direction (like reading a paragraph left to right, Figure 7.6).

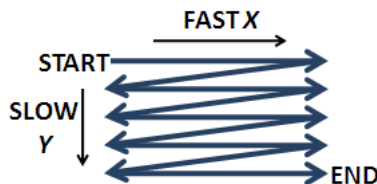


**Figure 7.6:** Raster scanning is usually performed quickly in the  $x$  direction, line-by-line. Other scanning patterns are also used, but this is most common.

The rastering is controlled by galvanometers that move the mirrors back and forth in a sawtooth motion. The disadvantage to scanning with the light beam is that the angle of light hitting the sample changes. Fortunately, this change is small. Interestingly, Minsky's original design moved the stage instead of the beam, as it was difficult to maintain alignment of the sensitive optics. Despite the obvious disadvantages of moving a bulky specimen, there are some advantages of moving the stage and keeping the optics stationary:

- The light illuminates the specimen axially everywhere circumventing optical aberrations, and
- The field of view can be made much larger by controlling the amplitude of the stage movements.

An alternative to light-reflecting mirrors is the acousto-optic deflector (AOD). The AOD allows for fast  $x$ -direction scans by creating a diffraction grating from high-frequency standing sound (pressure) waves which locally change the refractive index of a crystal. The disadvantage to AODs is that the amount of deflection depends on the wavelength, so the emission light cannot be descanned (travel back through the same path as the excitation light). The solution to this is to descann only in the  $y$  direction controlled by the slow galvanometer and collect the light in a slit instead of a pinhole. This results in reduced optical sectioning and slight distortion due to the loss of radial symmetry, but good images can still be formed. Keep in mind this is not a problem for reflected light microscopy which has the same wavelength for incident and reflected light!

Another alternative is the Nipkow disk, which has a spiral array of pinholes that create the simultaneous sampling of many points in the sample. A single rotation covers the entire specimen several times over (at 40 revolutions per second, that's over 600 frames per second). This allows descanning, but only about 1% of the excitation light passes through. This is okay for reflected light microscopy, but the signal is relatively weak and signal-to-noise ratio is low. The pinholes could be made bigger to increase light transmission but then the optical sectioning is less effective (remember depth of field is dependent on the diameter of the pinhole) and  $xy$  resolution is poorer. Highly responsive, efficient fluorophores are needed with this method.

Returning to the confocal microscope (Figure 7.5), light then passes through the objective which acts as a well-corrected condenser and objective combination. The illuminated fluorophores fluoresce and emitted light travels up the objective back to the dichromatic mirror. This is known as epifluorescence when the incident light has the same path as detected light. Since the emitted light now has a lower wavelength than the incident, it cannot pass through the dichromatic mirror and is reflected to the detector. When using reflected light, a beamsplitter is used instead of a dichromatic mirror. Fluorescence microscopy when used properly can be more sensitive than reflected light microscopy.

Though the signal's position is well-defined according to the position of the  $xy$  mirrors, the signal from fluorescence is relatively weak after passing through the pinhole, so a photomultiplier tube is used to detect emitted photons. Detecting all photons without regard to spatial position increases the signal, and the photomultiplier tube further increases the detection signal by propagating an electron cascade resulting from the photoelectric effect (incident photons kicking off electrons). The resulting signal is an analog electrical

signal with continuously varying voltage that corresponds to the emission intensity. This is periodically sampled by an analog-to-digital converter.

It is important to understand that the image is a reconstruction of many points sampled across the specimen. At any given time the microscope is only looking at a tiny point, and no complete image exists that can be viewed at an instantaneous point in time. Software is used to recombine these points to form an image plane, and combine image planes to form a 3-D representation of the sample volume.

### 7.1.5 Two-photon microscopy

Two-photon microscopy is a technique whereby two beams of lower intensity are directed to intersect at the focal point. Two photons can excite a fluorophore if they hit it at the same time, but alone they do not have enough energy to excite any molecules. The probability of two photons hitting a fluorophore at nearly the exact same time (less than  $10^{-16}$ ) is very low, but more likely at the focal point. This creates a bright point of light in the sample without the usual cone of light above and below the focal plane, since there are almost no excitations away from the focal point.

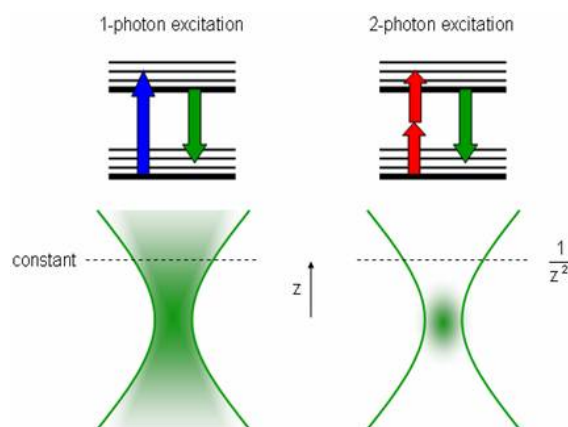


**Figure 7.7:** Schematic representation of the difference between single photon and two photon microscopy. Copyright: J. Mertz, Boston University.

To increase the chance of absorption, an ultra-fast pulsed laser is used to create quick, intense light pulses. Since the hourglass shape is replaced by a point source, the pinhole near the detector (used to reduce the signal from light originating from outside the focal plane) can be eliminated. This also increases the signal-to-noise ratio (here is very little noise now that the light source is so focused, but the signal is also small). These lasers have lower average incident power than normal lasers, which helps reduce damage to the surrounding specimen. This technique can image deeper into the specimen ( $\sim 400 \mu\text{m}$ ), but these lasers are still very expensive, difficult to set up, require a stronger power supply, intensive cooling, and must be aligned in the same optical table because pulses can be distorted in optical fibers.

### 7.1.6 Microparticle characterization

Confocal microscopy is very useful for determining the relative positions of particles in three dimensions Figure 7.8. Software allows measurement of distances in the 3D reconstructions so that information about spacing can be ascertained (such as packing density, porosity, long range order or alignment, etc.).

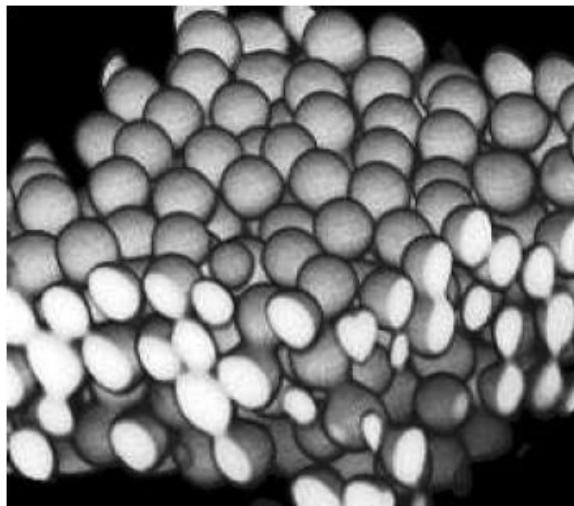


**Figure 7.8:** A reconstruction of a colloidal suspension of poly(methyl methacrylate) (PMMA) microparticles approximately 2 microns in diameter. Adapted from *Confocal Microscopy of Colloids*, Eric Weeks.

---

If imaging in fluorescence mode, remember that the signal will only represent the locations of the individual fluorophores. There is no guarantee fluorophores will completely attach to the structures of interest or that there will not be stray fluorophores away from those structures. For microparticles it is often possible to attach the fluorophores to the shell of the particle, creating hollow spheres of fluorophores. It is possible to tell if a sample sphere is hollow or solid but it would depend on the transparency of the material.

Dispersions of microparticles have been used to study nucleation and crystal growth, since colloids are much larger than atoms and can be imaged in real-time. Crystalline regions are determined from the order of spheres arranged in a lattice, and regions can be distinguished from one another by noting lattice defects.

Self-assembly is another application where time-dependent, 3-D studies can help elucidate the assembly process and determine the position of various structures or materials. Because confocal is popular for biological specimens, the position of nanoparticles such as quantum dots in a cell or tissue can be observed. This can be useful for determining toxicity, drug-delivery effectiveness, diffusion limitations, etc.

### 7.1.7 A summary of confocal microscopy's strengths and weaknesses

#### Strengths

- Less haze, better contrast than ordinary microscopes.
- 3-D capability.
- Illuminates a small volume.
- Excludes most of the light from the sample not in the focal plane.
- Depth of field may be adjusted with pinhole size.
- Has both reflected light and fluorescence modes.
- Can image living cells and tissues.
- Fluorescence microscopy can identify several different structures simultaneously.
- Accommodates samples with thickness up to 100  $\mu\text{m}$ .
- Can use with two-photon microscopy.

- Allows for optical sectioning (no artifacts from physical sectioning) 0.5 - 1.5  $\mu\text{m}$ .

#### Weakness

- Images are scanned slowly (one complete image every 0.1-1 second).
- Must raster scan sample, no complete image exists at any given time.
- There is an inherent resolution limit because of diffraction (based on numerical aperture,  $\sim 200$  nm).
- Sample should be relatively transparent for good signal.
- High fluorescence concentrations can quench the fluorescent signal.
- Fluorophores irreversibly photobleach.
- Lasers are expensive.
- Angle of incident light changes slightly, introducing slight distortion.

### 7.1.8 Bibliography

- P. Davidovits and M. D. Egger, *Nature*, 1973, **244**, 366.
- A. Hibbs, *Confocal Microscopy for Biologists*, Twayne Publishers, Boston (2004).
- M. Minsky, *Scanning*, 1988, **10**, 128.
- J. Pawley, *Handbook of Biological Confocal Microscopy*, Twayne Publishers, Boston (2006).
- V. Prasad, D. Semwogerere, and E.R. Weeks, *J. Phys.: Condens. Matter*, 2007, **19**, 113102.
- D. Semwogerere and E. R. Weeks, *Encyclopedia of Biomaterials and Biomedical Engineering Confocal Microscopy*, Taylor Francis (2005).
- C. Sheppard, *Confocal Laser Scanning Microscopy*, Twayne Publishers, Boston (1997).

## 7.2 Transmission Electron Microscopy

### 7.2.1 Transmission Electron Microscopy: An Overview<sup>2</sup>

Transmission electron microscopy (TEM) is a form of microscopy in which a beam of electrons transmits through an extremely thin specimen, and then interacts with the specimen when passing through it. The formation of images in a TEM can be explained by an optical electron beam diagram in Figure 7.9. TEMs provide images with significantly higher resolution than visible-light microscopes (VLMs) do because of the smaller de Broglie wavelength of electrons. These electrons allow for the examination of finer details, which are several thousand times higher than the highest resolution in a VLM. Nevertheless, the magnification provided in a TEM image is in contrast to the absorption of the electrons in the material, which is primarily due to the thickness or composition of the material.

---

<sup>2</sup>This content is available online at <http://cnx.org/content/m34523/1.1/>.

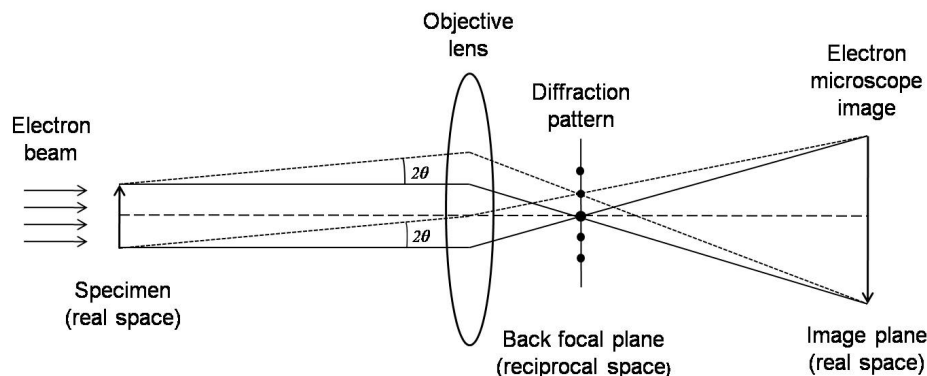


**Figure 7.9:** The optical electron beam diagram of TEM.

When a crystal lattice spacing ( $d$ ) is investigated with electrons with wavelength  $\lambda$ , diffracted waves will be formed at specific angles  $2\theta$ , satisfying the Bragg condition, (7.1).

$$2d\sin\theta = \lambda \quad (7.1)$$

The regular arrangement of the diffraction spots, the so-called diffraction pattern (DP), can be observed. While the transmitted and the diffracted beams interfere on the image plane, a magnified image (electron microscope image) appears. The plane where the DP forms is called the *reciprocal space*, which the image plane is called the *real space*. A Fourier transform can mathematically transform the real space to reciprocal space.

By adjusting the lenses (changing their focal lengths), both electron microscope images and DP can be observed. Thus, both observation modes can be successfully combined in the analysis of the microstructures of materials. For instance, during investigation of DPs, an electron microscope image is observed. Then, by inserting an aperture (selected area aperture), adjusting the lenses, and focusing on a specific area that we are interested in, we will get a DP of the area. This kind of observation mode is called a *selected area diffraction*. In order to investigate an electron microscope image, we first observe the DP. Then by passing the transmitted beam or one of the diffracted beams through a selected aperture and changing to the imaging mode, we can get the image with enhanced contrast, and precipitates and lattice defects can easily be identified.

Describing the resolution of a TEM in terms of the classic Rayleigh criterion for VLMs, which states that the smallest distance that can be investigated,  $\delta$ , is given approximately by (7.2), where  $\lambda$  is the wavelength of the electrons,  $\mu$  is the refractive index of the viewing medium, and  $\beta$  is the semi-angle of collection of the magnifying lens.

$$\delta = \frac{0.61\lambda}{\mu \sin\beta} \quad (7.2)$$

According to de Broglie's ideas of the wave-particle duality, the particle momentum  $p$  is related to its wavelength  $\lambda$  through Planck's constant  $h$ , (7.3).

$$\lambda = \frac{h}{p} \quad (7.3)$$

Momentum is given to the electron by accelerating it through a potential drop,  $V$ , giving it a kinetic energy,

eV. This potential energy is equal to the kinetic energy of the electron, (7.4).

$$eV = \frac{m_o v^2}{2} \quad (7.4)$$

Based upon the foregoing, we can equate the momentum ( $p$ ) to the electron mass ( $m_o$ ), multiplied by the velocity ( $v$ ) and substituting for  $v$  from (7.4), i.e., (7.5).

$$p = m_o v = (2m_o eV)^{\frac{1}{2}} \quad (7.5)$$

These equations define the relationship between the electron wavelength,  $\lambda$ , and the accelerating voltage of the electron microscope ( $V$ ), Eq. However, we have to consider about the relative effects when the energy of electron more than 100 keV. So in order to be exact we must modify (7.6) to give (7.7).

$$\lambda = \frac{h}{(2m_o eV)^{\frac{1}{2}}} \quad (7.6)$$

$$\lambda = \frac{h}{\left[2m_o eV \left(1 + \frac{eV}{2m_o e^2}\right)\right]^{\frac{1}{2}}} \quad (7.7)$$

From (7.2) and (7.7), if a higher resolution is desired a decrease in the electron wavelength is accomplished by increasing the accelerating voltage of the electron microscope. In other words, the higher accelerating rating used, the better resolution obtained.

### 7.2.1.1 Why the specimen should be thin

The scattering of the electron beam through the material under study can form different angular distribution (Figure 7.10) and it can be either forward scattering or back scattering. If an electron is scattered  $< 90^\circ$ , then it is forward scattered, otherwise, it is backscattered. If the specimen is thicker, fewer electrons are forward scattered and more are backscattered. Incoherent, backscattered electrons are the only remnants of the incident beam for bulk, non-transparent specimens. The reason that electrons can be scattered through different angles is related to the fact that an electron can be scattered more than once. Generally, the more times of scattering happen, the greater the angle of scattering.

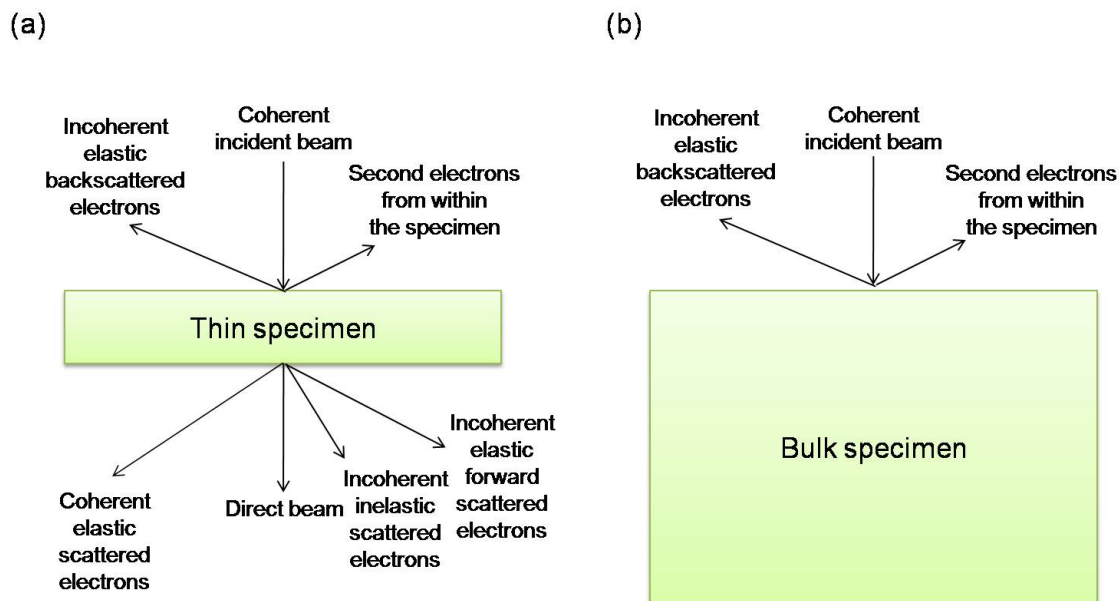


Figure 7.10: Two different kinds of electron scattering form (a) a thin specimen and (b) a bulk specimen.

All scattering in the TEM specimen is often approximated as a single scattering event since it is the simplest process. If the specimen is very thin, this assumption will be reasonable enough. If the electron is scattered more than once, it is called ‘plural scattering.’ It is generally safe to assume single scattering occurs, unless the specimen is particularly thick. When the times of scattering increase, it is difficult to predict what will happen to the electron and to interpret the images and DPs. So, the principle is ‘thinner is better’, i.e., if we make thin enough specimens so that the single-scattering assumption is plausible, and the TEM research will be much easier.

In fact, forward scattering includes the direct beam, most elastic scattering, refraction, diffraction, particularly Bragg diffraction, and inelastic scattering. Because of forward scattering through the thin specimen, a DP or an image would be showed on the viewing screen, and an X-ray spectrum or an electron energy-loss spectrum can be detected outside the TEM column. However, backscattering still cannot be ignored, it is an important imagine mode in the SEM.

## 7.2.1.2 Limitations of TEM

### 7.2.1.2.1 Interpreting transmission images

One significant problem that might encounter when TEM images are analyzed is that the TEM present us with 2D images of a 3D specimen, viewed in transmission. This problem can be illustrated by showing a picture of two rhinos side by side such that the head of one appears attached to the rear of the other (Figure 7.11).

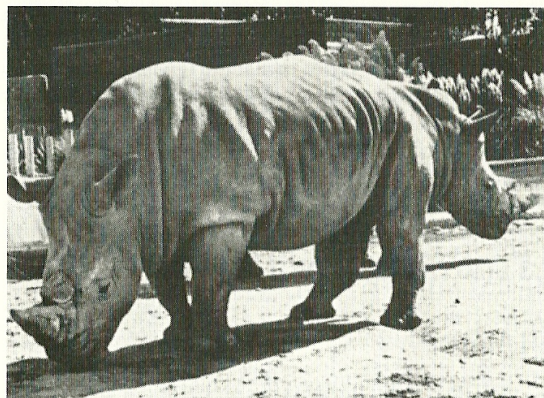


**Figure 7.11:** In projection, this photograph of two rhinos appears as one two-headed beast, because sometimes people have difficulty to translate a 2D image to a 3D image. Adapted from D. B. Williams and C. B. Carter, *Transmission Electron Microscopy: A Textbook for Material Science*, 2<sup>nd</sup> Ed., Springer, New York (2009).

---

One aspect of this particular drawback is that a single TEM images has no depth sensitivity. There often is information about the top and bottom surfaces of the specimen, but this is not immediately apparent. There has been progress in overcoming this limitation, by the development of electron tomography, which uses a sequence of images taken at different angles. In addition, there has been improvement in specimen-holder design to permit full  $360^\circ$  rotation and, in combination with easy data storage and manipulation; nanotechnologists have begun to use this technique to look at complex 3D inorganic structures such as porous materials containing catalyst particles.

#### 7.2.1.2.2 Electron beam damage

A detrimental effect of ionizing radiation is that it can damage the specimen, particularly polymers (and most organics) or certain minerals and ceramics. Some aspects of beam damage made worse at higher voltages. Figure 7.12 shows an area of a specimen damaged by high-energy electrons. However, the combination of more intense electron sources with more sensitive electron detectors, and the use computer enhancement of noisy images, can be used to minimize the total energy received by the sample.

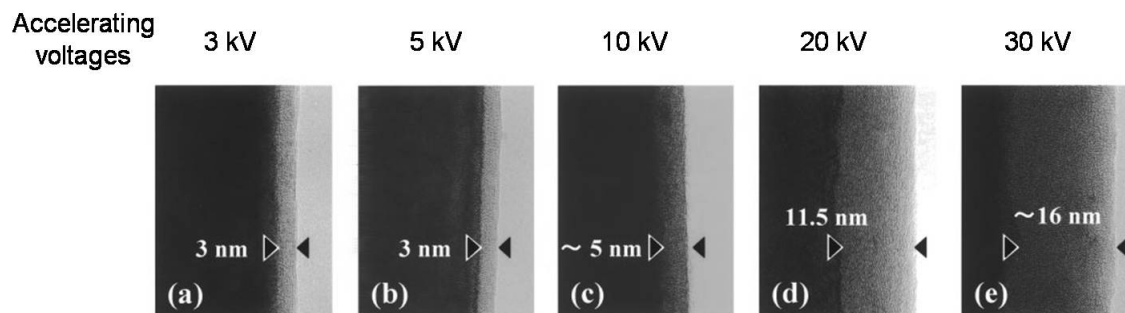


**Figure 7.12:** High-resolution TEM images at the slit edge of the GaAs samples prepared by slit focused ion beam. GaAs samples prepared at (a) 3 kV, (b) 5 kV, (c) 10 kV, (d) 20 kV, and (e) 30 kV. The thickness of the amorphous layer produced by focused ion beam is shown in each image. Adapted from Y. Yabuuchi, S. Tametou, T. Okano, S. Inazato, S. Sadaayamn, and Y. Tamamoto, *J. Electron Microsc.*, 2004, **53**, 5.

### 7.2.1.3 Sample preparation

The specimens under study have to be thin if any information is to be obtained using transmitted electrons in the TEM. For a sample to be transparent to electrons, the sample must be thin enough to transmit sufficient electrons such that enough intensity falls on the screen to give an image. This is a function of the electron energy and the average atomic number of the elements in the sample. Typically for 100 keV electrons, a specimen of aluminum alloy up to  $\sim 1 \mu\text{m}$  would be thin, while steel would be thin up to about several hundred nanometers. However, thinner is better and specimens  $< 100 \text{ nm}$  should be used wherever possible.

The method to prepare the specimens for TEM depends on what information is required. In order to observe TEM images with high resolution, it is necessary to prepare thin films without introducing contamination or defects. For this purpose, it is important to select an appropriate specimen preparation method for each material, and to find an optimum condition for each method.

#### 7.2.1.3.1 Crushing

A specimen can be crushed with an agate mortar and pestle. The flakes obtained are suspended in an organic solvent (e.g., acetone), and dispersed with a sonic bath or simply by stirring with a glass stick. Finally, the solvent containing the specimen flakes is dropped onto a grid. This method is limited to materials which tend to cleave (e.g., mica).

#### 7.2.1.3.2 Electropolishing

Slicing a bulk specimen into wafer plates of about 0.3 mm thickness by a fine cutter or a multi-wire saw. The wafer is further thinned mechanically down to about 0.1 mm in thickness. Electropolishing is performed in a specific electrolyte by supplying a direct current with the positive pole at the thin plate and the negative pole at a stainless steel plate. In order to avoid preferential polishing at the edge of the specimen, all the edges are covered with insulating paint. This is called the window method. The electropolishing is finished when there is a small hole in the plate with very thin regions around it (Figure 7.13). This method is mainly used to prepare thin films of metals and alloys.

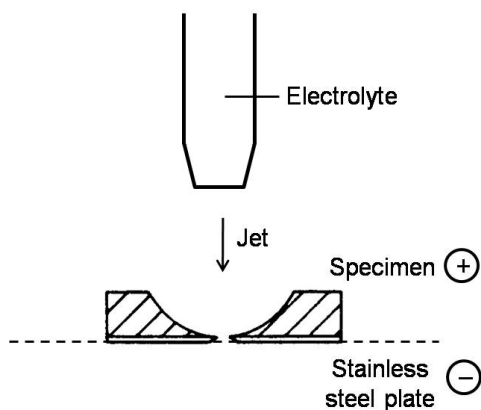


**Figure 7.13:** Principle of jet electropolishing method. The specimen and the stainless steel plate is electronic positive and negative, respectively.

#### 7.2.1.3.3 Chemical polishing

Thinning is performed chemically, i.e., by dipping the specimen in a specific solution. As for electropolishing, a thin plate of 0.1~0.2 mm in thickness should be prepared in advance. If a small dimple is made in the center of the plate with a dimple grinder, a hole can be made by etching around the center while keeping the edge of the specimen relatively thick. This method is frequently used for thinning semiconductors such as silicon. As with electro-polishing, if the specimen is not washed properly after chemical etching, contamination such as an oxide layer forms on the surface.

#### 7.2.1.3.4 Ultramicrotomy

Specimens of thin films or powders are usually fixed in an acrylic or epoxy resin and trimmed with a glass knife before being sliced with a diamond knife. This process is necessary so that the specimens in the resin can be sliced easily by a diamond knife. Acrylic resins are easily sliced and can be removed with chloroform after slicing. When using an acrylic resin, a gelatin capsule is used as a vessel. Epoxy resin takes less time to solidify than acrylic resins, and they remain strong under electron irradiation. This method has been used for preparing thin sections of biological specimens and sometimes for thin films of inorganic materials which are not too hard to cut.

#### 7.2.1.3.5 Ion milling

A thin plate (less than 0.1 mm) is prepared from a bulk specimen by using a diamond cutter and by mechanical thinning. Then, a disk 3 mm in diameter is made from the plate using a diamond knife or a ultrasonic cutter, and a dimple is formed in the center of the surface with a dimple grinder. If it is possible to thin the disk directly to 0.03 mm in thickness by mechanical thinning without using a dimple grinder, the disk should be strengthened by covering the edge with a metal ring. Ar ions are usually used for the sputtering, and the incidence angle against the disk specimen and the accelerating voltage are set as 10 - 20° and a few kilovolts, respectively. This method is widely used to obtain thin regions of ceramics and semiconductors in particular, and also for cross section of various multilayer films.

### 7.2.1.3.6 Focused ion beam (FIB)

This method was originally developed for the purpose of fixing semiconductor devices. In principle, ion beams are sharply focused on a small area, and the specimen is thinned very rapidly by sputtering. Usually Ga ions are used, with an accelerating voltage of about 30 kV and a current of about 10 A/cm<sup>2</sup>. The probe size is several tens of nanometers. This method is useful for specimens containing a boundary between different materials, where it may be difficult to homogeneously thin the boundary region by other methods such as ion milling.

### 7.2.1.3.7 Vacuum evaporation

The specimen to be studied is set in a tungsten-coil or basket. Resistance heating is applied by an electric current passing through the coil or basket, and the specimen is melted, then evaporated (or sublimed), and finally deposited onto a substrate. The deposition process is usually carried under a pressure of 10<sup>-3</sup>-10<sup>-4</sup> Pa, but in order to avoid surface contamination, a very high vacuum is necessary. A collodion film or cleaved rock salt is used as a substrate. Rock salt is especially useful in forming single crystals with a special orientation relationship between each crystal and the substrate. Salt is easily dissolved in water, and then the deposited films can be fixed on a grid. Recently, as an alternative to resistance heating, electron beam heating or an ion beam sputtering method has been used to prepare thin films of various alloys. This method is used for preparing homogeneous thin films of metals and alloys, and is also used for coating a specimen with the metal of alloy.

### 7.2.1.3.8 The characteristics of the grid

The types of TEM specimens that are prepared depend on what information is needed. For example, a self-supporting specimen is one where the whole specimen consists of one material (which may be a composite). Other specimens are supported on a grid or on a Cu washer with a single slot. Some grids are shown in Figure 7.14. Usually the specimen or grid will be 3 mm in diameter.

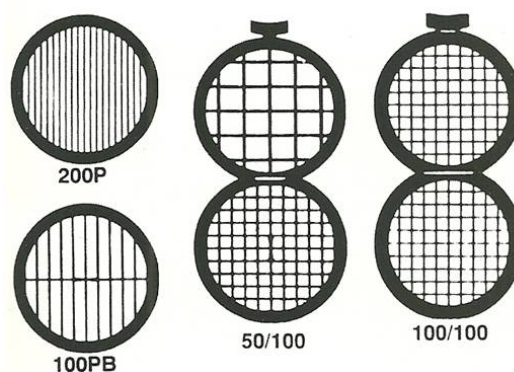


**Figure 7.14:** TEM sample support mesh grids. A diameter of a grid is usually 3.05 mm, however, some grids with diameters of 2.30 mm are also be used for earlier microscopes. Adapted from D. B. Williams and C. B. Carter, *Transmission Electron Microscopy: A Textbook for Material Science*, 2<sup>nd</sup> Ed., Springer, New York (2009).

TEM specimen stage designs include airlocks to allow for insertion of the specimen holder into the vacuum with minimal increase in pressure in other areas of the microscope. The specimen holders are adapted to

hold a standard size of grid upon which the sample is placed or a standard size of self-supporting specimen. Standard TEM grid sizes is a 3.05 mm diameter ring, with a thickness and mesh size ranging from a few to 100  $\mu\text{m}$ . The sample is placed onto the inner meshed area having diameter of approximately 2.5 mm. The grid materials usually are copper, molybdenum, gold or platinum. This grid is placed into the sample holder which is paired with the specimen stage. A wide variety of designs of stages and holders exist, depending upon the type of experiment being performed. In addition to 3.05 mm grids, 2.3 mm grids are sometimes, if rarely, used. These grids were particularly used in the mineral sciences where a large degree of tilt can be required and where specimen material may be extremely rare. Electron transparent specimens have a thickness around 100 nm, but this value depends on the accelerating voltage.

Once inserted into a TEM, the sample is manipulated to allow study of the region of interest. To accommodate this, the TEM stage includes mechanisms for the translation of the sample in the XY plane of the sample, for Z height adjustment of the sample holder, and usually at least one rotation degree of freedom. Most TEMs provide the ability for two orthogonal rotation angles of movement with specialized holder designs called double-tilt sample holders.

A TEM stage is required to have the ability to hold a specimen and be manipulated to bring the region of interest into the path of the electron beam. As the TEM can operate over a wide range of magnifications, the stage must simultaneously be highly resistant to mechanical drift as low as a few nm/minute while being able to move several  $\mu\text{m}$ /minute, with repositioning accuracy on the order of nanometers.

#### 7.2.1.4 Bibliography

- D. B. Williams and C. B. Carter, *Transmission Electron Microscopy: A Textbook for Material Science*, 2<sup>nd</sup> Ed., Springer, New York (2009).
- D. Shindo and K. Hiraga, *High-Resolution Electron Microscopy for Material Science*, Springer, New York (1998).
- L. Reimer and H. Kohl, *Transmission Electron Microscopy Physics of Image Formation*, 5<sup>th</sup> Ed., Springer, New York (2008).
- D. L. Spector and R. D. Goldman, *Basic Methods in Microscopy Protocols and Concepts from Cells: A Laboratory Manual*, Cold Spring Harbor, New York (2006).
- Y. Yabuuchi, S. Tametou, T. Okano, S. Inazato, S. Sadayamn, and Y. Tamamoto, *J. Electron Microsc.*, 2004, **53**, 5.

### 7.2.2 Transmission Electron Microscopy Image for Multilayer-Nanomaterials<sup>3</sup>

Although, TEMs can only provide 2D analysis for a 3D specimen; magnifications of 300,000 times can be routinely obtained for many materials making it an ideal method for the study of nanomaterials. Besides from the TEM images, darker areas of the image show that the sample is thicker or denser in these areas, so we can observe the different components and structures of the specimen by the difference of color. For investigating multilayer-nanomaterials, a TEM is usually the first choice, because not only does it provide a high resolution image for nanomaterials but also it can distinguish each layer within a nanostructured material.

#### 7.2.2.1 Observations of multilayer-nanomaterials

TEM was been used to analyze the depth-graded W/Si multilayer films. Multilayer films were grown on polished, 100 mm thick Si wafers by magnetron sputtering in argon gas. The individual tungsten and silicon layer thicknesses in periodic and depth-graded multilayers are adjusted by varying the computer-controlled rotational velocity of the substrate platen. The deposition times required to produce specific layer thicknesses were determined from detailed rate calibrations. Samples for TEM were prepared by focused ion

<sup>3</sup>This content is available online at <<http://cnx.org/content/m34524/1.1/>>.

beam milling at liquid N<sub>2</sub> temperature to prevent any beam heating which might result in re-crystallization and/or re-growth of any amorphous or fine grained polycrystalline layers in the film.

TEM measurements were made using a JEOL-4000 high-resolution transmission electron microscope operating at 400 keV; this instrument has a point-to-point resolution of 0.16 nm. Large area cross-sectional images of a depth-graded multilayer film obtained under medium magnification (~100 kX) were acquired at high resolution. A cross-sectional TEM image showed 150 layers W/Si film with the thickness of layers in the range of 3.33 ~ 29.6 nm (Figure 7.15 shows a part of layers). The dark layers are tungsten and the light layers are silicon and they are separated by the thin amorphous W–Si interlayers (gray bands). By the high resolution of the TEM and the nature characteristics of the material, each layer can be distinguished clearly with their different darkness.

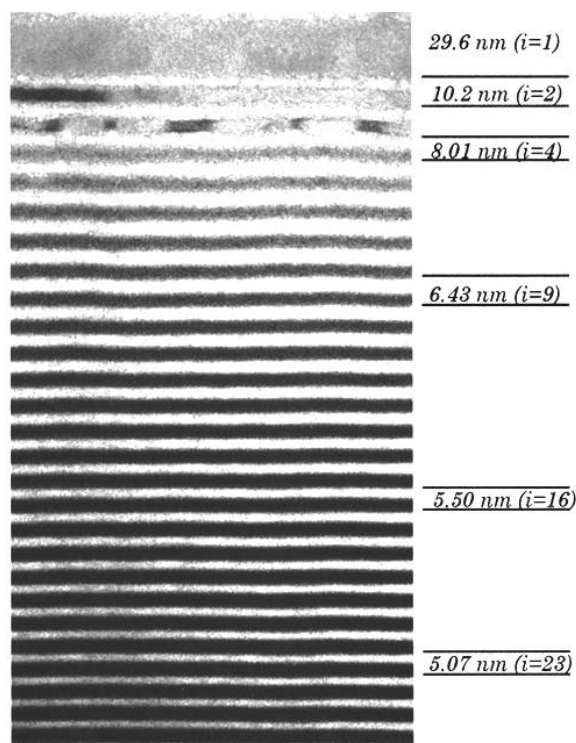


**Figure 7.15:** Cross-sectional transmission electron micrograph of the top portion of a depth-graded W/Si multilayer structure. Selected bilayer indices and thicknesses are indicated. The tungsten (dark bands) and silicon (light bands) layers are separated by thin amorphous W–Si interlayers (gray bands). The topmost silicon layer is not completely visible in this image. Adapted from D. L. Windt, F. E. Christensen, W. W. Craig, C. Hailey, F. A. Harrison, M. Jimenez-Garate, R. Kalyanaraman, and P. H. Mao, *J. Appl. Phys.*, 2000, **88**, 460.

Not all kinds of multilayer nanomaterials can be observed clearly under TEM. A materials consist of pc-Si:H multilayers were prepared by a photo-assisted chemical vapor deposition (photo-CVD) using a low-pressure mercury lamp as an UV light source to dissociate the gases. The pc-Si:H multilayer included low H<sub>2</sub>-diluted a-Si:H sublayers (SL's) and highly H<sub>2</sub>-diluted a-Si:H sublayers (SH's). Control of the CVD gas flow (H<sub>2</sub>|SiH<sub>4</sub>) under continuous UV irradiation resulted in the deposition of multilayer films layer by layer.

For a TEM measurement, a 20 nm thick undiluted a-Si:H film on a c-Si wafer before the deposition

of multilayer to prevent from any epitaxial growth. Figure 7.16 shows a cross-sectional TEM image of a six-cycled pc-Si:H multilayer specimen. The white dotted lines are used to emphasize the horizontal stripes, which have periodicity in the TEM image. As can be seen, there are no significant boundaries between SL and SH could be observed because all sublayers are prepared in  $H_2$  gas. In order to get the more accurate thickness of each sublayer, other measurements might be necessary.

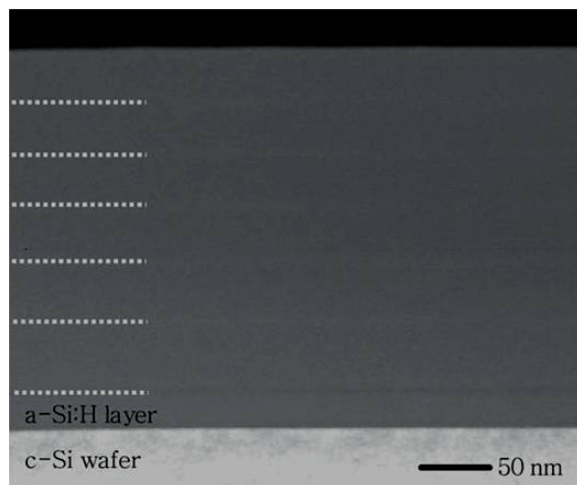


**Figure 7.16:** Cross-sectional TEM image of a 6-cycled pc-Si:H multilayer. Before the multilayer deposition, a 20 nm thick a-Si:H was deposited on a c-Si substrate. Adapted from S. W. Kwon, J. Kwak, S. Y. Myong, and K. S. Lim, *J. Non-Cryst. Solid*, 2006, **352**, 1132.

### 7.2.2.2 Bibliography

- D. L. Windt, F. E. Christensen, W. W. Craig, C. Hailey, F. A. Harrison, M. Jimenez-Garate, R. Kalyanaraman, and P. H. Mao, *J. Appl. Phys.*, 2000, **88**, 460.
- S. W. Kwon, J. Kwak, S. Y. Myong, and K. S. Lim, *J. Non-Cryst. Solid*, 2006, **352**, 1132.

## 7.2.3 TEM Imaging of Carbon Nanomaterials<sup>4</sup>

### 7.2.3.1 Introduction to TEM

Transmission electron microscopy (TEM) is a form of microscopy that uses an high energy electron beam (rather than optical light). A beam of electrons is transmitted through an ultra thin specimen, interacting with the specimen as it passes through. The image (formed from the interaction of the electrons with the sample) is magnified and focused onto an imaging device, such as a photographic film, a fluorescent screen, or detected by a CCD camera. In order to let the electrons pass through the specimen, the specimen has to be ultra thin, usually thinner than 10 nm.

The resolution of TEM is significantly higher than light microscopes. This is because the electron has a much smaller de Broglie wavelength than visible light (wavelength of 400~700 nm). Theoretically, the

<sup>4</sup>This content is available online at <<http://cnx.org/content/m22963/1.5/>>.

maximum resolution,  $d$ , has been limited by  $\lambda$ , the wavelength of the detecting source (light or electrons) and NA, the numerical aperture of the system.

$$d = \frac{\lambda}{2n \sin\alpha} \approx \frac{\lambda}{2NA} \quad (7.8)$$

For high speed electrons (in TEM, electron velocity is close to the speed of light,  $c$ , so that the special theory of relativity has to be considered), the  $\lambda_e$ :

$$\lambda_e = \frac{h}{\sqrt{(2m_0E(1 + E/2m_0c^2))}} \quad (7.9)$$

According to this formula, if we increase the energy of the detecting source, its wavelength will decrease, and we can get higher resolution. Today, the energy of electrons used can easily get to 200 keV, sometimes as high as 1 MeV, which means the resolution is good enough to investigate structure in sub-nanometer scale. Because the electrons is focused by several electrostatic and electromagnetic lenses, like the problems optical camera usually have, the image resolution is also limited by aberration, especially the spherical aberration called  $C_s$ . Equipped with a new generation of aberration correctors, transmission electron aberration-corrected microscope (TEAM) can overcome spherical aberration and get to half angstrom resolution.

Although TEAM can easily get to atomic resolution, the first TEM invented by Ruska in April 1932 could hardly compete with optical microscope, with only  $3.6 \times 4.8 = 14.4$  magnification. The primary problem was the electron irradiation damage to sample in poor vacuum system. After World War II, Ruska resumed his work in developing high resolution TEM. Finally, this work brought him the Nobel Prize in physics 1986. Since then, the general structure of TEM hasn't changed too much as shown in Figure 7.17. The basic components in TEM are: electron gun, condenser system, objective lens (most important len in TEM which determines the final resolution), diffraction lens, projective lenses (all lens are inside the equipment column, between apertures), image recording system (used to be negative films, now is CCD cameras) and vacuum system.

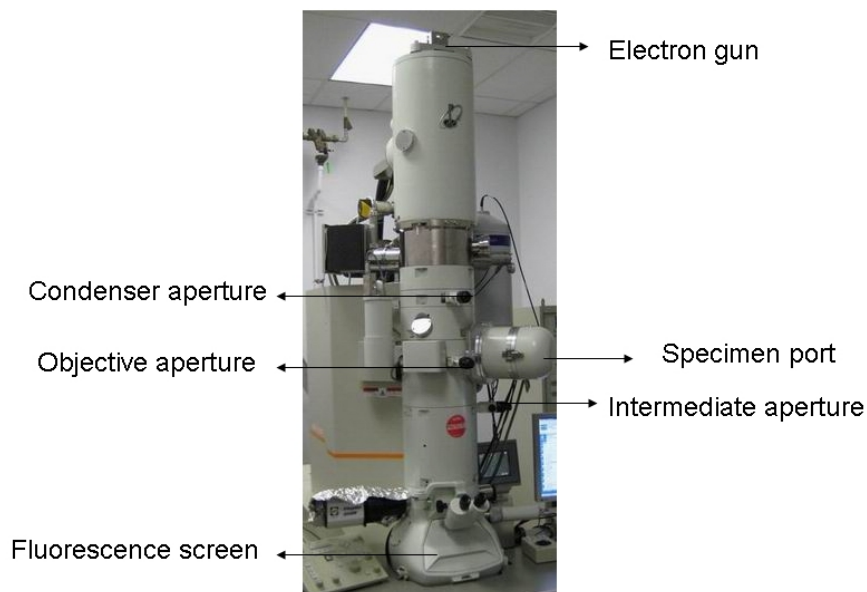


**Figure 7.17:** Position of the basic components in a TEM.

---

### 7.2.3.2 The family of carbon allotropes and carbon nanomaterials

Common carbon allotropes include diamond, graphite, amorphous C (a-C), fullerene (also known as buckyball), carbon nanotube (CNT, including single wall CNT and multi wall CNT), graphene. Most of them are chemically inert and have been found in nature. We can also define carbon as  $sp^2$  carbon (which is graphite),  $sp^3$  carbon (which is diamond) or hybrids of  $sp^2$  and  $sp^3$  carbon. As shown in Figure 7.18, (a) is the structure of diamond, (b) is the structure of graphite, (c) graphene is a single sheet of graphite, (d) is amorphous carbon, (e) is  $C_{60}$ , and (f) is single wall nanotube. As for carbon nanomaterials, fullerene, CNT and graphene are the three most well investigated, due to their unique properties in both mechanics and electronics. Under TEM, these carbon nanomaterials will display three different projected images.

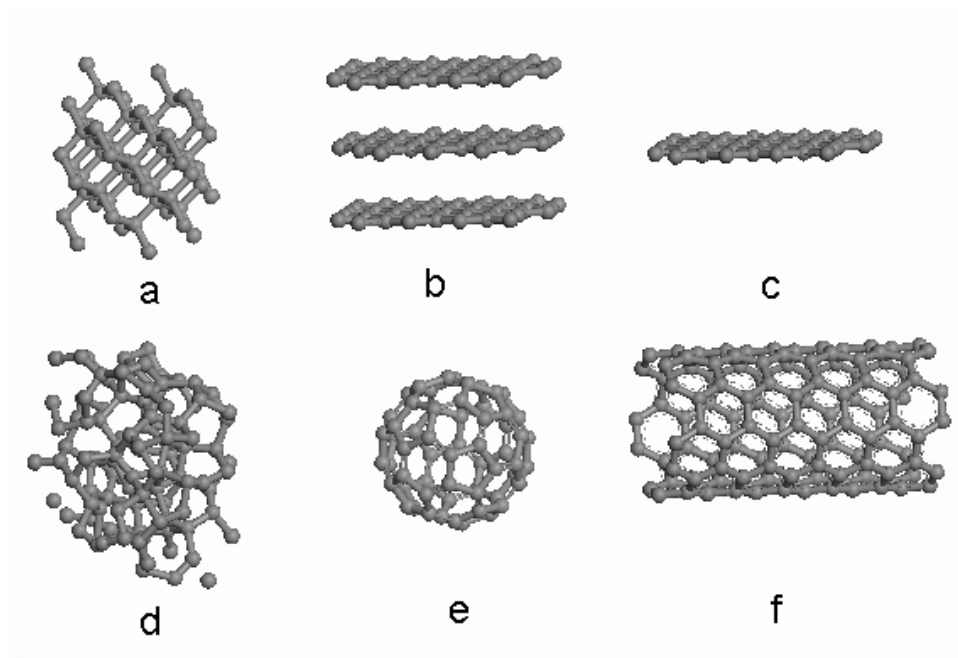


**Figure 7.18:** Six allotropes of carbon: a) diamond, b) graphite, c) graphene, d) amorphous carbon, e)  $C_{60}$  (Buckminsterfullerene or buckyball), f) single-wall carbon nanotube or buckytube.

### 7.2.3.3 Atomic structure of carbon nanomaterials under TEM

All carbon nanomaterials can be investigated under TEM. However, because of their difference in structure and shape, specific parts should be focused in order to obtain their atomic structure.

For  $C_{60}$ , which has a diameter of only 1 nm, it is relatively difficult to suspend a sample over a lacey carbon grid (a common kind of TEM grid usually used for nanoparticles). Even if the  $C_{60}$  sits on a thin a-C film, it also has some focus problems since the surface profile variation might be larger than 1 nm. One way to solve this problem is to encapsulate the  $C_{60}$  into single wall CNTs, which is known as nano peapods. This method has two benefits:

1. CNT helps focus on  $C_{60}$ . Single wall is aligned in a long distance (relative to  $C_{60}$ ). Once it is suspended on lacey carbon film, it is much easier to focus on it. Therefore, the  $C_{60}$  inside can also be caught by minor focus changes.
2. The CNT can protect  $C_{60}$  from electron irradiation. Intense high energy electrons can permanently change the structure of the CNT. For  $C_{60}$ , which is more reactive than CNTs, it can not survive after exposing to high dose fast electrons.

In studying CNT cages,  $C_{92}$  is observed as a small circle inside the walls of the CNT. While a majority of electron energy is absorbed by the CNT, the sample is still not irradiation-proof. Thus, as is seen in Figure 7.19, after a 123 s exposure, defects can be generated and two  $C_{92}$  fused into one new larger fullerene.

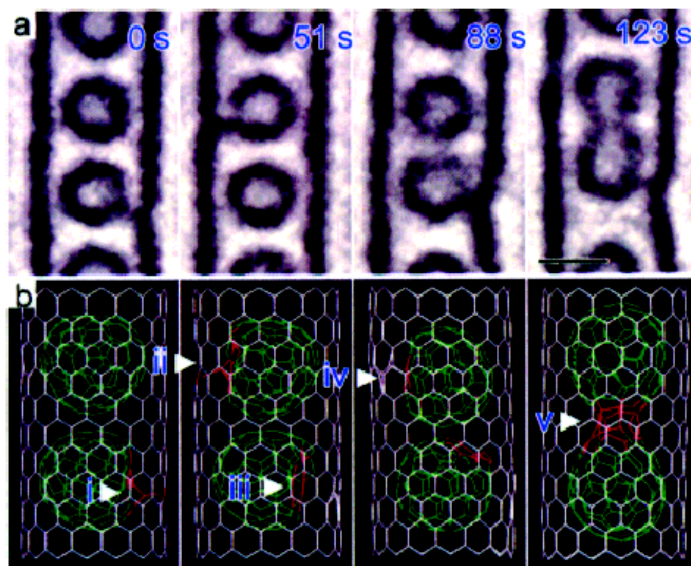


**Figure 7.19:** C<sub>92</sub> encapsulated in SWNTs under different electron irradiation time. Courtesy of Dr. Kazutomo SUENAGA, adapted from K. Urita, Y. Sato, K. Suenaga, A. Gloter, A. Hasimoto, M. Ishida, T. Shimada, T. Shinohara, S. Iijima, *Nano Lett.*, 2004, 4, 2451. Copyright American Chemical Society (2004).

Although, the discovery of C<sub>60</sub> was first confirmed by mass spectra rather than TEM. When it came to the discovery of CNTs, mass spectra was no longer useful because CNTs shows no individual peak in mass spectra since any sample contains a range of CNTs with different lengths and diameters. On the other hand, HRTEM can provide a clear image evidence of their existence. An example is shown in Figure 7.20.

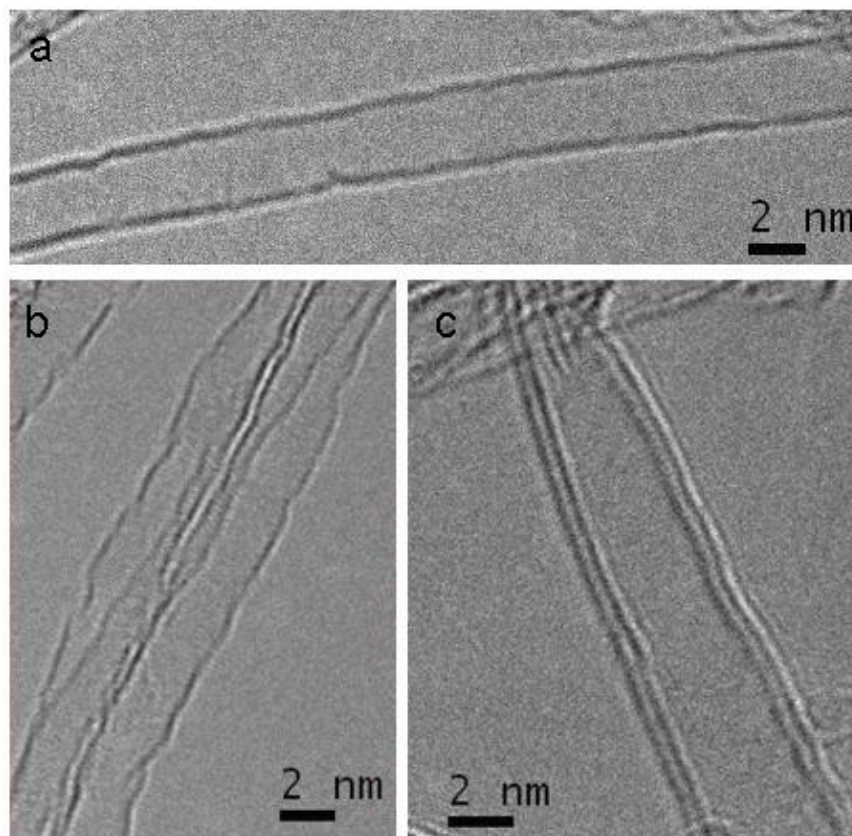


**Figure 7.20:** TEM images of SWNT and DWCNTs. Parallel dark lines corresponds to (002) lattice image of graphite. (a) and (b) SWNTs have 1 layer graphene sheet, diameter 3.2 nm. (c) DWCNT, diameter 4.0 nm.

Graphene is a planar fullerene sheet. Until recently, Raman, AFM and optical microscopy (graphene on 300 nm  $\text{SiO}_2$  wafer) were the most convenient methods to characterize samples. However, in order to confirm graphene's atomic structure and determine the difference between mono-layer and bi-layer, TEM is still a good option. In Figure 7.21, a monolayer suspended graphene is observed with its atomic structure clearly shown. Inset is the FFT of the TEM image, which can be used as a filter to get an optimized structure image. High angle annular dark field (HAADF) image usually gives better contrast for different particles on it. It is also sensitive with changes of thickness, which allows a determination of the number of graphene layers.

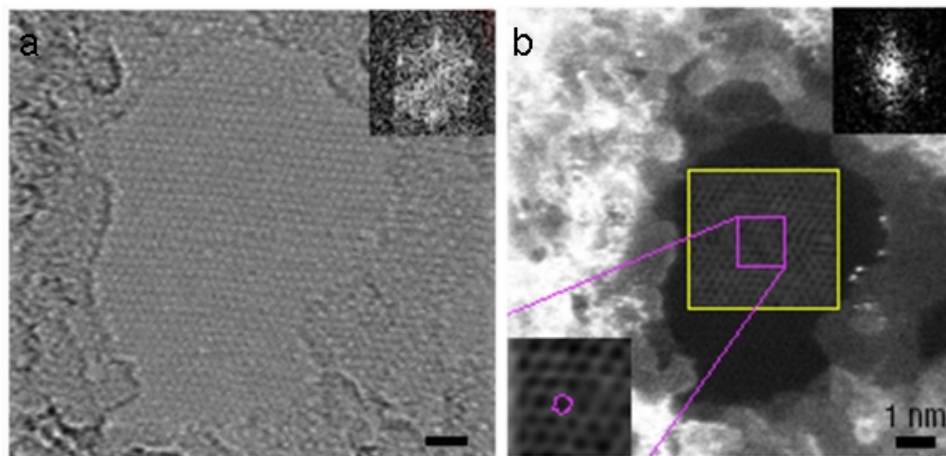


**Figure 7.21:** HRTEM of monolayer graphene. (a) Bright filed. (b) High Angle Annular Dark Field. Courtesy of Dr M. H. Gass, adapted from M. H. Gass, U. Bangert, A. L. Bleloch, P. Wang, R. R. Nair, and A. K. Geim, *Nature Nanotechnol.*, 2008, **3**, 676.

#### 7.2.3.4 Graphene stacking and edges direction

Like the situation in CNT, TEM image is a projected image. Therefore, even with exact count of edge lines, it is not possible to conclude that a sample is a single layer graphene or multi-layer. If folding graphene has AA stacking (one layer is superposed on the other), with a projected direction of [001], one image could not tell the thickness of graphene. In order to distinguish such a bilayer of graphene from a single layer of graphene, a series of tilting experiment must be done. Different stacking structures of graphene are shown in Figure 7.22a.

Theoretically, graphene has the potential for interesting edge effects. Based upon its  $sp^2$  structure, its edge can be either that of a zigzag or armchair configuration. Each of these possess different electronic properties similar to that observed for CNTs. For both research and potential application, it is important to control the growth or cutting of graphene with one specific edge. But before testing its electronic properties, all the edges have to be identified, either by directly imaging with STM or by TEM. Detailed information of graphene edges can be obtained with HRTEM, simulated with fast fourier transform (FFT). In Figure 7.22b, armchair directions are marked with red arrow respectively. A clear model in Figure 7.22c shows a 30 degree angle between zigzag edge and armchair edge.

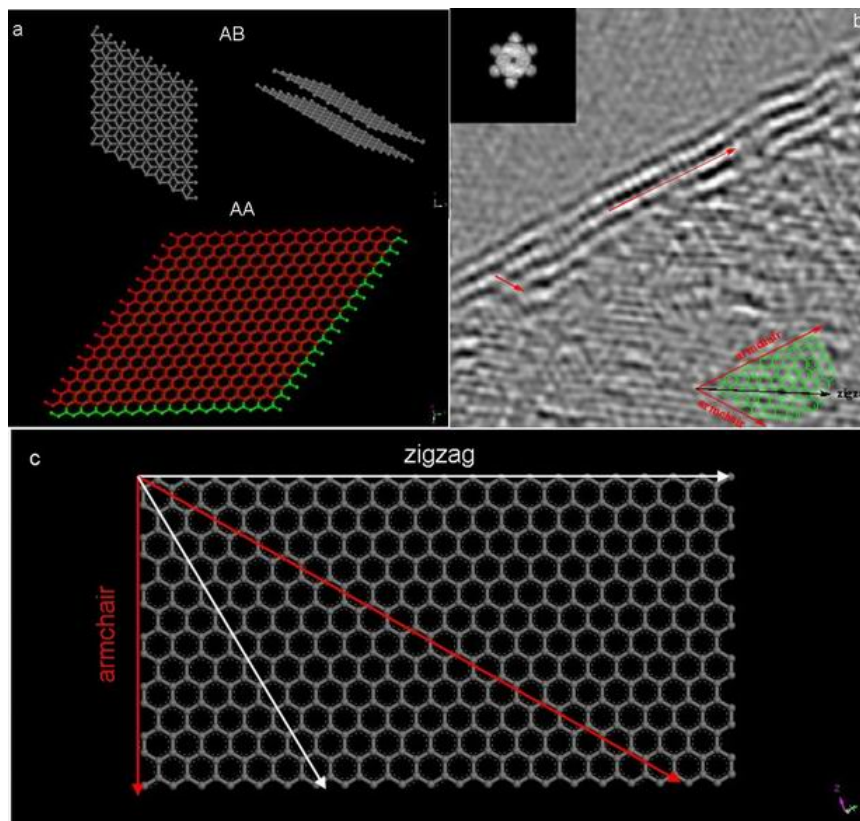


**Figure 7.22:** (a) Graphene stacking structure; (b) HRTEM image of graphene edges: zigzag and armchair (inset is FFT); (c) graphene edge model, a  $30^\circ$  angle between zigzag and armchair direction.

### 7.2.3.5 Bibliography

- K. Urita, Y. Sato, K. Suenaga, A. Gloter, A. Hasimoto, M. Ishida, T. Shimada, T. Shinohara, and S. Iijima, *Nano Lett.*, 2004, **4**, 2451.
- H. W. Kroto, J. R. Heath, S. C. O'Brien, R. F. Curl, and R. E. Smalley, *Nature*, 1985, **318**, 162.
- S. Iijima, *Nature*, 1991, **354**, 56.
- M. H. Gass, U. Bangert, A. L. Bleloch, P. Wang, R. R. Nair, and A. K. Geim, *Nature Nanotechnol.*, 2008, **3**, 676.
- L. Zheng and S. Iijima, *Phys. Rev. Lett.*, 2009, **102**, 015501.
- J. Campos-Delgado, J. M. Romo-Herrera, X. Jia, D. A. Cullen, H. Muramatsu, Y. A. Kim, T. Hayashi, Z. Ren, D. J. Smith, Y. Okuno, T. Ohba, H. Kanoh, K. Kaneko, M. Endo, H. Terrones, M. S. Dresselhaus, and M. Terrones, *Nano Lett.*, 2008, **8**, 2773.

## 7.3 Scanning Tunneling Microscopy

### 7.3.1 Scanning Tunneling Microscopy of Nanomaterials<sup>5</sup>

#### 7.3.1.1 Introduction

Scanning tunneling microscopy (STM) is a powerful instrument that allows one to image the sample surface at the atomic level. As the first generation of scanning probe microscopy (SPM), STM paves the way for the study of nano-science and nano-materials. For the first time, researchers could obtain atom-resolution images of electrically conductive surfaces as well as their local electric structures. Because of this milestone invention, Gerd Binnig (Figure 7.23) and Heinrich Rohrer (Figure 7.24) won the Nobel Prize in Physics in 1986.



**Figure 7.23:** German physicist Gerd Binnig (1947 - ).

---

<sup>5</sup>This content is available online at <<http://cnx.org/content/m38335/1.2/>>.

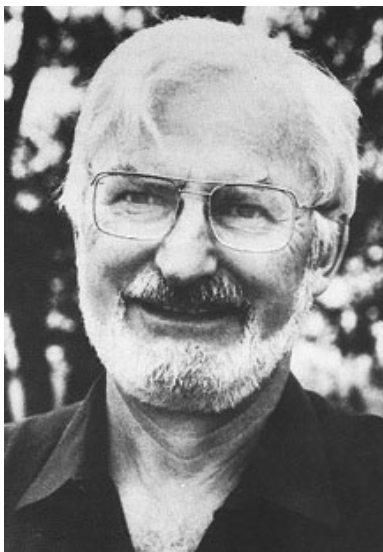


**Figure 7.24:** Swiss physicist Heinrich Rohrer (1933 - )

---

### 7.3.1.2 Principles of scanning tunneling microscopy

The key physical principle behind STM is the *tunneling effect*. In terms of their wave nature, the electrons in the surface atoms actually are not as tightly bonded to the nucleons as the electrons in the atoms of the bulk. More specifically, the electron density is not zero in the space outside the surface, though it will decrease exponentially as the distance between the electron and the surface increases (Figure 7.25a). So, when a metal tip approaches to a conductive surface within a very short distance, normally just a few Å, their perspective electron clouds will starting to overlap, and generate tunneling current if a small voltage is applied between them, as shown in Figure 7.25b.

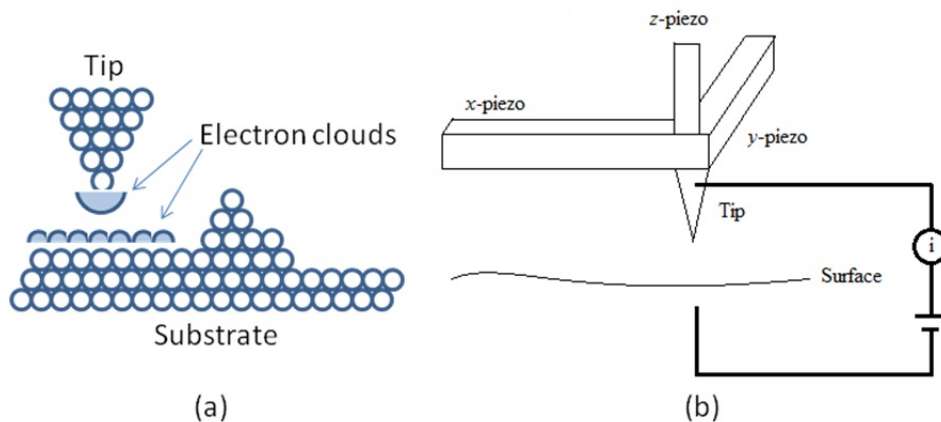


**Figure 7.25:** Schematic diagram of the principles of AFM showing (a) the interactions between tip and surface and (b) the tunneling current generated from tip and surface is measured and used as feedback to control the movement of the tip.

When we consider the separation between the tip and the surface as an ideal one-dimensional tunneling barrier, the tunneling probability, or the tunneling current  $I$ , will depend largely on  $s$ , the distance between the tip and surface, (7.10), where  $m$  is the electron mass,  $e$  the electron charge,  $h$  the Plank constant,  $[U+03D5]$  the averaged work function of the tip and the sample, and  $V$  the bias voltage.

$$I \propto \exp(-2s [2m/h^2 (\langle\phi\rangle - e|V|/2)]^{1/2}) \quad (7.10)$$

A simple calculation will show us how strongly the tunneling current is affected by the distance ( $s$ ). If  $s$  is increased by  $\Delta s = 1 \text{ \AA}$ , (7.11) and (7.12).

$$\Delta I = \exp(-2k_0 \Delta s) \quad (7.11)$$

$$k_0 = [2m/h^2 (\langle\phi\rangle - e|V|/2)]^{1/2} \quad (7.12)$$

Usually ( $\langle\phi\rangle - e|V|/2$ ) is about 5 eV, which  $k_0$  about  $1 \text{ \AA}^{-1}$ , then  $\Delta I/I = 1/s$ . That means, if  $s$  changes by 1  $\text{\AA}$ , the current will change by one order of the magnitude. That's the reason why we can get atom-level image by measuring the tunneling current between the tip and the sample.

In a typical STM operation process, the tip is scanning across the surface of sample in  $x$ - $y$  plain, the instrument records the  $x$ - $y$  position of the tip, measures the tunneling current, and control the height of the tip via a feedback circuit. The movements of the tip in  $x$ ,  $y$  and  $z$  directions are all controlled by piezo ceramics, which can be elongated or shortened according to the voltage applied on them.

Normally, there are two modes of operation for STM, *constant height mode* and *constant current mode*. In constant height mode, the tip stays at a constant height when it scans through the sample, and the tunneling current is measured at different ( $x$ ,  $y$ ) position (Figure 7.25b). This mode can be applied when the surface of sample is very smooth. But, if the sample is rough, or has some large particles on the surface, the tip may contact with the sample and damage the surface. In this case, the constant current mode is applied. During this scanning process, the tunneling current, namely the distance between the tip and the sample, is settled to an unchanged target value. If the tunneling current is higher than that target value, that means

the height of the sample surface is increasing, the distance between the tip and sample is decreasing. In this situation, the feedback control system will respond quickly and retract the tip. Conversely, if the tunneling current drops below the target value, the feedback control will have the tip closer to the surface. According to the output signal from feedback control, the surface of the sample can be imaged.

### 7.3.1.3 Comparison of atomic force microscopy (AFM) and scanning tunneling microscopy (STM)

Both AFM and STM are widely used in nano-science. According to the different working principles though, they have their own advantages and disadvantages when measuring specific properties of sample (Table 7.1). STM requires an electric circuit including the tip and sample to let the tunneling current go through. That means, the sample for STM must be conducting. In case of AFM however, it just measures the deflection of the cantilever caused by the van der Waals forces between the tip and sample. Thus, in general any kind of sample can be used for AFM. But, because of the exponential relation of the tunneling current and distance, STM has a better resolution than AFM. In STM image one can actually “see” an individual atom, while in AFM it’s almost impossible, and the quality of AFM image is largely depended on the shape and contact force of the tip. In some cases, the measured signal would be rather complicated to interpret into morphology or other properties of sample. On the other side, STM can give straight forward electric property of the sample surface.

	<b>AFM</b>	<b>STM</b>
Sample requirement	-	Conducting
Work environment	Air, liquid	Vacuum
Lateral resolution	~1 nm	~0.1 nm
Vertical resolution	~0.05 nm	~0.05 nm
Working mode	Tapping, contact	Constant current, constant height

**Table 7.1:** Comparison of AFM and STM.

### 7.3.1.4 Applications of scanning tunneling microscopy in nanoscience.

STM provides a powerful method to detect the surface of conducting and semi-conducting materials. Recently STM can also be applied in the imaging of insulators, superlattice assemblies and even the manipulation of molecules on surface. More importantly, STM can provide the surface structure and electric property of surface at atomic resolution, a true breakthrough in the development of nano-science. In this sense, the data collected from STM could reflect the local properties even of single molecule and atom. With these valuable measurement data, one could give a deeper understanding of structure-property relations in nanomaterials.

An excellent example is the STM imaging of graphene on Ru(0001), as shown in Figure 7.26. Clearly seen is the superstructure with a periodicity of  $\sim 30 \text{ \AA}$ , coming from the lattice mismatch of 12 unit cells of the graphene and 11 unit cells of the underneath Ru(0001) substrate. This so-called moiré structure can also be seen in other systems when the adsorbed layers have strong chemical bonds within the layer and weak interaction with the underlying surface. In this case, the periodic superstructure seen in graphene tells us that the formed graphene is well crystallized and expected to have high quality.

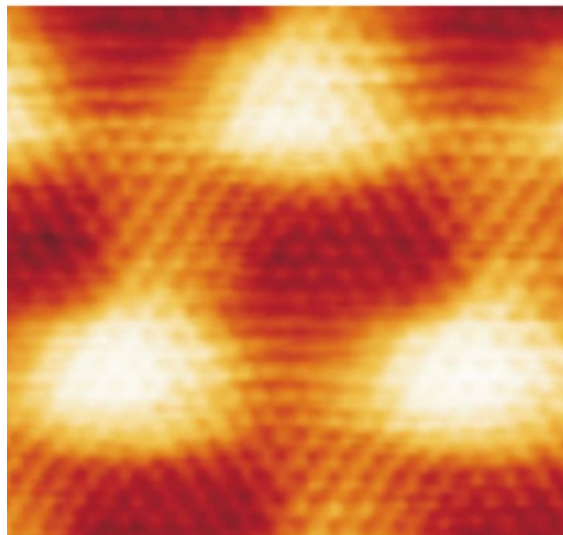


**Figure 7.26:** Atomically resolved image of the graphene overlayer. The scanning area is  $40 \times 40 \text{ \AA}$ , the operation mode is constant current mode,  $I_t$  is  $1 \text{ nA}$ ,  $V_{\text{Bias}}$  is  $-0.05 \text{ V}$ . Adapted with permission from S. Marchini, S. Gunther, and J. Winterlin, *Phys. Rev. B*, 2007, **76**, 075429. Copyrighted by the American Physical Society.

Another good example is shown to see that the measurement from STM could tell us the bonding information in single-molecular level. In thiol- and thiophene-functionalization of single-wall carbon nanotubes (SWNTs) (Figure 7.27), the use of Au nanoparticles as chemical markers for AFM gives misleading results, while STM imaging could give correct information of substituent location. From AFM image, Au-thiol-SWNT (Figure 7.28a) shows that most of the sidewalls are unfunctionalized, while Au-thiophene-SWNT (Figure 7.28c) shows long bands of continuous functionalized regions on SWNT. This could lead to the estimation that thiophene is better functionalized to SWNT than thiol. Yet, if we look up to the STM image (Figure 7.28b and d), in thiol-SWNTs the multiple functional groups are tightly bonded in about 5 - 25 nm, while in thiophene-SWNTs the functionalization is spread out uniformly along the whole length of SWNT. This information indicates that actually the functionalization levels of thiol- and thiophene-SWNTs are comparable. The difference is that, in thiol-SWNTs, functional groups are grouped together and each group is bonded to a single gold nanoparticle, while in thiophene-SWNTs, every individual functional group is bonded to a nanoparticle.

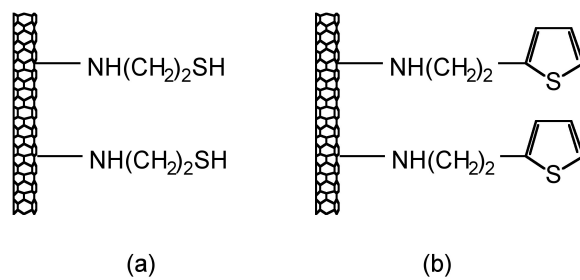


**Figure 7.27:** Structure of (a) thiol-functionalized SWNTs and thiophene-functionalized SWNTs.

---

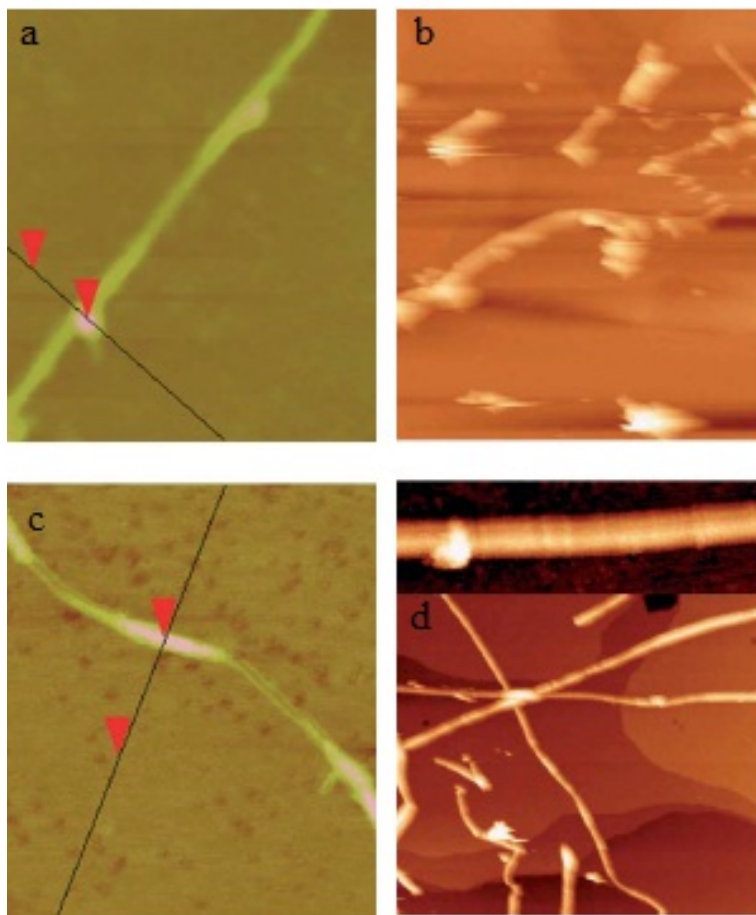


**Figure 7.28:** Difference between AFM and STM images of functionalized SWNTs. (a) and (c) are tapping mode AFM images and height profiles of thiol- and thiophene-SWNTs. (b) and (d) are STM images of thiol-SWNTs (scanning area is  $4560 \times 4000 \text{ \AA}$ , the operation mode is constant current mode,  $I_t$  is  $3.25 \text{ pA}$ ,  $V_{\text{Bias}}$  is  $-0.5 \text{ V}$ ) and thiophene-SWNTs (scanning area is  $4560 \times 4000 \text{ \AA}$ , the operation mode is constant current mode,  $I_t$  is  $5.66 \text{ pA}$ ,  $V_{\text{Bias}}$  is  $-0.8 \text{ V}$ ). Inset in (d) is a higher resolution image of the local defects on thiophene-SWNT ( $500 \times 140 \text{ \AA}$ , the operation mode is constant current mode,  $I_t$  is  $25.5 \text{ pA}$ ,  $V_{\text{Bias}}$  is  $-0.8 \text{ V}$ ). Adapted from L. Zhang, J. Zhang, N. Schmandt, J. Cratty, V. N. Khabashesku, K. F. Kelly, and A. R. Barron, *Chem. Commun.*, 2005, 5429 (<http://dx.doi.org/10.1039/b509257d><sup>6</sup>). Reproduced by permission of The Royal Society of Chemistry.

### 7.3.1.5 Bibliography

- G. Binnig and H. Rohrer, *Surf. Sci.*, 1983, **126**, 236.
- G. Binnig and H. Rohrer, *Surf. Sci.*, 1985, **152/153**, 17.
- J. Griffith, *Annu. Rev. Mater. Sci.*, 1990, **20**, 219.

<sup>6</sup><http://dx.doi.org/10.1039/b509257d>

- M. Poggi, L. Bottomley, and P. Lillehei, *Anal. Chem.*, 2002, **74**, 2851.
- P. Samori. *J. Mater. Chem.*, 2005, **14**, 1353.
- S. Marchini, S. Gunther, and J. Winterlin, *Phys. Rev. B*, 2007, **76**, 075429.
- L. Zhang, J. Zhang, N. Schmandt, J. Cratty, V. N. Khabashesku, K. F. Kelly, and A. R. Barron, *Chem. Commun.*, 2005, 5429.

## 7.3.2 Adaptations to Scanning Tunneling Microscopy<sup>7</sup>

### 7.3.2.1 Introduction

Scanning tunneling microscopy (STM) is a relatively recent imaging technology that has proven very useful for determining the topography of conducting and semiconducting samples with angstrom ( $\text{\AA}$ ) level precision. STM was invented by Gerd Binnig (Figure 7.29) and Heinrich Rohrer (Figure 7.30), who both won the 1986 Nobel Prize in physics for their technological advances.



**Figure 7.29:** German physicist Gerd Binnig (1947 - ).

---

<sup>7</sup>This content is available online at <<http://cnx.org/content/m43549/1.1/>>.

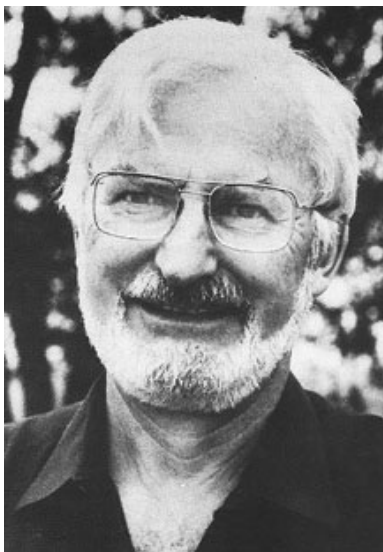


**Figure 7.30:** Swiss physicist Heinrich Rohrer (1933 - ).

---

The main component of a scanning tunneling microscope is a rigid metallic probe tip, typically composed of tungsten, connected to a piezodrive containing three perpendicular piezoelectric transducers (Figure 7.31). The tip is brought within a fraction of a nanometer of an electrically conducting sample. At close distances, the electron clouds of the metal tip overlap with the electron clouds of the surface atoms (Figure 7.31 inset). If a small voltage is applied between the tip and the sample a tunneling current is generated. The magnitude of this tunneling current is dependent on the bias voltage applied and the distance between the tip and the surface. A current amplifier can convert the generated tunneling current into a voltage. The magnitude of the resulting voltage as compared to the initial voltage can then be used to control the piezodrive, which controls the distance between the tip and the surface (i.e., the  $z$  direction). By scanning the tip in the  $x$  and  $y$  directions, the tunneling current can be measured across the entire sample. The STM system can operate in either of two modes: .

1. Constant height.
2. Constant current.

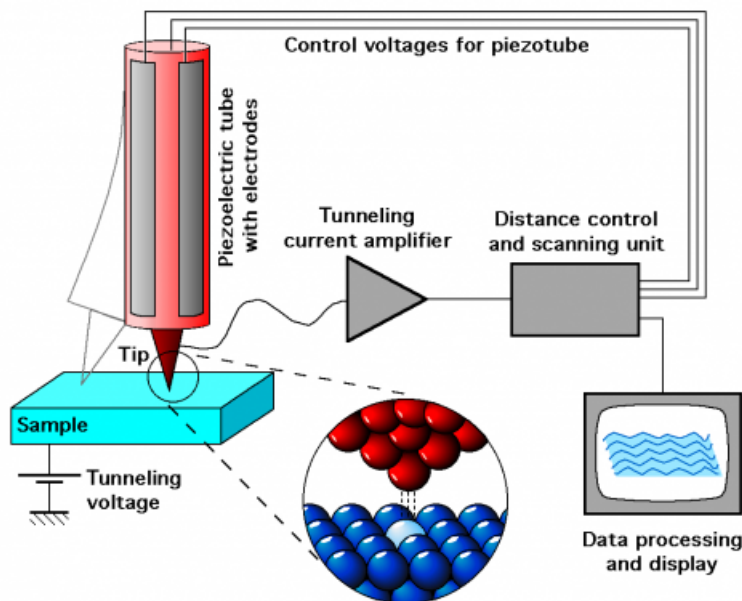


**Figure 7.31:** Schematic drawing of a STM apparatus.

In constant height mode, the tip is fixed in the  $z$  direction and the change in tunneling current as the tip changes in the  $x,y$  direction is collected and plotted to describe the change in topography of the sample. This method is dangerous for use in samples with fluctuations in height as the fixed tip might contact and destroy raised areas of the sample. A common method for non-uniformly smooth samples is constant current mode. In this mode, a target current value, called the set point, is selected and the tunneling current data gathered from the sample is compared to the target value. If the collected voltage deviates from the set point, the tip is moved in the  $z$  direction and the voltage is measured again until the target voltage is reached. The change in the  $z$  direction required to reach the set point is recorded across the entire sample and plotted as a representation of the topography of the sample. The height data is typically displayed as a gray scale image of the topography of the sample, where lighter areas typically indicate raised sample areas and darker spots indicate protrusions. These images are typically colored for better contrast.

The standard method of STM, described above, is useful for many substances (including high precision optical components, disk drive surfaces, and buckyballs) and is typically used under ultrahigh vacuum to avoid contamination of the samples from the surrounding systems. Other sample types, such as semiconductor interfaces or biological samples, need some enhancements to the traditional STM apparatus to yield more detailed sample information. Three such modifications, spin-polarized STM (SP-STM), ballistic electron emission microscopy (BEEM) and photon STM (PSTM) are summarized in Table 7.2 and in described in detail below.

Name	Alterations to conventional STM	Sample types	Limitations
STM	None	Conducting surface	Rigidity of probe
SP-STM	Magnetized STM tip	Magnetic	Needs to be overlaid with STM, magnetized tip type
BEEM	Three-terminal with base electrode and current collector	Interfaces	Voltage, changes due to barrier height
PSTM	Optical fiber tip	Biological	Optical tip and prism manufacture

**Table 7.2:** Comparison of conventional STM and alterations.

### 7.3.2.2 Spin-polarized STM

Spin-polarized scanning tunneling microscopy (SP-STM) can be used to provide detailed information of magnetic phenomena on the single-atom scale. This imaging technique is particularly important for accurate measurement of superconductivity and high-density magnetic data storage devices. In addition, SP-STM, while sensitive to the partial magnetic moments of the sample, is not a field-sensitive technique and so can be applied in a variety of different magnetic fields.

#### 7.3.2.2.1 Device setup and sample preparation

In SP-STM, the STM tip is coated with a thin layer of magnetic material. As with STM, voltage is then applied between tip and sample resulting in tunneling current. Atoms with partial magnetic moments that are aligned in the same direction as the partial magnetic moment of the atom at the very tip of the STM tip show a higher magnitude of tunneling current due to the interactions between the magnetic moments. Likewise, atoms with partial magnetic moments opposite that of the atom at the tip of the STM tip demonstrate a reduced tunneling current (Figure 7.32). A computer program can then translate the change in tunneling current to a topographical map, showing the spin density on the surface of the sample.

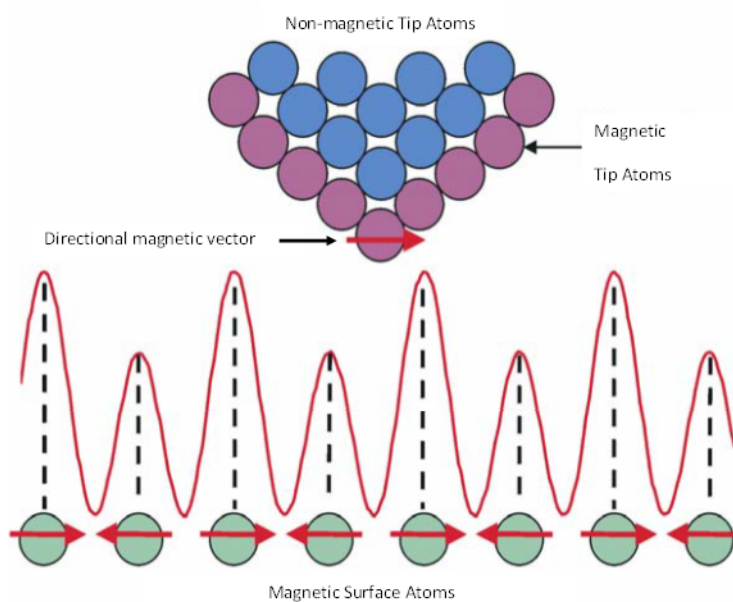


**Figure 7.32:** Schematic illustration of magnetized tip for SP-STM.

The sensitivity to magnetic moments depends greatly upon the direction of the magnetic moment of the tip, which can be controlled by the magnetic properties of the material used to coat the outermost layer of the tungsten STM probe. A wide variety of magnetic materials have been studied as possible coatings, including both ferromagnetic materials, such as a thin coat of iron or of gadolinium, and antiferromagnetic materials such as chromium. Another method that has been used to make a magnetically sensitive probe tip is irradiation of a semiconducting GaAs tip with high energy circularly polarized light. This irradiation causes a splitting of electrons in the GaAs valence band and population of the conduction band with spin-polarized electrons. These spin-polarized electrons then provide partial magnetic moments which in turn influence the tunneling current generated by the sample surface.

Sample preparation for SP-STM is essentially the same as for STM. SP-STM has been used to image samples such as thin films and nanoparticle constructs as well as determining the magnetic topography of thin metallic sheets such as in Figure 7.33. The upper image is a traditional STM image of a thin layer of cobalt, which shows the topography of the sample. The second image is an SP-STM image of the same layer of cobalt, which shows the magnetic domain of the sample. The two images, when combined provide useful information about the exact location of the partial magnetic moments within the sample.

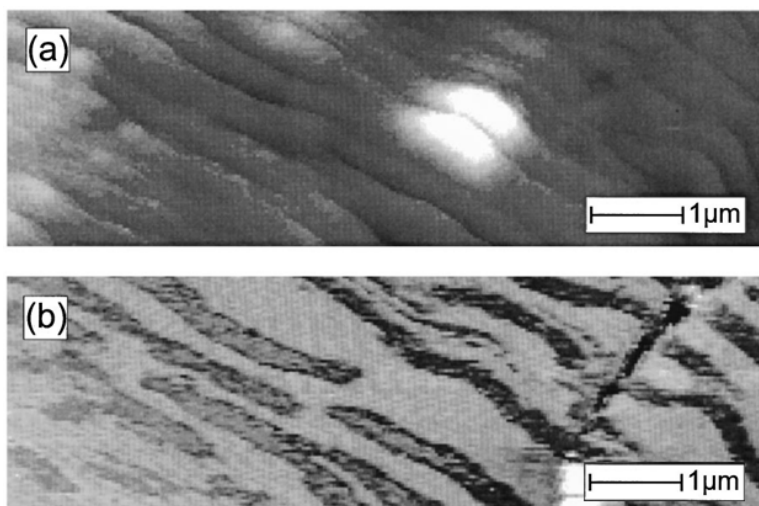


**Figure 7.33:** A thin layer of Co(0001) as imaged by (a) STM, showing the topography, and (b) SP-STM, showing the magnetic domain structure. Image adapted from W. Wulfhekel and J. Kirschner, *Appl. Phys. Lett.*, 1999, **75**, 1944.

### 7.3.2.2.2 Limitations

One of the major limitations with SP-STM is that both distance and partial magnetic moment yield the same contrast in a SP-STM image. This can be corrected by combination with conventional STM to get multi-domain structures and/or topological information which can then be overlaid on top of the SP-STM image, correcting for differences in sample height as opposed to magnetization.

The properties of the magnetic tip dictate much of the properties of the technique itself. If the outermost atom of the tip is not properly magnetized, the technique will yield no more information than a traditional STM. The direction of the magnetization vector of the tip is also of great importance. If the magnetization vector of the tip is perpendicular to the magnetization vector of the sample, there will be no spin contrast. It is therefore important to carefully choose the coating applied to the tungsten STM tip in order to align appropriately with the expected magnetic moments of the sample. Also, the coating makes the magnetic tips more expensive to produce than standard STM tips. In addition, these tips are often made of mechanically soft materials, causing them to wear quickly and require a high cost of maintenance.

### 7.3.2.3 Ballistic electron emission microscopy

Ballistic electron emission microscopy (BEEM) is a technique commonly used to image semiconductor interfaces. Conventional surface probe techniques can provide detailed information on the formation of interfaces, but lack the ability to study fully formed interfaces due to inaccessibility to the surface. BEEM allows for the ability to obtain a quantitative measure of electron transport across fully formed interfaces, something necessary for many industrial applications.

#### 7.3.2.3.1 Device setup and sample preparation

BEEM utilizes STM with a three-electrode configuration, as seen in Figure 7.31. In this technique, ballistic electrons are first injected from a STM tip into the sample, traditionally composed of at least two layers

separated by an interface, which rests on three indium contact pads that provide a connection to a base electrode (Figure 7.34). As the voltage is applied to the sample, electrons tunnel across the vacuum and through the first layer of the sample, reaching the interface, and then scatter. Depending on the magnitude of the voltage, some percentage of the electrons tunnel through the interface, and can be collected and measured as a current at a collector attached to the other side of the sample. The voltage from the STM tip is then varied, allowing for measurement of the barrier height. The barrier height is defined as the threshold at which electrons will cross the interface and are measurable as a current in the far collector. At a metal/n-type semiconductor interface this is the difference between the conduction band minimum and the Fermi level. At a metal/p-type semiconductor interface this is the difference between the valence band maximum of the semiconductor and the metal Fermi level. If the voltage is less than the barrier height, no electrons will cross the interface and the collector will read zero. If the voltage is greater than the barrier height, useful information can be gathered about the magnitude of the current at the collector as opposed to the initial voltage.

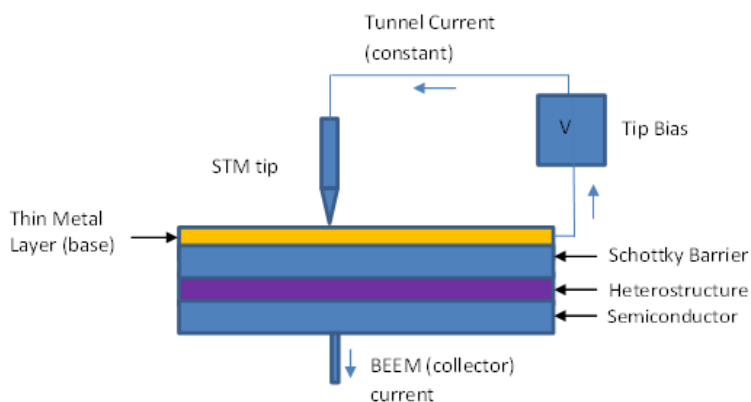


**Figure 7.34:** Diagram of a STM/BEEM system. The tip is maintained at the tunneling voltage,  $V$ , and the tunneling current,  $I_t = V_t/R_F$ , is held constant by the STM feedback circuit. The sample base layer is grounded and current into the semiconductor is measured by a virtual ground current amplifier.

Samples are prepared from semiconductor wafers by chemical oxide growth-strip cycles, ending with the growth of a protective oxide layer. Immediately prior to imaging the sample is spin-etched in an inert environment to remove oxides of oxides and then transferred directly to the ultra-high vacuum without air exposure. The BEEM apparatus itself is operated in a glove box under inert atmosphere and shielded from light.

Nearly any type of semiconductor interface can be imaged with BEEM. This includes both simple binary interfaces such as Au/n-Si(100) and more chemically complex interfaces such as Au/n-GaAs(100), such as seen in Figure 7.35.

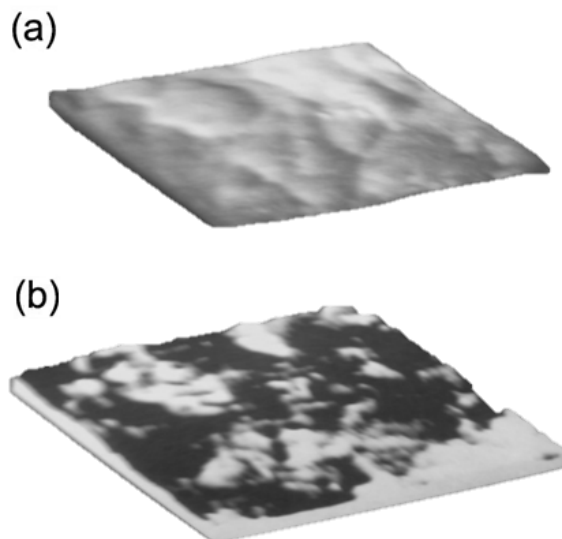


**Figure 7.35:** Images of Au/n-GaAs(100) layer (image area  $510 \text{ \AA} \times 390 \text{ \AA}$ ) showing (a) the topography of the Au surface and (b) the BEEM grey-scale interface image. Image adapted from M. H. Hecht, L. D. Bell, W. J. Kaiser, and F. J. Grunthaler, *Appl. Phys. Lett.*, 1989, **55**, 780.

### 7.3.2.3.2 Limitations

Expected barrier height matters a great deal in the desired setup of the BEEM apparatus. If it is necessary to measure small collector currents, such as with an interface of high-barrier-height, a high-gain, low-noise current preamplifier can be added to the system. If the interface is of low-barrier-height, the BEEM apparatus can be operated at very low temperatures, accomplished by immersion of the STM tip in liquid nitrogen and enclosure of the BEEM apparatus in a nitrogen-purged glove box.

### 7.3.2.4 Photon STM

Photon scanning tunneling microscopy (PSTM) measures light to determine more information about characteristic sample topography. It has primarily been used as a technique to measure the electromagnetic interaction of two metallic objects in close proximity to one another and biological samples, which are both difficult to measure using many other common surface analysis techniques.

#### 7.3.2.4.1 Device setup and sample preparation

This technique works by measuring the tunneling of photons to an optical tip. The source of these photons is the evanescent field generated by the total internal reflection (TIR) of a light beam from the surface of the sample (Figure 7.36). This field is characteristic of the sample material on the TIR surface, and can be measured by a sharpened optical fiber probe tip where the light intensity is converted to an electrical signal (Figure 7.37). Much like conventional STM, the force of this electrical signal modifies the location of the tip in relation to the sample. By mapping these modifications across the entire sample, the topography can be

determined to a very accurate degree as well as allowing for calculations of polarization, emission direction and emission time.

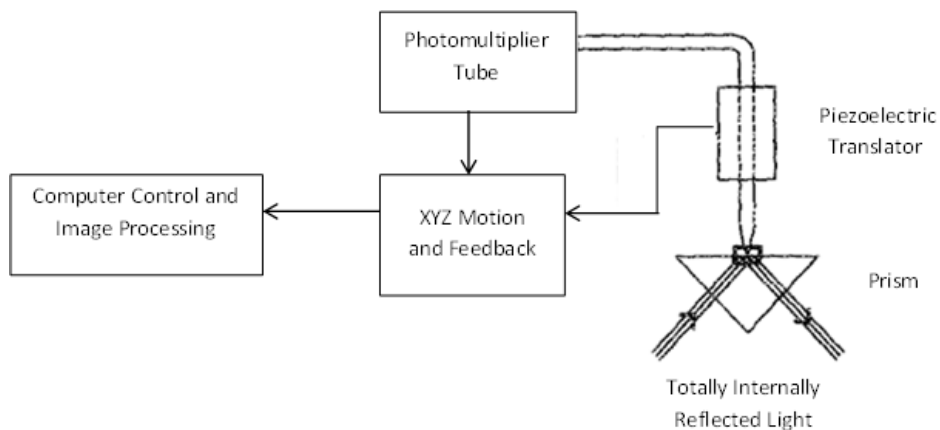


**Figure 7.36:** A schematic of a PSTM system.

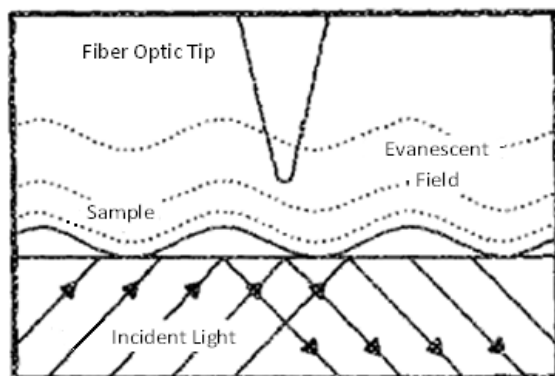


**Figure 7.37:** A TIR light beam generates an evanescent field which is modulated by the sample. A sharpened fiber optic probe tip receives light from the evanescent field and spatial variations in evanescent field intensity form the basis for imaging.

In PSTM, the vertical resolution is governed only by the noise, as opposed to conventional STM where the vertical resolution is limited by the tip dimensions. Therefore, this technique provides advantages over more conventional STM apparatus for samples where subwavelength resolution in the vertical dimension is a critical measurement, including fractal metal colloid clusters, nanostructured materials and simple organic

molecules.

Samples are prepared by placement on a quartz or glass slide coupled to the TIR face of a triangular prism containing a laser beam, making the sample surface into the TIR surface (Figure 7.37). The optical fiber probe tips are constructed from UV grade quartz optical fibers by etching in HF acid to have nominal end diameters of 200 nm or less and resemble either a truncated cone or a paraboloid of revolution (Figure 7.38).

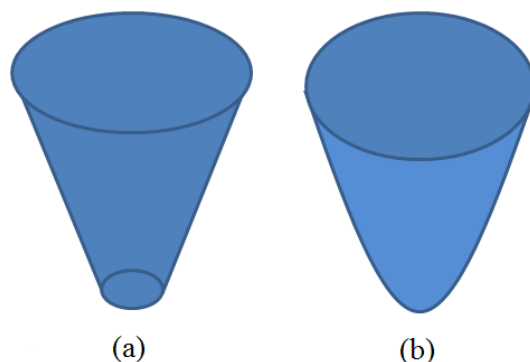


**Figure 7.38:** Possible optical fiber tip configurations: (a) truncated cone and (b) paraboloid of rotation.

---

PSTM shows much promise in the imaging of biological materials due to the increase in vertical resolution and the ability to measure a sample within a liquid environment with a high index TIR substrate and probe tip. This would provide much more detailed information about small organisms than is currently available.

#### 7.3.2.4.2 Limitations

The majority of the limitations in this technique come from the materials and construction of the optical fibers and the prism used in the sample collection. The sample needs to be kept at low temperatures, typically around 100K, for the duration of the imaging and therefore cannot decompose or be otherwise negatively impacted by drastic temperature changes.

#### 7.3.2.5 Conclusion

Scanning tunneling microscopy can provide a great deal of information into the topography of a sample when used without adaptations, but with adaptations, the information gained is nearly limitless. Depending on the likely properties of your sample surface, SP-STM, BEEM and PSTM can provide much more accurate topographical pictures than conventional forms of STM (Table 7.2). All of these adaptations to STM have their limitations and all work within relatively specialized categories and subsets of substances, but they are very strong tools that are constantly improving to provide more useful information about materials to the nanometer scale.

#### 7.3.2.6 Bibliography

- R. Berndt and J. K. Gimzewski, *Phys. Rev. B*, 1993, **48**, 4746.
- G. Binnig, H. Rohrer, C. Gerber, and E. Weibel, *Phys. Rev. Lett.*, 1982, **49**, 57.
- M. Bode, *Rep. Prog. Phys.* 2003, **66**, 523.
- M. H. Hecht, L. D. Bell, W. J. Kaiser, and F. J. Grunthaner, *Appl. Phys. Lett.*, 1989, **55**, 780.

- W. J. Kaiser and L. D. Bell, *Phys. Rev. Lett.*, 1988, **60**, 1406.
- R. C. Reddick, D. W. Warmack, D. W. Chilcott, S. L. Sharp, and T. L. Ferrell, *Rev. Sci. Instrum.*, 1990, **61**, 3669.
- D. P. Tsai, J. Kovacs, Z. Wang, M. Moskovits, V. M. Shalaev, J. S. Suh, and R. Botet, *Phys. Rev. Lett.*, 1994, **72**, 4149.
- W. Wulfhekel and J. Kirschner, *Appl. Phys. Lett.*, 1999, **75**, 1944.

## 7.4 Spectroscopic Characterization of Nanoparticles

### 7.4.1 Using UV-vis for the detection and characterization of silicon quantum dots<sup>8</sup>

#### 7.4.1.1 What are quantum dots?

Quantum dots (QDs) are small semiconductor nanoparticles generally composed of two elements that have extremely high quantum efficiencies when light is shined on them. The most common quantum dots are CdSe, PbS, and ZnSe, but there are many many other varieties of these particles that contain other elements as well. QDs can also be made of just three elements or just one element such as silicon.

#### 7.4.1.2 Synthesis of silicon quantum dots

Silicon quantum dots are synthesized in inverse micelles.  $\text{SiCl}_4$  is reduced using a two fold excess of  $\text{LiAlH}_4$  (Figure 7.39). After the silicon has been fully reduced and the excess reducing agent quenched, the particles are capped with hydrogens and are hydrophobic. A platinum catalyzed ligand exchange of hydrogen for allylamine will produce hydrophilic particles (Figure 7.40). All reactions in making these particles are extremely air sensitive, and silica is formed readily, so the reactions should be performed in a highly controlled atmosphere, such as a glove box. The particles are then washed in DMF, and finally filtered and stored in deionized water. This will allow the Si QDs to be pure in water, and the particles are ready for analysis. This technique yields Si QDs of 1 - 2 nm in size.

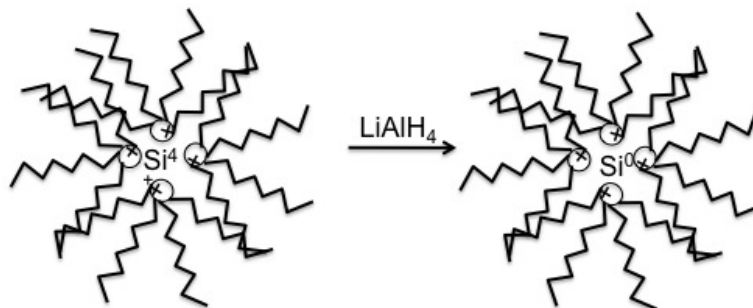


**Figure 7.39:** A schematic representation of the inverse micelle used for the synthesis of Si QDs.

<sup>8</sup>This content is available online at <<http://cnx.org/content/m34655/1.1/>>.

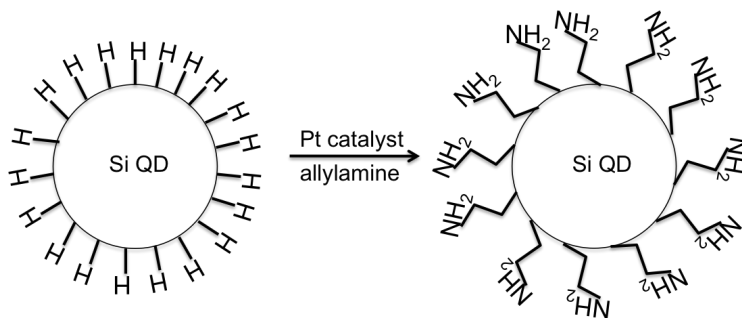


**Figure 7.40:** Conversion of hydrophobic Si QDs to hydrophilic Si QDs. Adapted from J. H. Warner, A. Hoshino, K. Yamamoto, and R. D. Tilley, *Angew. Chem., Int. Ed.*, 2005, **44**, 4550. Copyright: American Chemical Society (2005).

#### 7.4.1.2.1 Sample preparation of Si QDs

The reported absorption wavelength for 1 - 2 nm Si QDs is 300 nm. With the hydrophobic Si QDs, UV-vis absorbance analysis in toluene does not yield an acceptable spectrum because the UV-vis absorbance cutoff is 287 nm, which is very close to 300 nm for the peaks to be resolvable. A better hydrophobic solvent would be hexanes. All measurements of these particles would require a quartz cuvette since the glass absorbance cutoff (300 nm) is exactly where the particles would be observed. Hydrophilic substituted particles do not need to be transferred to another solvent because water's absorbance cutoff is much lower. There is usually a slight impurity of DMF in the water due to residue on the particles after drying. If there is a DMF peak in the spectrum with the Si QDs the wavelengths are far enough apart to be resolved.

#### 7.4.1.3 What information can be obtained from UV-visible spectra?

Quantum dots are especially interesting when it comes to UV-vis spectroscopy because the size of the quantum dot can be determined from the position of the absorption peak in the UV-vis spectrum. Quantum dots absorb different wavelengths depending on the size of the particles (e.g., Figure 7.41). Many calibration curves would need to be done to determine the exact size and concentration of the quantum dots, but it is entirely possible and very useful to be able to determine size and concentration of quantum dots in this way since other ways of determining size are much more expensive and extensive (electron microscopy is most widely used for this data).

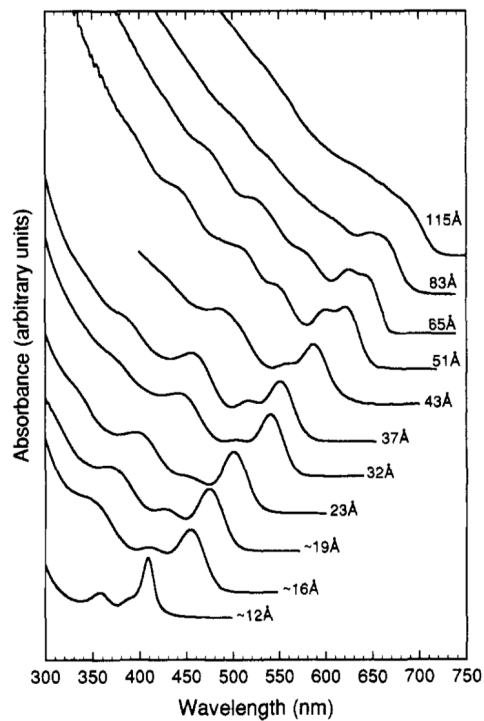


**Figure 7.41:** Absorbance of different sized CdSe QDs. Reprinted with permission from C. B. Murray, D. J. Norris, and M. G. Bawendi, *J. Am. Chem. Soc.*, 1993, **115**, 8706. Copyright: American Chemical Society (1993).

An example of silicon quantum dot data can be seen in Figure 7.42. The wider the absorbance peak is, the less monodispersed the sample is.

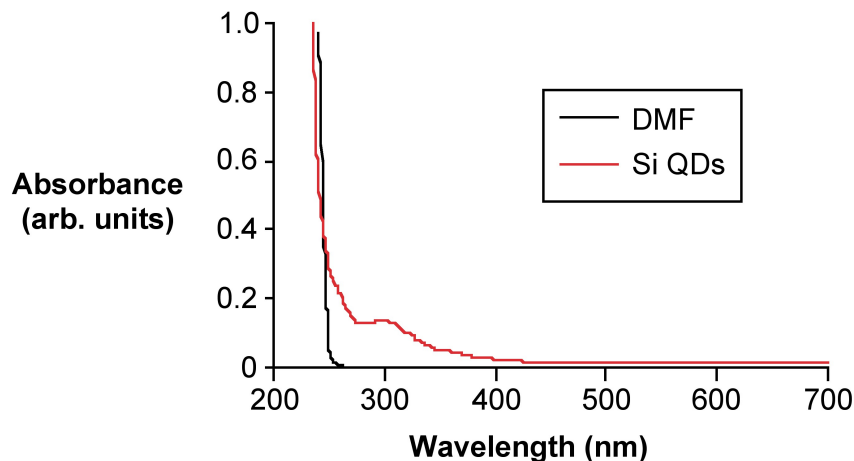


Figure 7.42: UV-vis absorbance spectrum of 1 - 2 nm Si QDs with a DMF reference spectrum.

#### 7.4.1.3.1 Why is knowing the size of QDs important?

Different size (different excitation) quantum dots can be used for different applications. The absorbance of the QDs can also reveal how monodispersed the sample is; more monodispersity in a sample is better and more useful in future applications. Silicon quantum dots in particular are currently being researched for making more efficient solar cells. The monodispersity of these quantum dots is particularly important for getting optimal absorbance of photons from the sun or other light source. Different sized quantum dots will absorb light differently, and a more exact energy absorption is important in the efficiency of solar cells. UV-vis absorbance is a quick, easy, and cheap way to determine the monodispersity of the silicon quantum dot sample. The peak width of the absorbance data can give that information. The other important information for future applications is to get an idea about the size of the quantum dots. Different size QDs absorb at different wavelengths; therefore, specific size Si QDs will be required for different cells in tandem solar cells.

#### 7.4.1.4 Bibliography

- J. H. Warner, A. Hoshino, K. Yamamoto, and R. D. Tilley, *Angew. Chem., Int. Ed.*, 2005, **44**, 4550.
- C. B. Murray, D. J. Norris, and M. G. Bawendi, *J. Am. Chem. Soc.*, 1993, **115**, 8706.

### 7.4.2 Optical Properties of Group 12-16 (II-VI) Semiconductor Nanoparticles<sup>9</sup>

#### 7.4.2.1 What are Group 12-16 semiconductors?

Semiconductor materials are generally classified on the basis of the periodic table group that their constituent elements belong to. Thus, Group 12-16 semiconductors, formerly called II-VI semiconductors, are materials whose cations are from the Group 12 and anions are from Group 16 in the periodic table (Figure 7.43). Some examples of Group 12-16 semiconductor materials are cadmium selenide (CdSe), zinc sulfide (ZnS), cadmium telluride (CdTe), zinc oxide (ZnO), and mercuric selenide (HgSe) among others.

<sup>9</sup>This content is available online at <<http://cnx.org/content/m34553/1.1/>>.

NOTE: The new IUPAC (International Union of Pure and Applied Chemistry) convention is being followed in this document, to avoid any confusion with regard to conventions used earlier. In the old IUPAC convention, Group 12 was known as Group IIB with the roman numeral 'II' referring to the number of electrons in the outer electronic shells and B referring to being on the right part of the table. However, in the CAS (Chemical Abstracts Service), the alphabet B refers to transition elements as compared to main group elements, though the roman numeral has the same meaning. Similarly, Group 16 was earlier known as Group VI because all the elements in this group have 6 valence shell electrons.

Group →	12	13	14	15	16
↓ Period					
2		5 B	6 C	7 N	8 O
3		13 Al	14 Si	15 P	16 S
4	30 Zn	31 Ga	32 Ge	33 As	34 Se
5	48 Cd	49 In	50 Sn	51 Sb	52 Te
6	80 Hg	81 Tl	82 Pb	83 Bi	84 Po
7	112 Cn	113 Uut	114 Uuq	115 Uup	116 Uuh

**Figure 7.43:** The red box indicates the Group 12 and Group 16 elements in the periodic table.

#### 7.4.2.2 What are Group 12-16 (II-VI) semiconductor nanoparticles?

From the Greek word *nanos* - meaning "dwarf" this prefix is used in the metric system to mean  $10^{-9}$  or one billionth (1/1,000,000,000). Thus a nanometer is  $10^{-9}$  or one billionth of a meter, and a nanojoule is  $10^{-9}$  or one billionth of a Joule, etc. A nanoparticle is ordinarily defined as any particle with at least one of its dimensions in the 1 - 100 nm range.

Nanoscale materials often show behavior which is intermediate between that of a bulk solid and that of an individual molecule or atom. An inorganic nanocrystal can be imagined to be comprised of a few atoms or molecules. It thus will behave differently from a single atom; however, it is still smaller than a macroscopic solid, and hence will show different properties. For example, if one would compare the chemical reactivity of a bulk solid and a nanoparticle, the latter would have a higher reactivity due to a significant fraction of the total number of atoms being on the surface of the particle. Properties such as boiling point, melting point, optical properties, chemical stability, electronic properties, etc. are all different in a nanoparticle as compared to its bulk counterpart. In the case of Group 12-16 semiconductors, this reduction in size from bulk to the nanoscale results in many size dependent properties such as varying band gap energy, optical and electronic properties.

#### 7.4.2.3 Optical properties of semiconductor quantum nanoparticles

In the case of semiconductor nanocrystals, the effect of the size on the optical properties of the particles is very interesting. Consider a Group 12-16 semiconductor, cadmium selenide (CdSe). A 2 nm sized CdSe

crystal has a blue color fluorescence whereas a larger nanocrystal of CdSe of about 6 nm has a dark red fluorescence (Figure 7.44). In order to understand the size dependent optical properties of semiconductor nanoparticles, it is important to know the physics behind what is happening at the nano level.



**Figure 7.44:** Fluorescing CdSe quantum dots synthesized in a heat transfer liquid of different sizes (M. S. Wong, Rice University).

---

#### 7.4.2.3.1 Energy levels in a semiconductor

The electronic structure of any material is given by a solution of Schrödinger equations with boundary conditions, depending on the physical situation. The electronic structure of a semiconductor (Figure 7.45) can be described by the following terms:

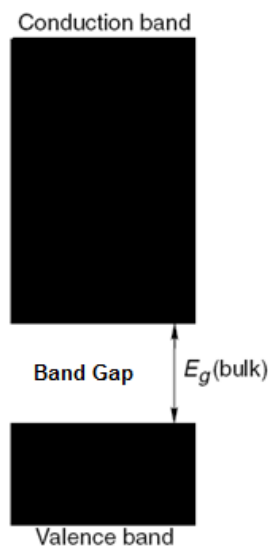


**Figure 7.45:** Simplified representation of the energy levels in a bulk semiconductor.

---

#### 7.4.2.3.1.1 Energy level

By the solution of Schrödinger's equations, the electrons in a semiconductor can have only certain allowable energies, which are associated with energy levels. No electrons can exist in between these levels, or in other words can have energies in between the allowed energies. In addition, from Pauli's Exclusion Principle, only 2 electrons with opposite spin can exist at any one energy level. Thus, the electrons start filling from the lowest energy levels. Greater the number of atoms in a crystal, the difference in allowable energies become very small, thus the distance between energy levels decreases. However, this distance can never be zero. For a bulk semiconductor, due to the large number of atoms, the distance between energy levels is very small and for all practical purpose the energy levels can be described as continuous (Figure 7.45).

#### 7.4.2.3.1.2 Band gap

From the solution of Schrödinger's equations, there are a set of energies which is not allowable, and thus no energy levels can exist in this region. This region is called the band gap and is a quantum mechanical phenomenon (Figure 7.45). In a bulk semiconductor the bandgap is fixed; whereas in a quantum dot nanoparticle the bandgap varies with the size of the nanoparticle.

#### 7.4.2.3.1.3 Valence band

In bulk semiconductors, since the energy levels can be considered as continuous, they are also termed as energy bands. Valence band contains electrons from the lowest energy level to the energy level at the lower edge of the bandgap (Figure 7.45). Since filling of energy is from the lowest energy level, this band is usually almost full.

#### 7.4.2.3.1.4 Conduction band

The conduction band consists of energy levels from the upper edge of the bandgap and higher (Figure 7.45). To reach the conduction band, the electrons in the valence band should have enough energy to cross the band gap. Once the electrons are excited, they subsequently relax back to the valence band (either radiatively or non-radiatively) followed by a subsequent emission of radiation. This property is responsible for most of the applications of quantum dots.

#### 7.4.2.3.1.5 Exciton and exciton Bohr radius

When an electron is excited from the valence band to the conduction band, corresponding to the electron in the conduction band a hole (absence of electron) is formed in the valence band. This electron pair is called an exciton. Excitons have a natural separation distance between the electron and hole, which is characteristic of the material. This average distance is called exciton Bohr radius. In a bulk semiconductor, the size of the crystal is much larger than the exciton Bohr radius and hence the exciton is free to move throughout the crystal.

#### 7.4.2.3.2 Energy levels in a quantum dot semiconductor

Before understanding the electronic structure of a quantum dot semiconductor, it is important to understand what a quantum dot nanoparticle is. We earlier studied that a nanoparticle is any particle with one of its dimensions in the 1 - 100 nm. A quantum dot is a nanoparticle with its diameter on the order of the materials exciton Bohr radius. Quantum dots are typically 2 - 10 nm wide and approximately consist of 10 to 50 atoms. With this understanding of a quantum dot semiconductor, the electronic structure of a quantum dot semiconductor can be described by the following terms.

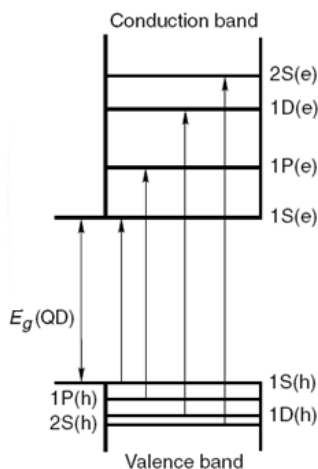


**Figure 7.46:** Energy levels in quantum dot. Allowed optical transitions are shown. Adapted from T. Pradeep, *Nano: The Essentials. Understanding Nanoscience and Nanotechnology*, Tata McGraw-Hill, New Delhi (2007).

#### 7.4.2.3.2.1 Quantum confinement

When the size of the semiconductor crystal becomes comparable or smaller than the exciton Bohr radius, the quantum dots are in a state of quantum confinement. As a result of quantum confinement, the energy levels in a quantum dot are discrete (Figure 7.46) as opposed to being continuous in a bulk crystal (Figure 7.45).

#### 7.4.2.3.2.2 Discrete energy levels

In materials that have small number of atoms and are considered as quantum confined, the energy levels are separated by an appreciable amount of energy such that they are not continuous, but are discrete (see Figure 7.46). The energy associated with an electron (equivalent to conduction band energy level) is given by is given by (7.13), where  $h$  is the Planck's constant,  $m_e$  is the effective mass of electron and  $n$  is the quantum number for the conduction band states, and  $n$  can take the values 1, 2, 3 and so on. Similarly, the energy associated with the hole (equivalent to valence band energy level) is given by (7.14), where  $n'$  is the quantum number for the valence states, and  $n'$  can take the values 1, 2, 3, and so on. The energy increases as one goes higher in the quantum number. Since the electron mass is much smaller than that of the hole, the electron levels are separated more widely than the hole levels.

$$E^e = \frac{h^2 n^2}{8\pi^2 m_e d^2} \quad (7.13)$$

$$E^h = \frac{h^2 n'^2}{8\pi^2 m_h d^2} \quad (7.14)$$

#### 7.4.2.3.2.3 Tunable band gap

As seen from (7.13) and (7.14), the energy levels are affected by the diameter of the semiconductor particles. If the diameter is very small, since the energy is dependent on inverse of diameter squared, the energy levels of the upper edge of the band gap (lowest conduction band level) and lower edge of the band gap (highest valence band level) change significantly with the diameter of the particle and the effective mass of the electron and the hole, resulting in a size dependent tunable band gap. This also results in the discretization of the energy levels.

Qualitatively, this can be understood in the following way. In a bulk semiconductor, the addition or removal of an atom is insignificant compared to the size of the bulk semiconductor, which consists of a large number of atoms. The large size of bulk semiconductors makes the changes in band gap so negligible on the addition of an atom, that it is considered as a fixed band gap. In a quantum dot, addition of an atom does make a difference, resulting in the tunability of band gap.

#### 7.4.2.3.3 UV-visible absorbance

Due to the presence of discrete energy levels in a QD, there is a widening of the energy gap between the highest occupied electronic states and the lowest unoccupied states as compared to the bulk material. As a consequence, the optical properties of the semiconductor nanoparticles also become size dependent.

The minimum energy required to create an exciton is the defined by the band gap of the material, i.e., the energy required to excite an electron from the highest level of valence energy states to the lowest level of the conduction energy states. For a quantum dot, the bandgap varies with the size of the particle. From (7.13) and (7.14), it can be inferred that the band gap becomes higher as the particle becomes smaller. This means that for a smaller particle, the energy required for an electron to get excited is higher. The relation between energy and wavelength is given by (7.15), where  $h$  is the Planck's constant,  $c$  is the speed of light,  $\lambda$

is the wavelength of light. Therefore, from (7.15) to cross a bandgap of greater energy, shorter wavelengths of light are absorbed, i.e., a blue shift is seen.

$$E = \frac{hc}{\lambda} \quad (7.15)$$

For Group 12-16 semiconductors, the bandgap energy falls in the UV-visible range. That is ultraviolet light or visible light can be used to excite an electron from the ground valence states to the excited conduction states. In a bulk semiconductor the band gap is fixed, and the energy states are continuous. This results in a rather uniform absorption spectrum (Figure 7.47a).

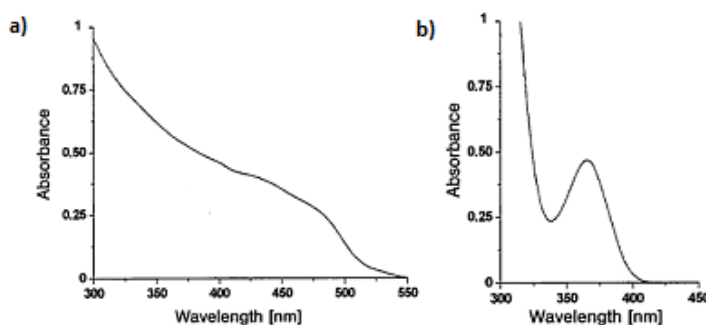


**Figure 7.47:** UV-vis spectra of (a) bulk CdS and (b) 4 nm CdS. Adapted from G. Kickelbick, *Hybrid Materials: Synthesis, Characterization and Applications*, Wiley-VCH, Weinheim (2007).

In the case of Group 12-16 quantum dots, since the bandgap can be changed with the size, these materials can absorb over a range of wavelengths. The peaks seen in the absorption spectrum (Figure 7.47b) correspond to the optical transitions between the electron and hole levels. The minimum energy and thus the maximum wavelength peak corresponds to the first exciton peak or the energy for an electron to get excited from the highest valence state to the lowest conduction state. The quantum dot will not absorb wavelengths of energy longer than this wavelength. This is known as the absorption onset.

#### 7.4.2.3.4 Fluorescence

Fluorescence is the emission of electromagnetic radiation in the form of light by a material that has absorbed a photon. When a semiconductor quantum dot (QD) absorbs a photon/energy equal to or greater than its band gap, the electrons in the QD's get excited to the conduction state. This excited state is however not stable. The electron can relax back to its ground state by either emitting a photon or lose energy via heat losses. These processes can be divided into two categories – radiative decay and non-radiative decay. Radiative decay is the loss of energy through the emission of a photon or radiation. Non-radiative decay involves the loss of heat through lattice vibrations and this usually occurs when the energy difference between the levels is small. Non-radiative decay occurs much faster than radiative decay.

Usually the electron relaxes to the ground state through a combination of both radiative and non-radiative decays. The electron moves quickly through the conduction energy levels through small non-radiative decays and the final transition across the band gap is via a radiative decay. Large nonradiative decays don't occur across the band gap because the crystal structure can't withstand large vibrations without breaking the bonds of the crystal. Since some of the energy is lost through the non-radiative decay, the energy of the emitted photon, through the radiative decay, is much lesser than the absorbed energy. As a result the

wavelength of the emitted photon or fluorescence is longer than the wavelength of absorbed light. This energy difference is called the Stokes shift. Due this Stokes shift, the emission peak corresponding to the absorption band edge peak is shifted towards a higher wavelength (lower energy), i.e., Figure 7.48.

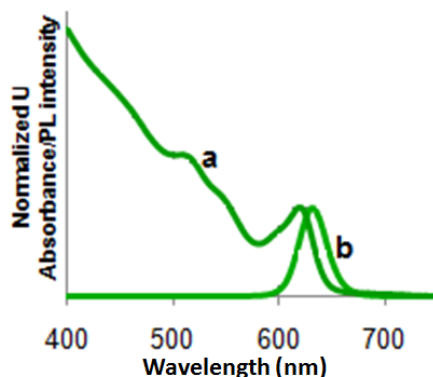


**Figure 7.48:** Absorption spectra (a) and emission spectra (b) of CdSe tetrapod.

Intensity of emission versus wavelength is a bell-shaped Gaussian curve. As long as the excitation wavelength is shorter than the absorption onset, the maximum emission wavelength is independent of the excitation wavelength. Figure 7.48 shows a combined absorption and emission spectrum for a typical CdSe tetrapod.

#### 7.4.2.3.5 Factors affecting the optical properties of NPs

There are various factors that affect the absorption and emission spectra for Group 12-16 semiconductor quantum crystals. Fluorescence is much more sensitive to the background, environment, presence of traps and the surface of the QDs than UV-visible absorption. Some of the major factors influencing the optical properties of quantum nanoparticles include:

- **Surface defects, imperfection of lattice, surface charges** – The surface defects and imperfections in the lattice structure of semiconductor quantum dots occur in the form of unsatisfied valencies. Similar to surface charges, unsatisfied valencies provide a sink for the charge carriers, resulting in unwanted recombinations.
- **Surface ligands** – The presence of surface ligands is another factor that affects the optical properties. If the surface ligand coverage is a 100%, there is a smaller chance of surface recombinations to occur.
- **Solvent polarity** – The polarity of solvents is very important for the optical properties of the nanoparticles. If the quantum dots are prepared in organic solvent and have an organic surface ligand, the more non-polar the solvent, the particles are more dispersed. This reduces the loss of electrons through recombinations again, since when particles come in close proximity to each other, increases the non-radiative decay events.

#### 7.4.2.3.6 Applications of the optical properties of Group 12-16 semiconductor NPs

The size dependent optical properties of NP's have many applications from biomedical applications to solar cell technology, from photocatalysis to chemical sensing. Most of these applications use the following unique properties.

For applications in the field of nanoelectronics, the sizes of the quantum dots can be tuned to be comparable to the scattering lengths, reducing the scattering rate and hence, the signal to noise ratio. For Group 12-16 QDs to be used in the field of solar cells, the bandgap of the particles can be tuned so as to form absorb energy over a large range of the solar spectrum, resulting in more number of excitons and hence more electricity. Since the nanoparticles are so small, most of the atoms are on the surface. Thus, the surface to volume ratio is very large for the quantum dots. In addition to a high surface to volume ratio, the Group 12-16 QDs respond to light energy. Thus quantum dots have very good photocatalytic properties. Quantum dots show fluorescence properties, and emit visible light when excited. This property can be used for applications as biomarkers. These quantum dots can be tagged to drugs to monitor the path of the drugs. Specially shaped Group 12-16 nanoparticles such as hollow shells can be used as drug delivery agents. Another use for the fluorescence properties of Group 12-16 semiconductor QDs is in color-changing paints, which can change colors according to the light source used.

#### 7.4.2.3.7 Bibliography

- M. J. Schulz, V. N. Shanov, and Y. Yun, *Nanomedicine - Design of Particles, Sensors, Motors, Implants, Robots, and Devices*, Artech House, London (2009).
- S. V. Gapoenko, *Optical Properties of Semiconductor Nanocrystals*, Cambridge University Press, Cambridge (2003).
- T. Pradeep, *Nano: The Essentials. Understanding Nanoscience and Nanotechnology*, Tata McGraw-Hill, New Delhi (2007).
- G. Schmid, *Nanoparticles: From Theory to Application*, Wiley-VCH, Weinheim (2004).
- A. L. Rogach, *Semiconductor Nanocrystal Quantum Dots. Synthesis, Assembly, Spectroscopy and Applications*, Springer Wien, New York (2008).
- G. Kickelbick, *Hybrid Materials: Synthesis, Characterization and Applications*, Wiley-VCH, Weinheim (2007).

### 7.4.3 Characterization of Group 12-16 (II-VI) Semiconductor Nanoparticles by UV-visible Spectroscopy<sup>10</sup>

Quantum dots (QDs) as a general term refer to nanocrystals of semiconductor materials, in which the size of the particles are comparable to the natural characteristic separation of an electron-hole pair, otherwise known as the exciton Bohr radius of the material. When the size of the semiconductor nanocrystal becomes this small, the electronic structure of the crystal is governed by the laws of quantum physics. Very small Group 12-16 (II-VI) semiconductor nanoparticle quantum dots, in the order of 2 - 10 nm, exhibit significantly different optical and electronic properties from their bulk counterparts. The characterization of size dependent optical properties of Group 12-16 semiconductor particles provide a lot of qualitative and quantitative information about them – size, quantum yield, monodispersity, shape and presence of surface defects. A combination of information from both the UV-visible absorption and fluorescence, complete the analysis of the optical properties.

#### 7.4.3.1 UV-visible absorbance spectroscopy

Absorption spectroscopy, in general, refers to characterization techniques that measure the absorption of radiation by a material, as a function of the wavelength. Depending on the source of light used, absorption spectroscopy can be broadly divided into infrared and UV-visible spectroscopy. The band gap of Group 12-16 semiconductors is in the UV-visible region. This means the minimum energy required to excite an electron from the valence states of the Group 12-16 semiconductor QDs to its conduction states, lies in the UV-visible region. This is also a reason why most of the Group 12-16 semiconductor quantum dot solutions are colored.

<sup>10</sup>This content is available online at <<http://cnx.org/content/m34601/1.1/>>.

This technique is complementary to fluorescence spectroscopy, in that UV-visible spectroscopy measures electronic transitions from the ground state to the excited state, whereas fluorescence deals with the transitions from the excited state to the ground state. In order to characterize the optical properties of a quantum dot, it is important to characterize the sample with both these techniques

In quantum dots, due to the very small number of atoms, the addition or removal of one atom to the molecule changes the electronic structure of the quantum dot dramatically. Taking advantage of this property in Group 12-16 semiconductor quantum dots, it is possible to change the band gap of the material by just changing the size of the quantum dot. A quantum dot can absorb energy in the form of light over a range of wavelengths, to excite an electron from the ground state to its excited state. The minimum energy that is required to excite an electron, is dependent on the band gap of the quantum dot. Thus, by making accurate measurements of light absorption at different wavelengths in the ultraviolet and visible spectrum, a correlation can be made between the band gap and size of the quantum dot. Group 12-16 semiconductor quantum dots are of particular interest, since their band gap lies in the visible region of the solar spectrum.

The UV-visible absorbance spectroscopy is a characterization technique in which the absorbance of the material is studied as a function of wavelength. The visible region of the spectrum is in the wavelength range of 380 nm (violet) to 740 nm (red) and the near ultraviolet region extends to wavelengths of about 200 nm. The UV-visible spectrophotometer analyzes over the wavelength range 200 – 900 nm.

When the Group 12-16 semiconductor nanocrystals are exposed to light having an energy that matches a possible electronic transition as dictated by laws of quantum physics, the light is absorbed and an exciton pair is formed. The UV-visible spectrophotometer records the wavelength at which the absorption occurs along with the intensity of the absorption at each wavelength. This is recorded in a graph of absorbance of the nanocrystal versus wavelength.

### 7.4.3.2 Instrumentation

A working schematic of the UV-visible spectrophotometer is shown in Figure 7.49.

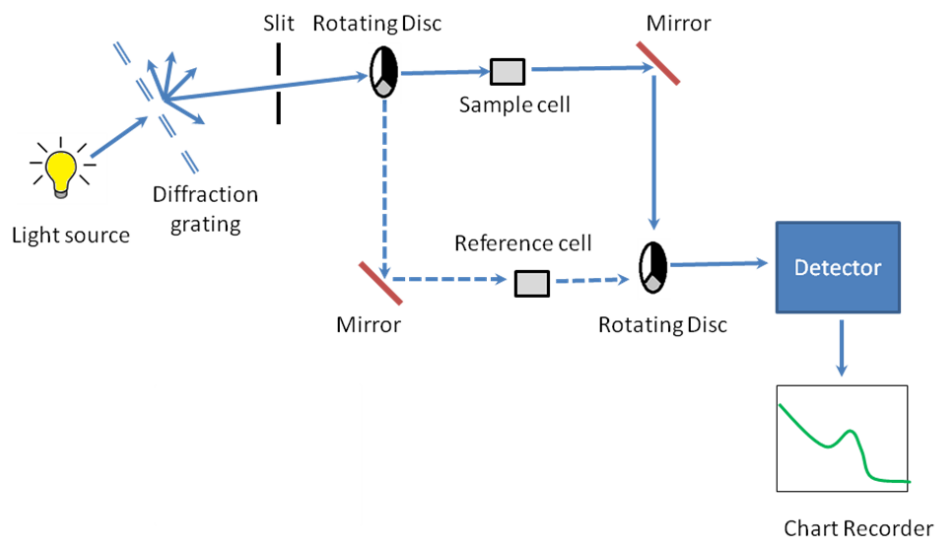


**Figure 7.49:** Schematic of UV-visible spectrophotometer.

### 7.4.3.2.1 The light source

Since it is a UV-vis spectrophotometer, the light source (Figure 7.49) needs to cover the entire visible and the near ultra-violet region (200 - 900 nm). Since it is not possible to get this range of wavelengths from a single lamp, a combination of a deuterium lamp for the UV region of the spectrum and tungsten or halogen lamp for the visible region is used. This output is then sent through a diffraction grating as shown in the schematic.

### 7.4.3.2.2 The diffraction grating and the slit

The beam of light from the visible and/or UV light source is then separated into its component wavelengths (like a very efficient prism) by a diffraction grating (Figure 7.49). Following the slit is a slit that sends a monochromatic beam into the next section of the spectrophotometer.

### 7.4.3.2.3 Rotating discs

Light from the slit then falls onto a rotating disc (Figure 7.49). Each disc consists of different segments – an opaque black section, a transparent section and a mirrored section. If the light hits the transparent section, it will go straight through the sample cell, get reflected by a mirror, hits the mirrored section of a second rotating disc, and then collected by the detector. Else if the light hits the mirrored section, gets reflected by a mirror, passes through the reference cell, hits the transparent section of a second rotating disc and then collected by the detector. Finally if the light hits the black opaque section, it is blocked and no light passes through the instrument, thus enabling the system to make corrections for any current generated by the detector in the absence of light.

### 7.4.3.2.4 Sample cell, reference cell and sample preparation

For liquid samples, a square cross section tube sealed at one end is used. The choice of cuvette depends on the following factors:

- **Type of solvent** - For aqueous samples, specially designed rectangular quartz, glass or plastic cuvettes are used. For organic samples glass and quartz cuvettes are used.
- **Excitation wavelength** – Depending on the size and thus, bandgap of the 12-16 semiconductor nanoparticles, different excitation wavelengths of light are used. Depending on the excitation wavelength, different materials are used

Cuvette	Wavelength (nm)
Visible only glass	380 - 780
Visible only plastic	380 - 780
UV plastic	220 - 780
Quartz	200 - 900

**Table 7.3:** Cuvette materials and their wavelengths.

- **Cost** – Plastic cuvettes are the least expensive and can be discarded after use. Though quartz cuvettes have the maximum utility, they are the most expensive, and need to be reused. Generally, disposable plastic cuvettes are used when speed is more important than high accuracy.

The best cuvettes need to be very clear and have no impurities that might affect the spectroscopic reading. Defects on the cuvette such as scratches, can scatter light and hence should be avoided. Some cuvettes are clear only on two sides, and can be used in the UV-Visible spectrophotometer, but cannot be used for

fluorescence spectroscopy measurements. For Group 12-16 semiconductor nanoparticles prepared in organic solvents, the quartz cuvette is chosen.

In the sample cell the quantum dots are dispersed in a solvent, whereas in the reference cell the pure solvent is taken. It is important that the sample be very dilute (maximum first exciton absorbance should not exceed 1 au) and the solvent is not UV-visible active. For these measurements, it is required that the solvent does not have characteristic absorption or emission in the region of interest. Solution phase experiments are preferred, though it is possible to measure the spectra in the solid state also using thin films, powders, etc. The instrumentation for solid state UV-visible absorption spectroscopy is slightly different from the solution phase experiments and is beyond the scope of discussion.

#### 7.4.3.2.5 Detector

Detector converts the light into a current signal that is read by a computer. Higher the current signal, greater is the intensity of the light. The computer then calculates the absorbance using the in (7.16), where A denotes absorbance, I is sample cell intensity and  $I_0$  is the reference cell intensity.

$$A = \log_{10}(I_0/I) \quad (7.16)$$

The following cases are possible:

- Where  $I < I_0$  and  $A < 0$ . This usually occurs when the solvent absorbs in the wavelength range. Preferably the solvent should be changed, to get an accurate reading for actual reference cell intensity.
- Where  $I = I_0$  and  $A = 0$ . This occurs when pure solvent is put in both reference and sample cells. This test should always be done before testing the sample, to check for the cleanliness of the cuvettes.
- When  $A = 1$ . This occurs when 90% of the light at a particular wavelength has been absorbed, which means that only 10% is seen at the detector. So  $I_0/I$  becomes  $100/10 = 10$ .  $\log_{10}$  of 10 is 1.
- When  $A > 1$ . This occurs in extreme case where more than 90% of the light is absorbed.

#### 7.4.3.2.6 Output

The output is the form of a plot of absorbance against wavelength, e.g., Figure 7.50.

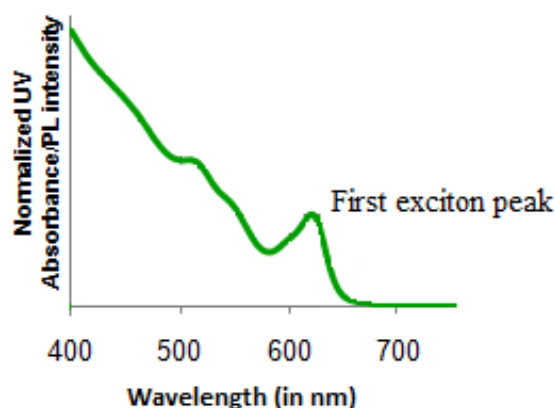


**Figure 7.50:** Representative UV-visible absorption spectrum for CdSe tetrapods.

### 7.4.3.3 Beer-Lambert law

In order to make comparisons between different samples, it is important that all the factors affecting absorbance should be constant except the sample itself.

#### 7.4.3.3.1 Effect of concentration on absorbance

The extent of absorption depends on the number of absorbing nanoparticles or in other words the concentration of the sample. If it is a reasonably concentrated solution, it will have a high absorbance since there are lots of nanoparticles to interact with the light. Similarly in an extremely dilute solution, the absorbance is very low. In order to compare two solutions, it is important that we should make some allowance for the concentration.

#### 7.4.3.3.2 Effect of container shape

Even if we had the same concentration of solutions, if we compare two solutions – one in a rectangular shaped container (e.g., Figure 7.51) so that light travelled 1 cm through it and the other in which the light travelled 100 cm through it, the absorbance would be different. This is because if the length the light travelled is greater, it means that the light interacted with more number of nanocrystals, and thus has a higher absorbance. Again, in order to compare two solutions, it is important that we should make some allowance for the concentration.



**Figure 7.51:** A typical rectangular cuvette for UV-visible spectroscopy.

---

#### 7.4.3.3.3 The law

The Beer-Lambert law addresses the effect of concentration and container shape as shown in (7.16), (7.17) and (7.18), where  $A$  denotes absorbance;  $\epsilon$  is the molar absorptivity or molar absorption coefficient;  $l$  is the path length of light (in cm); and  $c$  is the concentration of the solution ( $\text{mol}/\text{dm}^3$ ).

$$\log_{10}(I_0/I) = \epsilon lc \tag{7.17}$$

$$A = \epsilon lc \tag{7.18}$$

#### 7.4.3.3.4 Molar absorptivity

From the Beer-Lambert law, the molar absorptivity ' $\epsilon$ ' can be expressed as shown in (7.19).

$$c = A/\ell\epsilon \quad (7.19)$$

Molar absorptivity corrects for the variation in concentration and length of the solution that the light passes through. It is the value of absorbance when light passes through 1 cm of a 1 mol/dm<sup>3</sup> solution.

#### 7.4.3.3.5 Limitations of Beer-Lambert law

The linearity of the Beer-Lambert law is limited by chemical and instrumental factors.

- At high concentrations (> 0.01 M), the relation between absorptivity coefficient and absorbance is no longer linear. This is due to the electrostatic interactions between the quantum dots in close proximity.
- If the concentration of the solution is high, another effect that is seen is the scattering of light from the large number of quantum dots.
- The spectrophotometer performs calculations assuming that the refractive index of the solvent does not change significantly with the presence of the quantum dots. This assumption only works at low concentrations of the analyte (quantum dots).
- Presence of stray light.

#### 7.4.3.4 Analysis of data

The data obtained from the spectrophotometer is a plot of absorbance as a function of wavelength. Quantitative and qualitative data can be obtained by analysing this information

##### 7.4.3.4.1 Quantitative Information

The band gap of the semiconductor quantum dots can be tuned with the size of the particles. The minimum energy for an electron to get excited from the ground state is the energy to cross the band gap. In an absorption spectra, this is given by the first exciton peak at the maximum wavelength ( $\lambda_{\max}$ ).

##### 7.4.3.4.1.1 Size of the quantum dots

The size of quantum dots can be approximated corresponding to the first exciton peak wavelength. Empirical relationships have been determined relating the diameter of the quantum dot to the wavelength of the first exciton peak. The Group 12-16 semiconductor quantum dots that they studied were cadmium selenide (CdSe), cadmium telluride (CdTe) and cadmium sulfide (CdS). The empirical relationships are determined by fitting experimental data of absorbance versus wavelength of known sizes of particles. The empirical equations determined are given for CdTe, CdSe, and CdS in (7.20), (7.21) and (7.22) respectively, where  $D$  is the diameter and  $\lambda$  is the wavelength corresponding to the first exciton peak. For example, if the first exciton peak of a CdSe quantum dot is 500 nm, the corresponding diameter of the quantum dot is 2.345 nm and for a wavelength of 609 nm, the corresponding diameter is 5.008 nm.

$$D = (9.8127 \times 10^{-7})\lambda^3 - (1.7147 \times 10^{-3})\lambda^2 + (1.0064)\lambda - 194.84 \quad (7.20)$$

$$D = (1.6122 \times 10^{-7})\lambda^3 - (2.6575 \times 10^{-6})\lambda^2 + (1.6242 \times 10^{-3})\lambda + 41.57 \quad (7.21)$$

$$D = (-6.6521 \times 10^{-8})\lambda^3 + (1.9577 \times 10^{-4})\lambda^2 - (9.2352 \times 10^{-2})\lambda + 13.29 \quad (7.22)$$

#### 7.4.3.4.1.2 Concentration of sample

Using the Beer-Lambert law, it is possible to calculate the concentration of the sample if the molar absorptivity for the sample is known. The molar absorptivity can be calculated by recording the absorbance of a standard solution of  $1 \text{ mol/dm}^3$  concentration in a standard cuvette where the light travels a constant distance of 1 cm. Once the molar absorptivity and the absorbance of the sample are known, with the length the light travels being fixed, it is possible to determine the concentration of the sample solution.

Empirical equations can be determined by fitting experimental data of extinction coefficient per mole of Group 12-16 semiconductor quantum dots, at  $250^\circ\text{C}$ , to the diameter of the quantum dot, (7.23), (7.24), and (7.25).

$$\varepsilon = 10043 \times D^{2.12} \quad (7.23)$$

$$\varepsilon = 5857 \times D^{2.65} \quad (7.24)$$

$$\varepsilon = 21536 \times D^{2.3} \quad (7.25)$$

The concentration of the quantum dots can then be determined by using the Beer Lambert law as given by (7.19).

#### 7.4.3.4.2 Qualitative Information

Apart from quantitative data such as the size of the quantum dots and concentration of the quantum dots, a lot of qualitative information can be derived from the absorption spectra.

##### 7.4.3.4.2.1 Size distribution

If there is a very narrow size distribution, the first exciton peak will be very sharp (Figure 7.52). This is because due to the narrow size distribution, the differences in band gap between different sized particles will be very small and hence most of the electrons will get excited over a smaller range of wavelengths. In addition, if there is a narrow size distribution, the higher exciton peaks are also seen clearly.

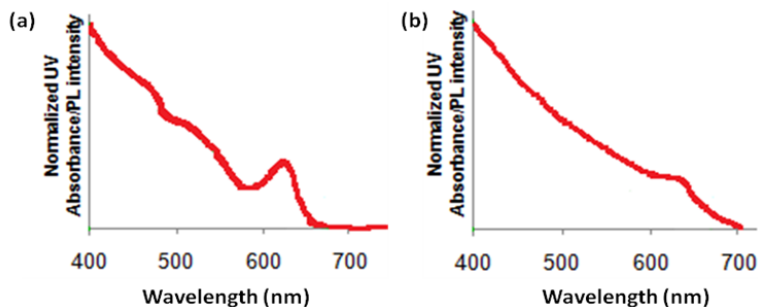
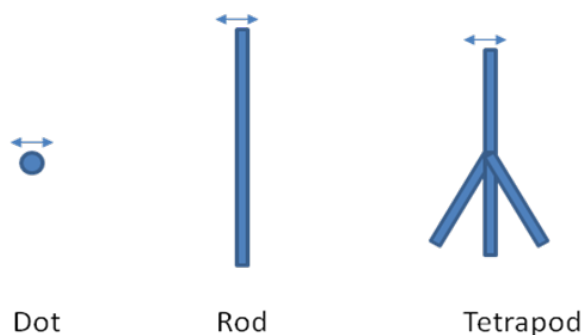


Figure 7.52: Narrow emission spectra (a) and broad emission spectra (b) of CdSe QDs.

#### 7.4.3.4.2 Shaped particles

In the case of a spherical quantum dot, in all dimensions, the particle is quantum confined (Figure 7.53). In the case of a nanorod, whose length is not in the quantum regime, the quantum effects are determined by the width of the nanorod. Similar is the case in tetrapods or four legged structures. The quantum effects are determined by the thickness of the arms. During the synthesis of the shaped particles, the thickness of the rod or the arm of the tetrapod does not vary among the different particles, as much as the length of the rods or arms changes. Since the thickness of the rod or tetrapod is responsible for the quantum effects, the absorption spectrum of rods and tetrapods has sharper features as compared to a quantum dot. Hence, qualitatively it is possible to differentiate between quantum dots and other shaped particles.



**Figure 7.53:** Different shaped nanoparticles with the arrows indicating the dimension where quantum confinement effects are observed.

---

#### 7.4.3.4.2.3 Crystal lattice information

In the case of CdSe semiconductor quantum dots it has been shown that it is possible to estimate the crystal lattice of the quantum dot from the adsorption spectrum (Figure 7.54), and hence determine if the structure is zinc blend or wurtzite.

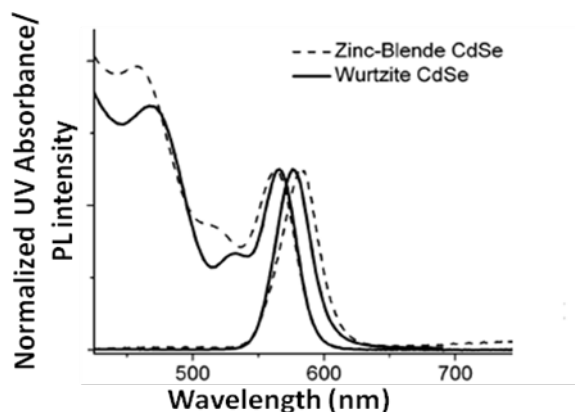


**Figure 7.54:** Zinc blende and wurtzite CdSe absorption spectra. Adapted from J. Jasieniak, C. Bullen, J. van Embden, and P. Mulvaney, *J. Phys. Chem. B*, 2005, **109**, 20665.

### 7.4.3.5 UV-vis absorption spectra of Group 12-16 semiconductor nanoparticles

#### 7.4.3.5.1 Cadmium selenide

Cadmium selenide (CdSe) is one of the most popular Group 12-16 semiconductors. This is mainly because the band gap (712 nm or 1.74 eV) energy of CdSe. Thus, the nanoparticles of CdSe can be engineered to have a range of band gaps throughout the visible range, corresponding to the major part of the energy that comes from the solar spectrum. This property of CdSe along with its fluorescing properties is used in a variety of applications such as solar cells and light emitting diodes. Though cadmium and selenium are known carcinogens, the harmful biological effects of CdSe can be overcome by coating the CdSe with a layer of zinc sulfide. Thus CdSe, can also be used as bio-markers, drug-delivery agents, paints and other applications.

A typical absorption spectrum of narrow size distribution wurtzite CdSe quantum dot is shown in Figure 7.55. A size evolving absorption spectra is shown in Figure 7.56. However, a complete analysis of the sample is possible only by also studying the fluorescence properties of CdSe.

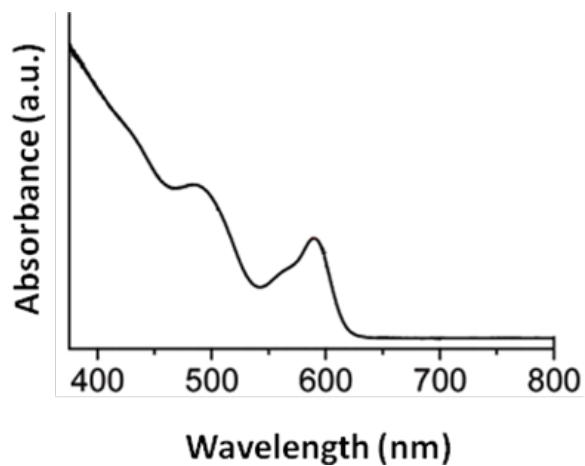


**Figure 7.55:** Wurtzite CdSe quantum dot. Adapted from X. Zhong, Y. Feng, and Y. Zhang, *J. Phys. Chem. C*, 2007, 111, 526.

---

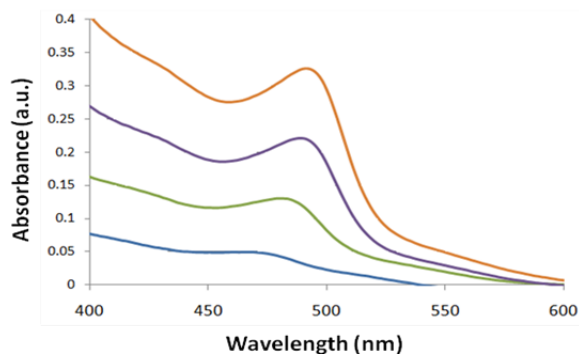


**Figure 7.56:** Size evolving absorption spectra of CdSe quantum dots.

---

#### 7.4.3.5.2 Cadmium telluride (CdTe)

Cadmium telluride has a band gap of 1.44 eV (860 nm) and as such it absorbs in the infrared region. Like CdSe, the sizes of CdTe can be engineered to have different band edges and thus, different absorption spectra as a function of wavelength. A typical CdTe spectra is shown in Figure 7.57. Due to the small bandgap energy of CdTe, it can be used in tandem with CdSe to absorb in a greater part of the solar spectrum.

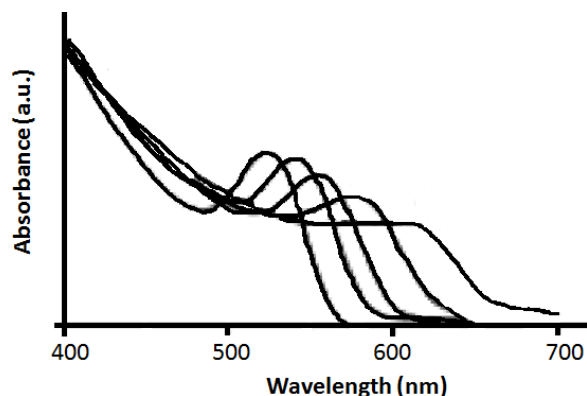


**Figure 7.57:** Size evolving absorption spectra of CdTe quantum dots from 3 nm to 7 nm. Adapted from C. Qi-Fan, W. Wen-Xing, G. Ying-Xin, L. Meng-Ying, X. Shu-Kun and Z. Xiu-Juan, *Chin. J. Anal. Chem.*, 2007, **35**, 135.

#### 7.4.3.5.3 Other Group 12-16 semiconductor systems

Table 7.4 shows the bulk band gap of other Group 12-16 semiconductor systems. The band gap of ZnS falls in the UV region, while those of ZnSe, CdS, and ZnTe fall in the visible region.

Material	Band gap (eV)	Wavelength (nm)
ZnS	3.61	343.2
ZnSe	2.69	460.5
ZnTe	2.39	518.4
CdS	2.49	497.5
CdSe	1.74	712.1
CdTe	1.44	860.3

**Table 7.4:** Bulk band gaps of different Group 12-16 semiconductors.

#### 7.4.3.5.4 Heterostructures of Group 12-16 semiconductor systems

It is often desirable to have a combination of two Group 12-16 semiconductor system quantum heterostructures of different shapes like dots and tetrapods, for applications in solar cells, bio-markers, etc. Some of the most interesting systems are ZnS shell-CdSe core systems, such as the CdSe/CdS rods and tetrapods.

Figure 7.58 shows a typical absorption spectra of CdSe-ZnS core-shell system. This system is important because of the drastically improved fluorescence properties because of the addition of a wide band gap ZnS shell than the core CdSe. In addition with a ZnS shell, CdSe becomes bio-compatible.

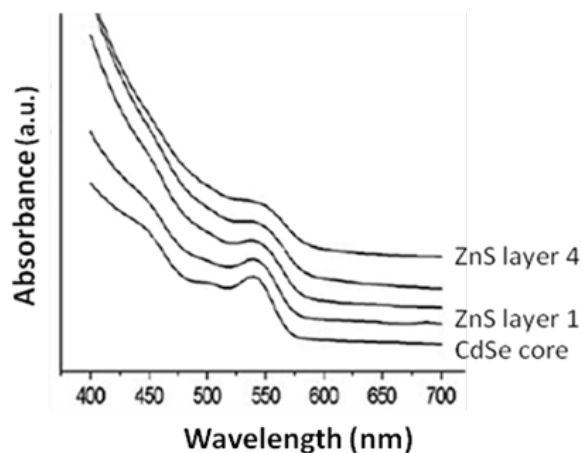


**Figure 7.58:** Absorption spectra of CdSe core, ZnS shell. Adapted from C. Qing-Zhu, P. Wang, X. Wang and Y. Li, *Nanoscale Res. Lett.*, 2008, **3**, 213.

A CdSe seed, CdS arm nanorods system is also interesting. Combining CdSe and CdS in a single nanostructure creates a material with a mixed dimensionality where holes are confined to CdSe while electrons can move freely between CdSe and CdS phases.

#### 7.4.3.6 Bibliography

- S. V. Gapoenko, *Optical Properties of Semiconductor Nanocrystals*, Cambridge University Press, Cambridge (2003).
- W. W. Yu, L. Qu, W. Guo, and X. Peng, *Chem. Mater.*, 2003, **15**, 2854.
- J. Jasieniak, C. Bullen, J. van Embden, and P. Mulvaney, *J. Phys. Chem. B*, 2005, **109**, 20665.
- X. Zhong, Y. Feng, and Y. Zhang, *J. Phys. Chem. C*, 2007, **111**, 526.
- D. V. Talapin, J. H. Nelson, E. V. Shevchenko, S. Aloni, B. Sadtler, and A. P. Alivisatos, *Nano Lett.*, 2007, **7**, 2951.
- C. Qing-Zhu, P. Wang, X. Wang, and Y. Li, *Nanoscale Res. Lett.*, 2008, **3**, 213.
- C. Qi-Fan, W. Wen-Xing, G. Ying-Xin, L. Meng-Ying, X. Shu-Kun, and Z. Xiu-Juan, *Chin. J. Anal. Chem.*, 2007, **35**, 135.

### 7.4.4 Optical Characterization of Group 12-16 (II-VI) Semiconductor Nanoparticles by Fluorescence Spectroscopy<sup>11</sup>

Group 12-16 semiconductor nanocrystals when exposed to light of a particular energy absorb light to excite electrons from the ground state to the excited state, resulting in the formation of an electron-hole pair (also known as excitons). The excited electrons relax back to the ground state, mainly through radiative emission of energy in the form of photons.

Quantum dots (QD) refer to nanocrystals of semiconductor materials where the size of the particles is comparable to the natural characteristic separation of an electron-hole pair, otherwise known as the exciton Bohr radius of the material. In quantum dots, the phenomenon of emission of photons associated with the transition of electrons from the excited state to the ground state is called fluorescence.

<sup>11</sup>This content is available online at <<http://cnx.org/content/m34656/1.1/>>.

#### 7.4.4.1 Fluorescence spectroscopy

Emission spectroscopy, in general, refers to a characterization technique that measures the emission of radiation by a material that has been excited. Fluorescence spectroscopy is one type of emission spectroscopy which records the intensity of light radiated from the material as a function of wavelength. It is a non-destructive characterization technique.

After an electron is excited from the ground state, it needs to relax back to the ground state. This relaxation or loss of energy to return to the ground state, can be achieved by a combination of non-radiative decay (loss of energy through heat) and radiative decay (loss of energy through light). Non-radiative decay by vibrational modes typically occurs between energy levels that are close to each other. Radiative decay by the emission of light occurs when the energy levels are far apart like in the case of the band gap. This is because loss of energy through vibrational modes across the band gap can result in breaking the bonds of the crystal. This phenomenon is shown in Figure 7.59.

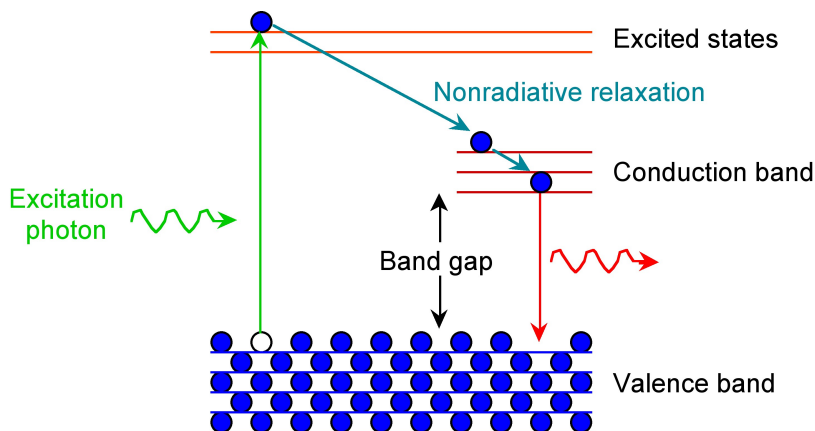


**Figure 7.59:** Emission of luminescence photon for Group 12-16 semiconductor quantum dot.

The band gap of Group 12-16 semiconductors is in the UV-visible region. Thus, the wavelength of the emitted light as a result of radiative decay is also in the visible region, resulting in fascinating fluorescence properties.

A fluorimeter is a device that records the fluorescence intensity as a function of wavelength. The fluorescence quantum yield can then be calculated by the ratio of photons absorbed to photons emitted by the system. The quantum yield gives the probability of the excited state getting relaxed via fluorescence rather than by any other non-radiative decay.

#### 7.4.4.2 Difference between fluorescence and phosphorescence

Photoluminescence is the emission of light from any material due to the loss of energy from excited state to ground state. There are two main types of luminescence – fluorescence and phosphorescence. Fluorescence is a fast decay process, where the emission rate is around  $10^8 \text{ s}^{-1}$  and the lifetime is around  $10^{-9} - 10^{-7} \text{ s}$ . Fluorescence occurs when the excited state electron has an opposite spin compared to the ground state electrons. From the laws of quantum mechanics, this is an allowed transition, and occurs rapidly by emission of a photon. Fluorescence disappears as soon as the exciting light source is removed.

Phosphorescence is the emission of light, in which the excited state electron has the same spin orientation as the ground state electron. This transition is a forbidden one and hence the emission rates are slow ( $10^3 -$

$10^0 \text{ s}^{-1}$ ). So the phosphorescence lifetimes are longer, typically seconds to several minutes, while the excited phosphors slowly returned to the ground state. Phosphorescence is still seen, even after the exciting light source is removed. Group 12-16 semiconductor quantum dots exhibit fluorescence properties when excited with ultraviolet light.

### 7.4.4.3 Instrumentation

The working schematic for the fluorometer is shown in Figure 7.60.

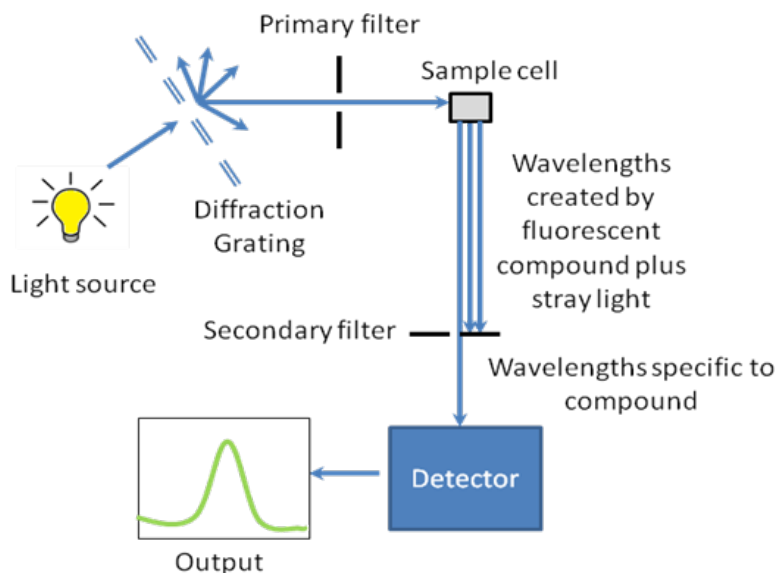


**Figure 7.60:** Schematic of fluorometer.

#### 7.4.4.3.1 The light source

The excitation energy is provided by a light source that can emit wavelengths of light over the ultraviolet and the visible range. Different light sources can be used as excitation sources such as lasers, xenon arcs and mercury-vapor lamps. The choice of the light source depends on the sample. A laser source emits light of a high irradiance at a very narrow wavelength interval. This makes the need for the filter unnecessary, but the wavelength of the laser cannot be altered significantly. The mercury vapor lamp is a discrete line source. The xenon arc has a continuous emission spectrum between the ranges of 300 - 800 nm.

#### 7.4.4.3.2 The diffraction grating and primary filter

The diffraction grating splits the incoming light source into its component wavelengths (Figure 7.60). The monochromator can then be adjusted to choose with wavelengths to pass through. Following the primary filter, specific wavelengths of light are irradiated onto the sample

### 7.4.4.3.3 Sample cell and sample preparation

A proportion of the light from the primary filter is absorbed by the sample. After the sample gets excited, the fluorescent substance returns to the ground state, by emitting a longer wavelength of light in all directions (Figure 7.60). Some of this light passes through a secondary filter. For liquid samples, a square cross section tube sealed at one end and all four sides clear, is used as a sample cell. The choice of cuvette depends on three factors:

1. **Type of solvent** - For aqueous samples, specially designed rectangular quartz, glass or plastic cuvettes are used. For organic samples glass and quartz cuvettes are used.
2. **Excitation wavelength** - Depending on the size and thus, bandgap of the Group 12-16 semiconductor nanoparticles, different excitation wavelengths of light are used. Depending on the excitation wavelength, different materials are used (Table 7.5).

Cuvette	Wavelength (nm)
Visible only glass	380 - 780
Visible only plastic	380 - 780
UV plastic	220 - 780
Quartz	200 - 900

**Table 7.5:** Cuvette materials and their wavelengths.

3. **Cost** - Plastic cuvettes are the least expensive and can be discarded after use. Though quartz cuvettes have the maximum utility, they are the most expensive, and need to be reused. Generally, disposable plastic cuvettes are used when speed is more important than high accuracy.



**Figure 7.61:** A typical cuvette for fluorescence spectroscopy.

The cuvettes have a 1 cm path length for the light (Figure 7.61). The best cuvettes need to be very clear and have no impurities that might affect the spectroscopic reading. Defects on the cuvette, such as scratches, can scatter light and hence should be avoided. Since the specifications of a cuvette are the same for both, the UV-visible spectrophotometer and fluorimeter, the same cuvette that is used to measure absorbance can be used to measure the fluorescence. For Group 12-16 semiconductor nanoparticles prepared in organic solvents, the clear four sided quartz cuvette is used. The sample solution should be dilute (absorbance <math>< 1\text{ au}</math>), to avoid very high signal from the sample to burn out the detector. The solvent used to disperse the nanoparticles should not absorb at the excitation wavelength.

#### 7.4.4.3.4 Secondary filter

The secondary filter is placed at a  $90^\circ$  angle (Figure 7.60) to the original light path to minimize the risk of transmitted or reflected incident light reaching the detector. Also this minimizes the amount of stray light, and results in a better signal-to-noise ratio. From the secondary filter, wavelengths specific to the sample are passed onto the detector.

#### 7.4.4.3.5 Detector

The detector can either be single-channeled or multichanneled (Figure 7.60). The single-channeled detector can only detect the intensity of one wavelength at a time, while the multichanneled detects the intensity at all wavelengths simultaneously, making the emission monochromator or filter unnecessary. The different types of detectors have both advantages and disadvantages.

#### 7.4.4.3.6 Output

The output is the form of a plot of intensity of emitted light as a function of wavelength as shown in Figure 7.62.

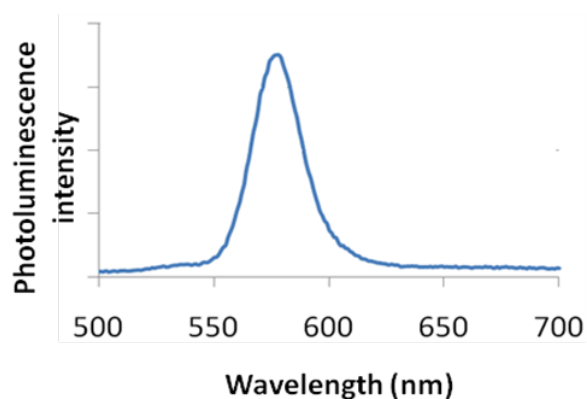


**Figure 7.62:** Emission spectra of CdSe quantum dot.

---

#### 7.4.4.4 Analysis of data

The data obtained from fluorimeter is a plot of fluorescence intensity as a function of wavelength. Quantitative and qualitative data can be obtained by analysing this information.

##### 7.4.4.4.1 Quantitative information

From the fluorescence intensity versus wavelength data, the quantum yield ( $\Phi_F$ ) of the sample can be determined. Quantum yield is a measure of the ratio of the photons absorbed with respect to the photons emitted. It is important for the application of Group 12-16 semiconductor quantum dots using their fluorescence properties, for e.g., bio-markers.

The most well-known method for recording quantum yield is the comparative method which involves the use of well characterized standard solutions. If a test sample and a standard sample have similar absorbance values at the same excitation wavelength, it can be assumed that the number of photons being absorbed by

both the samples is the same. This means that a ratio of the integrated fluorescence intensities of the test and standard sample measured at the same excitation wavelength will give a ratio of quantum yields. Since the quantum yield of the standard solution is known, the quantum yield for the unknown sample can be calculated.

A plot of integrated fluorescence intensity versus absorbance at the excitation wavelength is shown in Figure 7.63. The slope of the graphs shown in Figure 7.63 are proportional to the quantum yield of the different samples. Quantum yield is then calculated using (7.26), where subscripts ST denotes standard sample and X denotes the test sample; QY is the quantum yield; RI is the refractive index of the solvent.

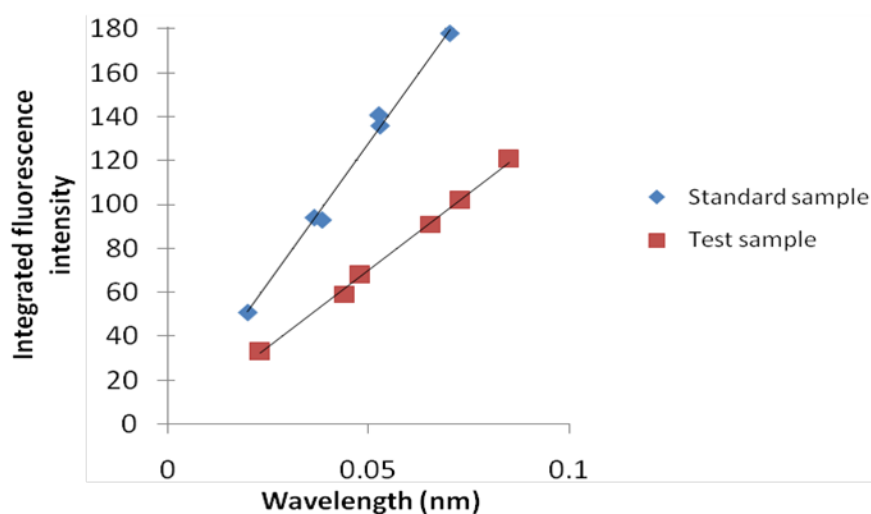


Figure 7.63: Integrated fluorescence intensity as a function of absorbance.

$$\frac{QY_X}{QY_{ST}} = \frac{\text{slope}_X (RI_X)^2}{\text{slope}_{ST} (RI_{ST})^2} \quad (7.26)$$

Take the example of Figure 7.63. If the same solvent is used in both the sample and the standard solution, the ratio of quantum yields of the sample to the standard is given by (7.27). If the quantum yield of the standard is known to 0.95, then the quantum yield of the test sample is 0.523 or 52.3%.

$$\frac{QY_X}{QY_{ST}} = \frac{1.41}{2.56} \quad (7.27)$$

The assumption used in the comparative method is valid only in the Beer-Lambert law linear regime. Beer-Lambert law states that absorbance is directly proportional to the path length of light travelled within the sample, and concentration of the sample. The factors that affect the quantum yield measurements are the following:

- **Concentration** – Low concentrations should be used (absorbance < 0.2 a.u.) to avoid effects such as self quenching.
- **Solvent** – It is important to take into account the solvents used for the test and standard solutions. If the solvents used for both are the same then the comparison is trivial. However, if the solvents in the test and standard solutions are different, this difference needs to be accounted for. This is done by incorporating the solvent refractive indices in the ratio calculation.

- **Standard samples** – The standard samples should be characterized thoroughly. In addition, the standard sample used should absorb at the excitation wavelength of the test sample.
- **Sample preparation** – It is important that the cuvettes used are clean, scratch free and clear on all four sides. The solvents used must be of spectroscopic grade and should not absorb in the wavelength range.
- **Slit width** – The slit widths for all measurements must be kept constant.

The quantum yield of the Group 12-16 semiconductor nanoparticles are affected by many factors such as the following.

- **Surface defects** – The surface defects of semiconductor quantum dots occur in the form of unsatisfied valencies. Thus resulting in unwanted recombinations. These unwanted recombinations reduce the loss of energy through radiative decay, and thus reducing the fluorescence.
- **Surface ligands** – If the surface ligand coverage is a 100%, there is a smaller chance of surface recombinations to occur.
- **Solvent polarity** – If the solvent and the ligand have similar solvent polarities, the nanoparticles are more dispersed, reducing the loss of electrons through recombinations.

#### 7.4.4.4.2 Qualitative Information

Apart from quantum yield information, the relationship between intensity of fluorescence emission and wavelength, other useful qualitative information such as size distribution, shape of the particle and presence of surface defects can be obtained.

As shown in Figure 7.64, the shape of the plot of intensity versus wavelength is a Gaussian distribution. In Figure 7.64, the full width at half maximum (FWHM) is given by the difference between the two extreme values of the wavelength at which the photoluminescence intensity is equal to half its maximum value. From the full width half max (FWHM) of the fluorescence intensity Gaussian distribution, it is possible to determine qualitatively the size distribution of the sample. For a Group 12-16 quantum dot sample if the FWHM is greater than 30, the system is very polydisperse and has a large size distribution. It is desirable for all practical applications for the FWHM to be lesser than 30.

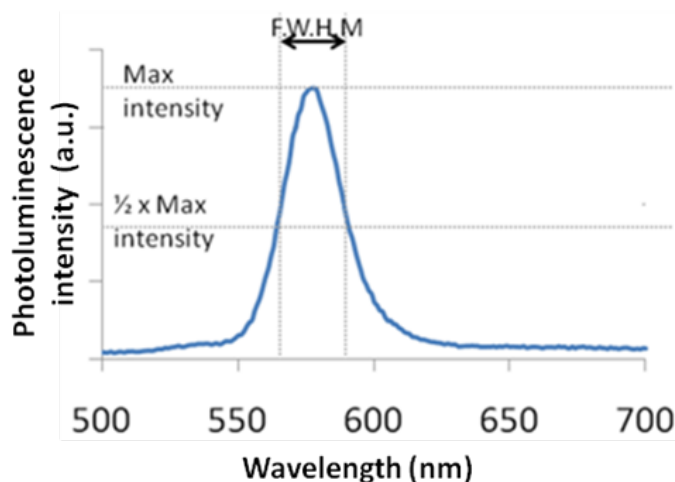


**Figure 7.64:** Emission spectra of CdSe QDs showing the full width half maximum (FWHM).

From the FWHM of the emission spectra, it is also possible to qualitatively get an idea if the particles are spherical or shaped. During the synthesis of the shaped particles, the thickness of the rod or the arm of the tetrapod does not vary among the different particles, as much as the length of the rods or arms changes. The thickness of the arm or rod is responsible for the quantum effects in shaped particles. In the case of quantum dots, the particle is quantum confined in all dimensions. Thus, any size distribution during the synthesis of quantum dots greatly affects the emission spectra. As a result the FWHM of rods and tetrapods is much smaller as compared to a quantum dot. Hence, qualitatively it is possible to differentiate between quantum dots and other shaped particles.

Another indication of branched structures is the decrease in the intensity of fluorescence peaks. Quantum dots have very high fluorescence values as compared to branched particles, since they are quantum confined in all dimensions as compared to just 1 or 2 dimensions in the case of branched particles.

#### 7.4.4.5 Fluorescence spectra of different Group 12-16 semiconductor nanoparticles

The emission spectra of all Group 12-16 semiconductor nanoparticles are Gaussian curves as shown in Figure 7.62 and Figure 7.64. The only difference between them is the band gap energy, and hence each of the Group 12-16 semiconductor nanoparticles fluoresce over different ranges of wavelengths

##### 7.4.4.5.1 Cadmium selenide

Since its bulk band gap (1.74 eV, 712 nm) falls in the visible region cadmium Selenide (CdSe) is used in various applications such as solar cells, light emitting diodes, etc. Size evolving emission spectra of cadmium selenide is shown in Figure 7.65. Different sized CdSe particles have different colored fluorescence spectra. Since cadmium and selenide are known carcinogens and being nanoparticles are easily absorbed into the human body, there is some concern regarding these particles. However, CdSe coated with ZnS can overcome all the harmful biological effects, making cadmium selenide nanoparticles one of the most popular 12-16 semiconductor nanoparticle.

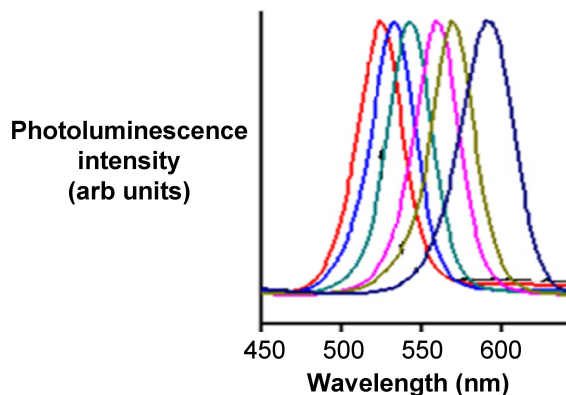


**Figure 7.65:** Size evolving CdSe emission spectra. Adapted from <http://www.physics.mq.edu.au>.

---

A combination of the absorbance and emission spectra is shown in Figure 7.66 for four different sized particles emitting green, yellow, orange, and red fluorescence.

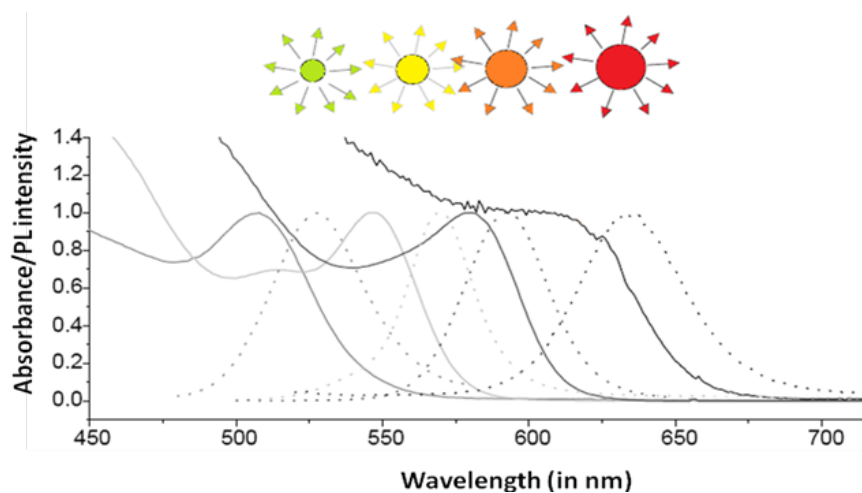


**Figure 7.66:** Absorption and emission spectra of CdSe quantum dots. Adapted from G. Schmid, *Nanoparticles: From Theory to Application*, Wiley-VCH, Weinham (2004).

#### 7.4.4.5.2 Cadmium telluride

Cadmium Telluride (CdTe) has a band gap of 1.44 eV and thus absorbs in the infra red region. The size evolving CdTe emission spectra is shown in Figure 7.67.

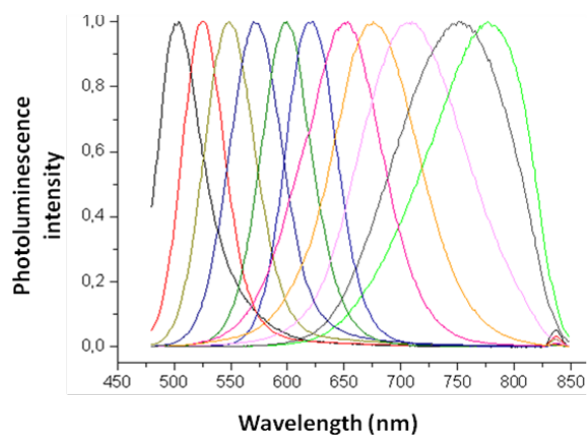


**Figure 7.67:** Size evolution spectra of CdTe quantum dots.

#### 7.4.4.5.3 Adding shells to QDs

Capping a core quantum dot with a semiconductor material with a wider bandgap than the core, reduces the nonradiative recombination and results in brighter fluorescence emission. Quantum yields are affected by the presences of free surface charges, surface defects and crystal defects, which results in unwanted recombinations. The addition of a shell reduces the nonradiative transitions and majority of the electrons relax radiatively to the valence band. In addition, the shell also overcomes some of the surface defects.

For the CdSe-core/ZnS-shell systems exhibit much higher quantum yield as compared to core CdSe quantum dots as seen in Figure 7.68.

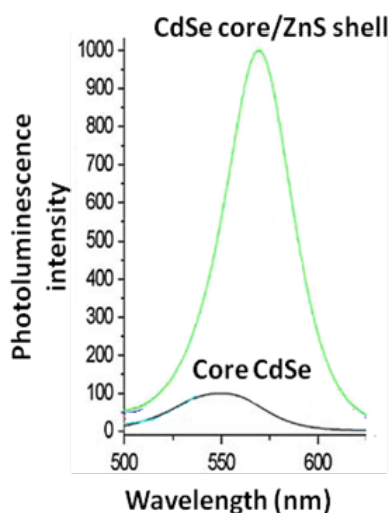


Figure 7.68: Emission spectra of core CdSe only and CdSe-core/ZnS-shell.

#### 7.4.4.6 Bibliography

- A. T. R. Williams, S. A. Winfield, and J. N. Miller, *Analyst*, 1983, **108**, 1067.
- G. Schmid, *Nanoparticles: From Theory to Application*, Wiley-VCH, Weinham, (2004).
- J. Y. Hariba, *A Guide to Recording Fluorescence Quantum Yield*, Jobin Yvon Hariba Limited, Stanmore (2003).
- C. Qing Zhu, P. Wang, X. Wang, and Y. Li, *Nanoscale Res. Lett...*, 2008, **3**, 213.

## 7.5 Measuring the Specific Surface Area of Nanoparticle Suspensions using NMR<sup>12</sup>

### 7.5.1 Introduction

Surface area is a property of immense importance in the nano-world, especially in the area of heterogeneous catalysis. A solid catalyst works with its active sites binding to the reactants, and hence for a given active site

<sup>12</sup>This content is available online at <<http://cnx.org/content/m34663/1.1/>>.

reactivity, the higher the number of active sites available, the faster the reaction will occur. In heterogeneous catalysis, if the catalyst is in the form of spherical nanoparticles, most of the active sites are believed to be present on the outer surface. Thus it is very important to know the catalyst surface area in order to get a measure of the reaction time. One expresses this in terms of volume specific surface area, i.e., surface area/volume although in industry it is quite common to express it as surface area per unit mass of catalyst, e.g.,  $\text{m}^2/\text{g}$ .

### 7.5.2 Overview of NMR

Nuclear magnetic resonance (NMR) is the study of the nuclei of the response of an atom to an external magnetic field. Many nuclei have a net magnetic moment with  $I \neq 0$ , along with an angular momentum in one direction where  $I$  is the spin quantum number of the nucleus. In the presence of an external magnetic field, a nucleus would precess around the field. With all the nuclei precessing around the external magnetic field, a measurable signal is produced.

NMR can be used on any nuclei with an odd number of protons or neutrons or both, like the nuclei of hydrogen ( $^1\text{H}$ ), carbon ( $^{13}\text{C}$ ), phosphorous ( $^{31}\text{P}$ ), etc. Hydrogen has a relatively large magnetic moment ( $\mu = 14.1 \times 10^{-27} \text{ J/T}$ ) and hence it is used in NMR logging and NMR rock studies. The hydrogen nucleus composes of a single positively charged proton that can be seen as a loop of current generating a magnetic field. It is may be considered as a tiny bar magnet with the magnetic axis along the spin axis itself as shown in Figure 7.69. In the absence of any external forces, a sample with hydrogen alone will have the individual magnetic moments randomly aligned as shown in Figure 7.70.

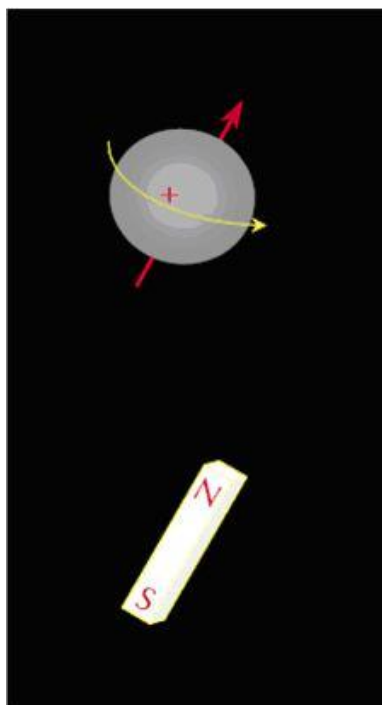


**Figure 7.69:** A simplistic representation of a spinning nucleus as bar magnet. Copyright: Halliburton Energy Services, Duncan, OK (1999).

---

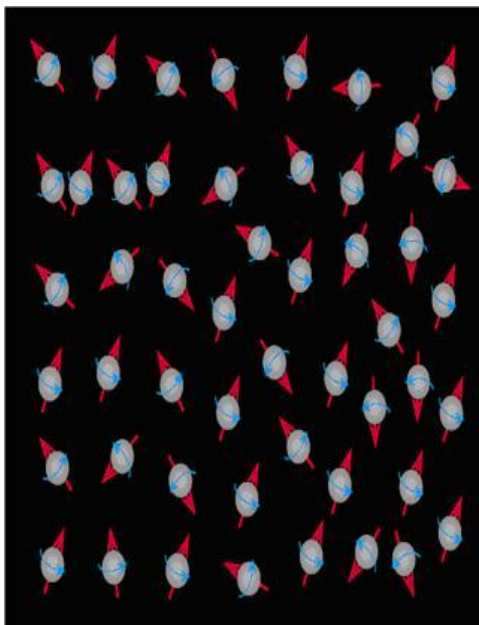


**Figure 7.70:** Representation of randomly aligned hydrogen nuclei. Copyright: Halliburton Energy Services, Duncan, OK (1999).

### 7.5.3 Advantages of NMR over BET technique

BET measurements follow the BET (Brunner-Emmet-Teller) adsorption isotherm of a gas on a solid surface. Adsorption experiments of a gas of known composition can help determine the specific surface area of the solid particle. This technique has been the main source of surface area analysis used industrially for a long time. However BET techniques take a lot of time for the gas-adsorption step to be complete while one shall see in the course of this module that NMR can give you results in times averaging around 30 minutes depending on the sample. BET also requires careful sample preparation with the sample being in dry powder form, whereas NMR can accept samples in the liquid state as well.

### 7.5.4 How does NMR work?

#### 7.5.4.1 Polarization

Polarization involves the alignment of the individual magnetic nuclei in the presence of a static external magnetic field  $B_0$ . This external field exerts a torque that forces the spinning nuclei to precess around it by a frequency given by the *Larmor frequency* given by (7.28), where  $\gamma$  is the gyromagnetic ratio which is a characteristic property of the nucleus. For hydrogen,  $\gamma/2\pi = 42.58$  MHz/Tesla. This value is different for different elements.

$$f = \frac{\gamma B_0}{2\pi} \quad (7.28)$$

Considering the case of a proton under the influence of an external magnetic field, it will be in one of two possible energy states depending on the orientation of the precession axis. If the axis is parallel to  $B_0$ , the

proton is in the lower energy state (preferred state) and in the higher energy state if anti-parallel shown by Figure 7.71.

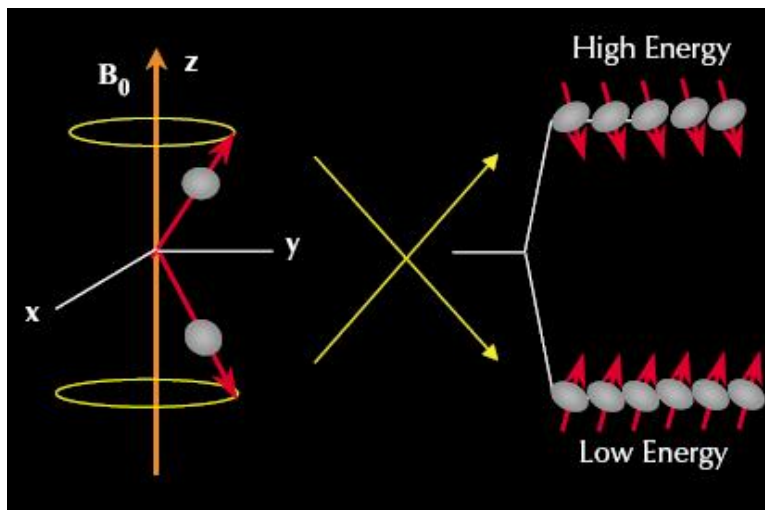


**Figure 7.71:** Alignment of precession axis. Copyright: Halliburton Energy Services, Duncan, OK (1999).

We define the net magnetization per unit volume of material,  $M_o$ , from Curie's law as (7.29), where  $N$  = number of protons,  $h$  = Planck's constant ( $6.626 \times 10^{-34}$  Js),  $I$  = spin quantum number of the nucleus,  $k$  = Boltzmann's constant ( $1.381 \times 10^{-23}$  m<sup>2</sup> Kg s<sup>-2</sup> K<sup>-1</sup>), and  $T$  = temperature (K)

$$M_o = \frac{N\gamma^2 h^2 I(I+1) B_o}{12\pi^2 kT} \quad (7.29)$$

#### 7.5.4.2 $T_1$ relaxation

The protons are said to be polarized completely once they are all aligned with the static external field. Polarization grows with a time constant called the *longitudinal relaxation time* ( $T_1$ ) as shown in (7.30), where  $t$  = time of exposure to  $B_o$ ,  $M_z(t)$  = magnitude of magnetization at time  $t$ , with  $B_o$  along  $z$ -axis and  $T_1$  = time at which  $M_z(t)$  reaches 90% of its final value, i.e.,  $M_o$ .

$$M_z(t) = M_o \left(1 - e^{-\frac{t}{T_1}}\right) \quad (7.30)$$

$T_1$  is the time at which  $M_z(t)$  reaches 63% of its final value,  $M_o$ . A typical  $T_1$  relaxation experiment involves application of a  $90^\circ$  RF pulse that rotates the magnetization to the transverse direction. With time, the magnetization returns to its original value in the same fashion described by the above equation.

Click on the video below to see the mechanism of  $T_1$  relaxation

[MEDIA OBJECT]<sup>13</sup>

<sup>13</sup>This media object is a video file. Please view or download it at

<T1\_Relaxation\_Video.wmv>

T<sub>1</sub> relaxation mechanism.

### 7.5.4.3 T<sub>2</sub> Relaxation

Once the polarization is complete, the magnetization direction is tipped from the longitudinal plane to a transverse plane by applying an oscillating field  $B_1$  perpendicular to  $B_0$ . The frequency of  $B_1$  must equal the Larmor frequency of the material from  $B_0$ . This oscillating field causes a possible change in energy state, and in-phase precession. The total phenomenon is called *nuclear magnetic resonance* as shown in Figure 7.72.

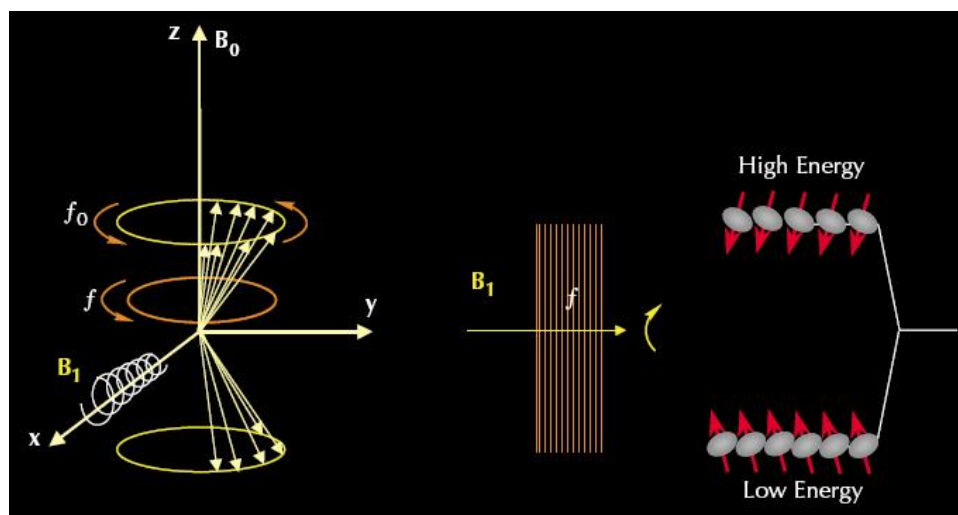


**Figure 7.72:** A schematic representation of the phenomenon of nuclear magnetic resonance. Copyright: Halliburton Energy Services, Duncan, OK (1999).

The oscillating field is generally pulsed in nature and so terms in books such as a 180° pulse or 90° pulse indicates the angle through which the net magnetization gets tipped over. Application of a 90° pulse causes precession in the transverse phase. When the field  $B_1$  is removed, the nuclei begin to de-phase and the net magnetization decreases. Here a receiver coil detects the decaying signal in a process called *free induction decay (FID)*. This exponential decay has an FID time constant ( $T_2$ ) which is in the order of microseconds.

The time constant of the transverse relaxation is referred as  $T_2$ , and the amplitude of the decaying signal is given by (7.31), with symbols as defined earlier.

$$M_x(t) = M_0 e^{-\frac{t}{T_2}} \quad (7.31)$$

Click on the video below to see the mechanism of  $T_2$  relaxation

[MEDIA OBJECT]<sup>14</sup>

T<sub>2</sub> relaxation mechanism.

<sup>14</sup>This media object is a video file. Please view or download it at

<T2\_Relaxation\_Video.wmv>

#### 7.5.4.4 CPMG sequence

The de-phasing caused by  $T_1$  relaxation can be reversed by applying a  $180^\circ$  pulse after a time  $\tau$  has passed after application of the initial  $90^\circ$  pulse. Thus the phase of the transverse magnetization vector is now reversed by  $180^\circ$  so that “slower” vectors are now ahead of the “faster” vectors. These faster vectors eventually over-take the slower vectors and cause rephasing which is detected by a receiver coil as a *spin echo*. Thus time  $\tau$  also passes between the application of the  $180^\circ$  pulse and the maximum peak in the spin echo. The entire sequence is illustrated in Figure 7.73. A single echo decays very quickly and hence a series of  $180^\circ$  pulses are applied repeatedly in a sequence called the *Carr-Purcell-Meiboom-Gill (CPMG) sequence*.

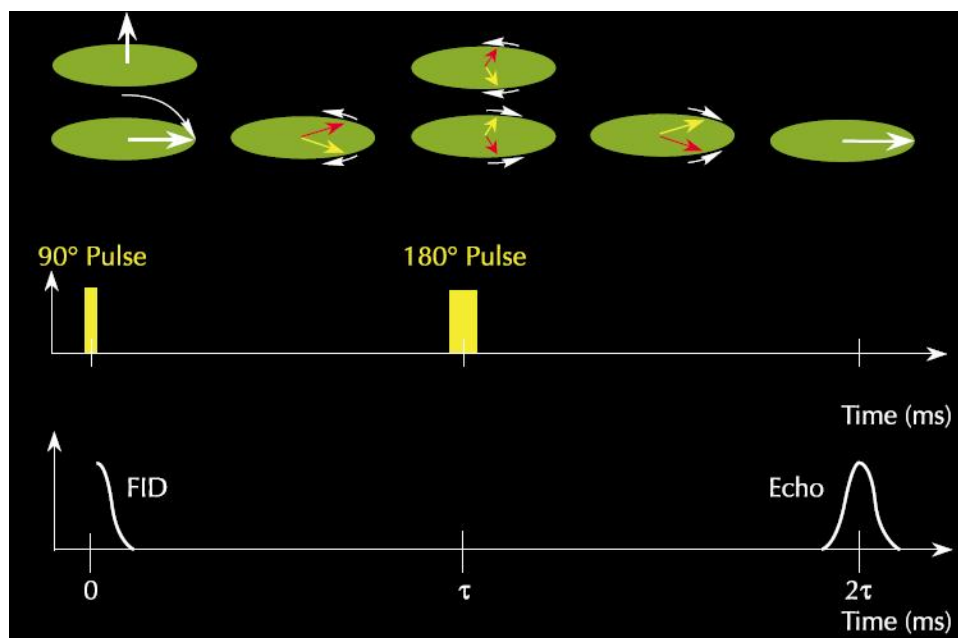


**Figure 7.73:** A schematic representation of the generation of a spin echo. Copyright: Halliburton Energy Services, Duncan, OK (1999).

### 7.5.5 NMR relaxation mechanism in solid suspensions

#### 7.5.5.1 Calculations

From an atomic stand point,  $T_1$  relaxation occurs when a precessing proton transfers energy with its surroundings as the proton relaxes back from higher energy state to its lower energy state. With  $T_2$  relaxation, apart from this energy transfer there is also dephasing and hence  $T_2$  is less than  $T_1$  in general. For solid suspensions, there are three independent relaxation mechanisms involved:-

- 1) Bulk fluid relaxation, which affects both  $T_1$  and  $T_2$  relaxation.
- 2) Surface relaxation, which affects both  $T_1$  and  $T_2$  relaxation.
- 3) Diffusion in the presence of the magnetic field gradients, which affects only  $T_2$  relaxation.

These mechanisms act in parallel so that the net effects are given by (7.32) and (7.33)

$$\frac{1}{T_2} = \frac{1}{T_{2,\text{bulk}}} + \frac{1}{T_{2,\text{surface}}} + \frac{1}{T_{2,\text{diffusion}}} \quad (7.32)$$

$$\frac{1}{T_1} = \frac{1}{T_{1,\text{bulk}}} + \frac{1}{T_{1,\text{surface}}} \quad (7.33)$$

The relative importance of each of these terms depend on the specific scenario. For the case of most solid suspensions in liquid, the diffusion term can be ignored by having a relatively uniform external magnetic field that eliminates magnetic gradients. Theoretical analysis has shown that the surface relaxation terms can be written as (7.34) and (7.35), where  $\rho$  = surface relaxivity and  $s/v$  = specific surface area.

$$\frac{1}{T_{1,\text{surface}}} = \rho_1 \left( \frac{S}{V} \right)_{\text{particle}} \quad (7.34)$$

$$\frac{1}{T_{2,\text{surface}}} = \rho_2 \left( \frac{S}{V} \right)_{\text{particle}} \quad (7.35)$$

Thus one can use  $T_1$  or  $T_2$  relaxation experiment to determine the specific surface area. We shall explain the case of the  $T_2$  technique further as (7.36).

$$\frac{1}{T_2} = \frac{1}{T_{2,\text{bulk}}} + \rho_2 \left( \frac{S}{V} \right)_{\text{particle}} \quad (7.36)$$

One can determine  $T_2$  by spin-echo measurements for a series of samples of known  $S/V$  values and prepare a calibration chart as shown in Figure 7.74, with the intercept as  $\frac{1}{T_{2,\text{bulk}}}$  and the slope as  $\rho_2$ , one can thus find the specific surface area of an unknown sample of the same material.

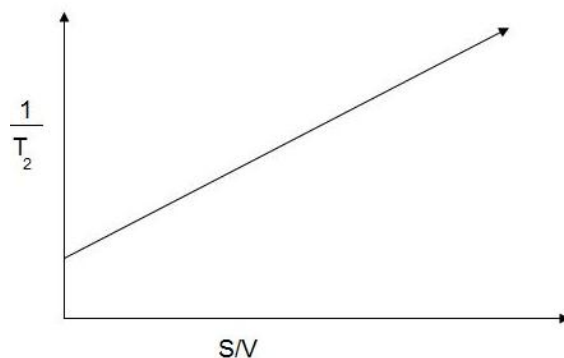


**Figure 7.74:** Example of a calibration plot of  $1/T_2$  versus specific surface area ( $S/V$ ) of a sample.

---

### 7.5.6 Sample preparation and experimental setup

The sample must be soluble in the solvent. For proton NMR, about 0.25-1.00 mg/mL are needed depending on the sensitivity of the instrument.

NOTE: The solvent properties will have an impact of some or all of the spectrum. Solvent viscosity affects obtainable resolution, while other solvents like water or ethanol have exchangeable protons that will prevent the observation of such exchangeable protons present in the solute itself. Solvents must be chosen such that the temperature dependence of solute solubility is low in the operation temperature range. Solvents containing aromatic groups like benzene can cause shifts in the observed spectrum compared to non-aromatic solvents.

NMR tubes are available in a wide range of specifications depending on specific scenarios. The tube specifications need to be extremely narrow while operating with high strength magnetic fields. The tube needs to be kept extremely clean and free from dust and scratches to obtain good results, irrespective of the quality of the tube. Tubes can be cleaned without scratching by rinsing out the contents and soaking them in a degreasing solution, and by avoiding regular glassware cleaning brushes. After soaking for a while, rinse with distilled water and acetone and dry the tube by blowing filtered nitrogen gas through a pipette or by using a swab of cotton wool.

Filter the sample solution by using a Pasteur pipette stuffed with a piece of cotton wool at the neck. Any suspended material like dust can cause changes in the spectrum. When working with dilute aqueous solutions, sweat itself can have a major effect and so gloves are recommended at all times.

NOTE: Sweat contains mainly water, minerals (sodium 0.9 g/L, potassium 0.2 g/L, calcium 0.015 g/L, magnesium 0.0013 g/L and other trace elements like iron, nickel, zinc, copper, lead and chromium), as well as lactate and urea. In presence of a dilute solution of the sample, the proton-containing substances in sweat (e.g., lactate and urea) can result in a large signal that can mask the signal of the sample.

The NMR probe is the most critical piece of equipment as it contains the apparatus that must detect the small NMR signals from the sample without adding a lot of noise. The size of the probe is given by the diameter of the NMR tube it can accommodate with common sizes 5, 10 and 15 mm. A larger size probe can be used in the case of less sensitive samples in order to get as much solute into the active zone as possible. When the sample is available in less quantity, use a smaller size tube to get an intrinsically higher sensitivity.

#### 7.5.6.1 NMR analysis

A result sheet of  $T_2$  relaxation has the plot of magnetization versus time, which will be linear in a semi-log plot as shown in Figure 7.75. Fitting it to the equation, we can find  $T_2$  and thus one can prepare a calibration plot of  $1/T_2$  versus  $S/V$  of known samples.

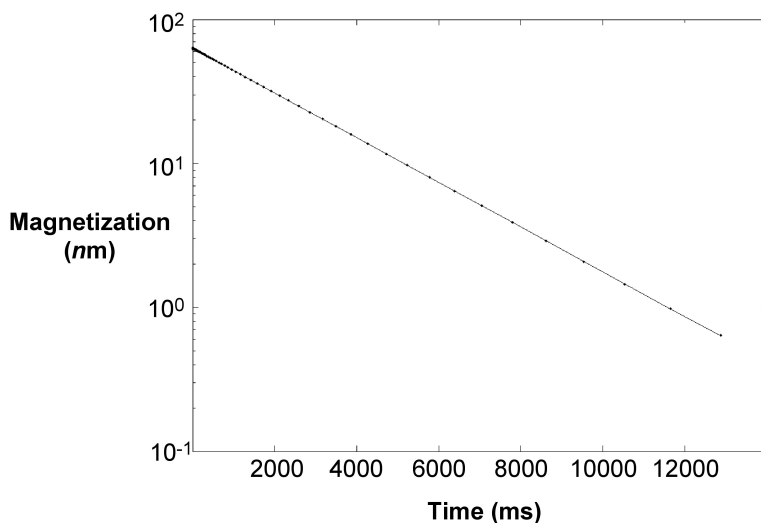


**Figure 7.75:** Example of  $T_2$  relaxation with magnetization versus time on a semi-log plot.

---

### 7.5.6.2 Limitations of the $T_2$ technique

The following are a few of the limitations of the  $T_2$  technique:

- One can't always guarantee no magnetic field gradients, in which case the  $T_1$  relaxation technique is to be used. However this takes much longer to perform than the  $T_2$  relaxation.
- There is the requirement of the odd number of nucleons in the sample or solvent.
- The solid suspension should not have any para- or ferromagnetic substance (for instance, organics like hexane tend to have dissolved  $O_2$  which is paramagnetic).
- The need to prepare a calibration chart of the material with known specific surface area.

### 7.5.6.3 Example of usage

A study of colloidal silica dispersed in water provides a useful example. Figure 7.76 shows a representation of an individual silica particle.

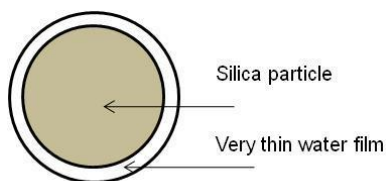


**Figure 7.76:** A representation of the silica particle with a thin water film surrounding it.

---

A series of dispersion in DI water at different concentrations was made and surface area calculated. The  $T_2$  relaxation technique was performed on all of them with a typical  $T_2$  plot shown in Figure 7.77 and  $T_2$  was recorded at 2117 milliseconds for this sample.

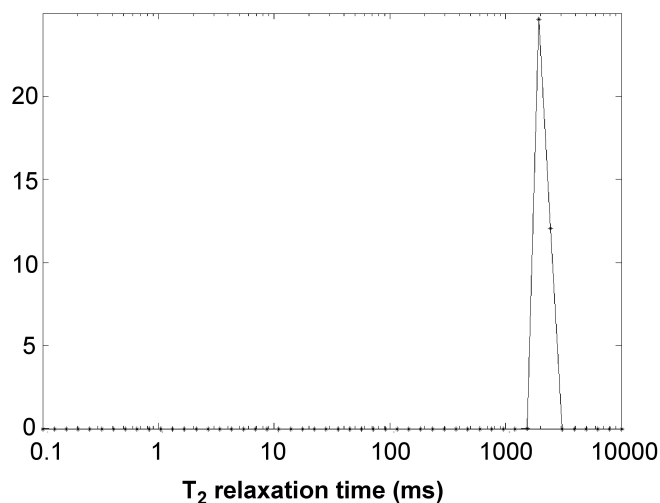


**Figure 7.77:**  $T_2$  measurement for 2.3 wt% silica in DI water.

---

A calibration plot was prepared with  $1/T_2 - 1/T_{2,\text{bulk}}$  as ordinate (the  $y$ -axis coordinate) and  $S/V$  as abscissa (the  $x$ -axis coordinate). This is called the *surface relaxivity plot* and is illustrated in Figure 7.78.

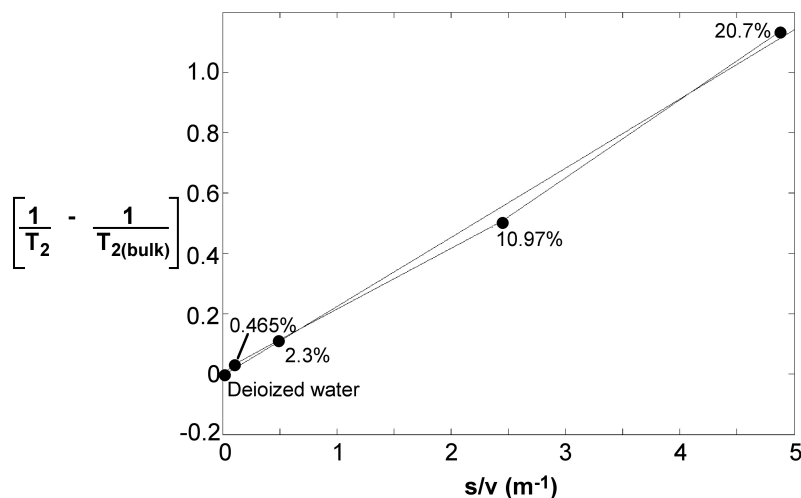


**Figure 7.78:** Calibration plot of  $(1/T_2 - 1/T_{2,Bulk})$  versus specific surface area for silica in DI water.

Accordingly for the colloidal dispersion of silica in DI water, the best fit resulted in (7.37), from which one can see that the value of surface relaxivity,  $2.3 \times 10^{-8}$ , is in close accordance with values reported in literature.

$$\frac{1}{T_2} - \frac{1}{T_{2,bulk}} = 2.3 \times 10^{-8} \left( \frac{S}{V} \right) - 0.0051 \quad (7.37)$$

The  $T_2$  technique has been used to find the pore-size distribution of water-wet rocks. Information of the pore size distribution helps petroleum engineers model the permeability of rocks from the same area and hence determine the extractable content of fluid within the rocks.

Usage of NMR for surface area determination has begun to take shape with a company, Xigo nanotools, having developed an instrument called the Acorn Area<sup>TM</sup> to get surface area of a suspension of aluminum oxide. The results obtained from the instrument match closely with results reported by other techniques in literature. Thus the  $T_2$  NMR technique has been presented as a strong case to obtain specific surface areas of nanoparticle suspensions.

### 7.5.7 Bibliography

- G. R Coates, L. Xiao, and M.G. Prammer, *NMR Logging: Principles & Applications*, Halliburton Energy Services, Houston (2001).
- B. Cowan, *Nuclear magnetic resonance and relaxation*, Cambridge University Press, Cambridge UK (2001).
- W. E. Kenyon, *The Log Analyst*, 1997, **6**, 2.
- A. E. Derome, *Modern NMR Techniques for Chemistry Research*, Vol 6, Pergamon Press, Oxford (1988).

## 7.6 Characterization of Graphene by Raman Spectroscopy<sup>15</sup>

### 7.6.1 Introduction

Graphene is a quasi-two-dimensional material, which comprises layers of carbon atoms arranged in six-member rings (Figure 7.79). Since being discovered by Andre Geim and co-workers at the University of Manchester, graphene has become one of the most exciting topics of research because of its distinctive band structure and physical properties, such as the observation of a quantum hall effect at room temperature, a tunable band gap, and a high carrier mobility.

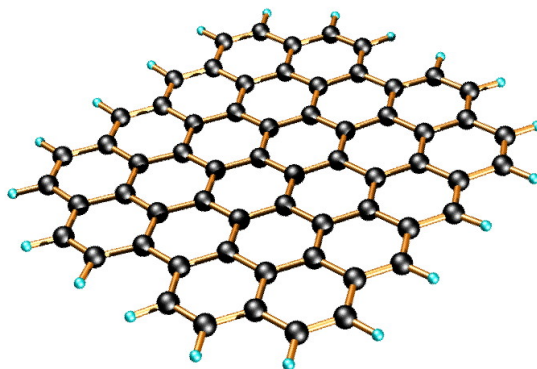


**Figure 7.79:** Idealized structure of a single graphene sheet.

Graphene can be characterized by many techniques including atomic force microscopy (AFM), transmission electron microscopy (TEM) and Raman spectroscopy. AFM can be used to determine the number of the layers of the graphene, and TEM images can show the structure and morphology of the graphene sheets. In many ways, however, Raman spectroscopy is a much more important tool for the characterization of graphene. First of all, Raman spectroscopy is a simple tool and requires little sample preparation. What's more, Raman spectroscopy can not only be used to determine the number of layers, but also can identify if the structure of graphene is perfect, and if nitrogen, hydrogen or other functionalization is successful.

### 7.6.2 Raman spectrum of graphene

While Raman spectroscopy is a useful technique for characterizing  $sp^2$  and  $sp^3$  hybridized carbon atoms, including those in graphite, fullerenes, carbon nanotubes, and graphene. Single, double, and multi-layer graphenes have also been differentiated by their Raman fingerprints.

shows a typical Raman spectrum of N-doped single-layer graphene. The D-mode, appears at approximately  $1350\text{ cm}^{-1}$ , and the G-mode appears at approximately  $1583\text{ cm}^{-1}$ . The other Raman modes are at  $1620\text{ cm}^{-1}$  (D'-mode),  $2680\text{ cm}^{-1}$  (2D-mode), and  $2947\text{ cm}^{-1}$  (D+G-mode).

<sup>15</sup>This content is available online at <<http://cnx.org/content/m34667/1.2/>>.

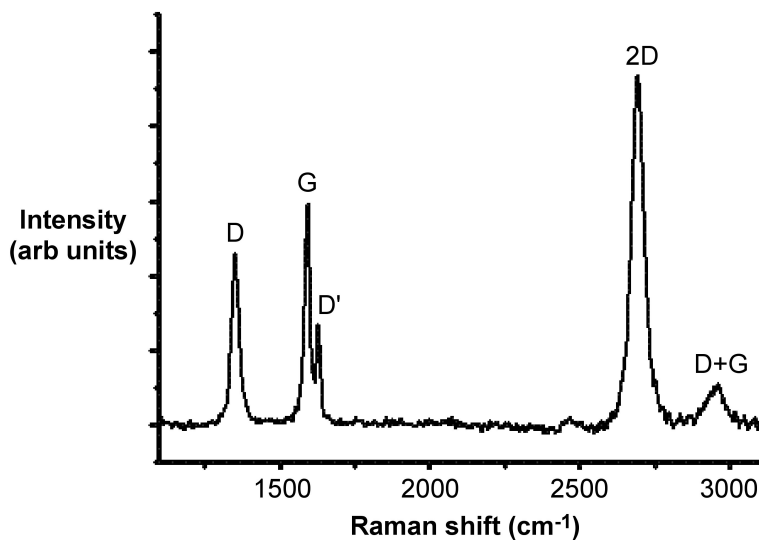


**Figure 7.80:** Raman spectrum with a 514.5 nm excitation laser wavelength of N-doped single-layer graphene.

---

### 7.6.2.1 The G-band

The G-mode is at about  $1583\text{ cm}^{-1}$ , and is due to E<sub>2g</sub> mode at the  $\Gamma$ -point. G-band arises from the stretching of the C-C bond in graphitic materials, and is common to all  $\text{sp}^2$  carbon systems. The G-band is highly sensitive to strain effects in  $\text{sp}^2$  system, and thus can be used to probe modification on the flat surface of graphene.

### 7.6.2.2 Disorder-induced D- band and D'- band

The D-mode is caused by disordered structure of graphene. The presence of disorder in  $\text{sp}^2$ -hybridized carbon systems results in resonance Raman spectra, and thus makes Raman spectroscopy one of the most sensitive techniques to characterize disorder in  $\text{sp}^2$  carbon materials. As is shown by a comparison of and , there is no D peak in the Raman spectra of graphene with a perfect structure.

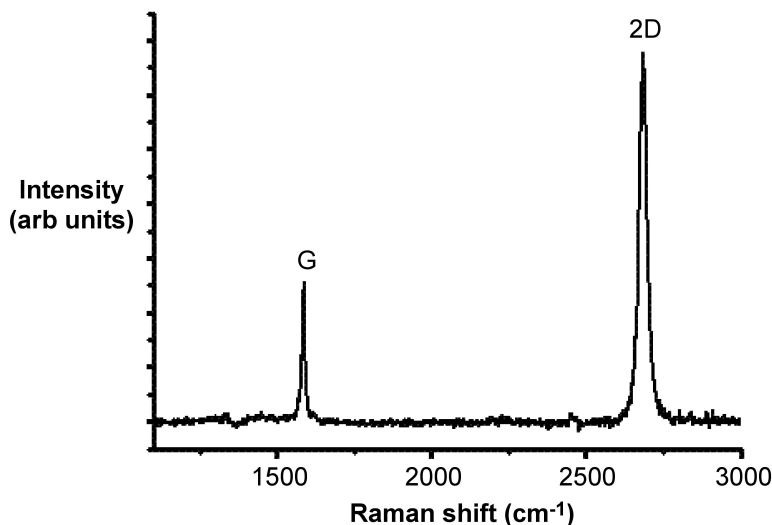


**Figure 7.81:** Raman spectrum with a 514.5 nm excitation laser wavelength of pristine single-layer graphene.

---

If there are some randomly distributed impurities or surface charges in the graphene, the G-peak can split into two peaks, G-peak (1583 cm<sup>-1</sup>) and D'-peak (1620 cm<sup>-1</sup>). The main reason is that the localized vibrational modes of the impurities can interact with the extended phonon modes of graphene resulting in the observed splitting.

### 7.6.2.3 The 2D-band

All kinds of sp<sup>2</sup> carbon materials exhibit a strong peak in the range 2500 - 2800 cm<sup>-1</sup> in the Raman spectra. Combined with the G-band, this spectrum is a Raman signature of graphitic sp<sup>2</sup> materials and is called 2D-band. 2D-band is a second-order two-phonon process and exhibits a strong frequency dependence on the excitation laser energy.

What's more, the 2D band can be used to determine the number of layer of graphene. This is mainly because in the multi-layer graphene, the shape of 2D band is pretty much different from that in the single-layer graphene. As shown in , the 2D band in the single-layer graphene is much more intense and sharper as compared to the 2D band in multi-layer graphene.

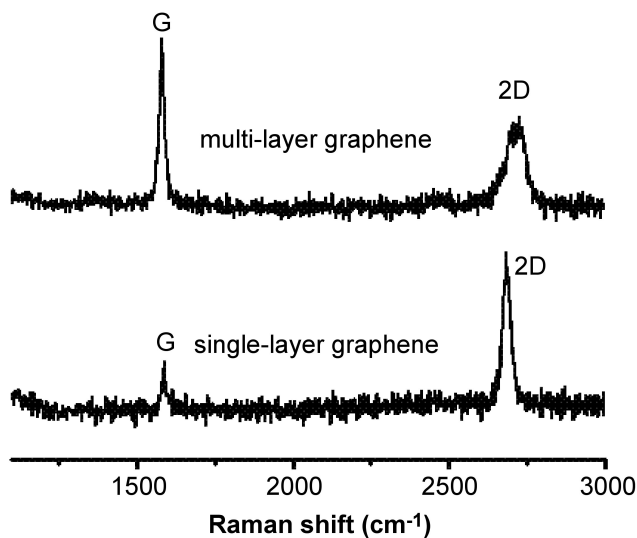


**Figure 7.82:** Raman spectrum with a 514.5 nm excitation laser wavelength of pristine single-layer and multi-layer graphene.

### 7.6.3 Bibliography

- G. G. Chen, P. Joshi, S. Tadigadapa, and P. C. Eklund, *Nano Lett.*, 2006, **6**, 2667.
- C. Ferrari, J. C. Meyer, V. Scardaci, C. Casiraghi, M. Lazzeri, F. Mauri, S. Piscanec, D. Jiang, K. S. Novoselov, and S. Roth, A. K. Geim, *Phys. Rev. Lett.*, 2006, **97**, 187401.
- M. A. Pimenta, G. Dresselhaus, M. S. Dresselhaus, L. A. Cancado, A. Jorio, and R. Sato, *Phys. Chem. Chem. Phys.*, 2007, **9**, 1276.

## 7.7 Characterization of Covalently Functionalized Single-Walled Carbon Nanotubes<sup>16</sup>

### 7.7.1 Introduction

Characterization of nanoparticles in general, and carbon nanotubes in particular, remains a technical challenge even though the chemistry of covalent functionalization has been studied for more than a decade. It has been noted by several researchers that the characterization of products represents a constant problem in nanotube chemistry. A systematic tool or suites of tools are needed for adequate characterization of chemically functionalized single-walled carbon nanotubes (SWNTs), and is necessary for declaration of success or failure in functionalization trials.

So far, a wide range of techniques have been applied to characterize functionalized SWNTs: infra red (IR), Raman, and UV/visible spectroscopies, thermogravimetric analysis (TGA), atomic force microscopy (AFM), transmission electron microscopy (TEM), X-ray photoelectron spectroscopy (XPS), etc. A summary of the attribute of each of the characterization method is given in Table 7.6.

<sup>16</sup>This content is available online at <<http://cnx.org/content/m22299/1.4/>>.



Method	Sample	Information	Limitations
TGA	solid	functionalization ratio	no evidence for covalent functionalization, not specific
XPS	solid	elements, functionalization ratio	no evidence of covalent functionalization, not specific, quantification complicated
Raman	solid	sp <sup>3</sup> indicated by D mode	not specific, quantification not reliable
Infra red (IR)	solid for (ATR-IR) or solution	substituent groups	no direct evidence for covalent functionalization, quantification not possible
UV/visible	solution	sidewall functionalization	not specific or quantitative, need highly dispersed sample
Solution NMR	solution	substituents	no evidence of covalent functionalization, high solubility of sample
Solid state NMR	solid	substituents, sp <sup>3</sup> molecular motions, quantification at high level of functionalization	high functionalization needed, long time for signal acquisition, quantification not available for samples with protons on side chains
AFM	solid on substrate	topography	only a small portion of sample characterized, no evidence of covalent functionalization, no chemical identity
<i>continued on next page</i>			

TEM	solid on substrate	image of sample distribution dispersion	only a small portion of sample characterized, no evidence of covalent functionalization, no chemical identity dispersion information complicated
STM	solid on substrate	distribution	no chemical identity of functional groups small portion of sample conductive sample only

**Table 7.6:** Common characterization methodology for functionalized SWNTs.

## 7.7.2 Elemental and Physical Analysis

### 7.7.2.1 Thermogravimetric analysis (TGA)

Thermogravimetric analysis (TGA) is the mostly widely used method to determine the level of sidewall functionalization. Since most functional groups are labile or decompose upon heating, while the SWNTs are stable up to 1200 °C under Ar atmosphere. The weight loss at 800 °C under Ar is often used to determine functionalization ratio using this indirect method. Unfortunately, quantification can be complicated with presence of multiple functional groups. Also, TGA does not provide direct evidence for covalent functionalization since it cannot differentiate between covalent attachment and physical adsorption.

### 7.7.2.2 X-ray photoelectron spectroscopy (XPS)

XPS confirms the presence of different elements in functionalized SWNTs. This is useful for identification of heteroatom elements such as F and N, and then XPS can be used for quantification with simple substituent groups and used indirectly. Deconvolution of XPS is useful to study fine structures on SWNTs. However, the overlapping of binding energies in the spectrum complicates quantification.

## 7.7.3 Spectroscopy

### 7.7.3.1 Raman spectroscopy

Raman spectroscopy is very informative and important for characterizing functionalized SWNTs. The tangential G mode (*ca.* 1550 – 1600  $\text{cm}^{-1}$ ) is characteristic of  $\text{sp}^2$  carbons on the hexagonal graphene network. The D-band, so-called disorder mode (found at *ca.* 1295  $\text{cm}^{-1}$ ) appears due to disruption of the hexagonal  $\text{sp}^2$  network of SWNTs. The D-band was largely used to characterize functionalized SWNTs and ensure functionalization is covalent and occurred at the sidewalls. However, the observation of D band in Raman can also be related to presence of defects such as vacancies, 5-7 pairs, or dopants. Thus, using Raman to provide evidence of covalent functionalization needs to be done with caution. In particular, the use of Raman spectroscopy for a determination of the degree of functionalization is not reliable.

It has been shown that quantification with Raman is complicated by the distribution of functional groups on the sidewall of SWNTs. For example, if fluorinated-SWNTs (F-SWNTs) are functionalized with thiol or thiophene terminated moieties, TGA shows that they have similar level of functionalization. However, their relative intensities of D:G in Raman spectrum are quite different. The use of sulfur substituents allow for gold nanoparticles with 5 nm in diameter to be attached as a “chemical marker” for direct imaging of the distribution of functional groups. AFM and STM suggest that the functional groups of thio-SWNTs are group together while the thiophene groups are widely distributed on the sidewall of SWNTs. Thus the difference is not due to significant difference in substituent concentration but on substituent distribution, while Raman shows different D:G ratio.

### 7.7.3.2 Infra red spectroscopy

IR spectroscopy is useful in characterizing functional groups bound to SWNTs. A variety of organic functional groups on sidewall of SWNTs have been identified by IR, such as COOH(R), -CH<sub>2</sub>, -CH<sub>3</sub>, -NH<sub>2</sub>, -OH, etc. However, it is difficult to get direct functionalization information from IR spectroscopy. The C-F group has been identified by IR in F-SWNTs. However, C-C, C-N, C-O groups associated with the side-wall functionalization have not been observed in the appropriately functionalized SWNTs.

### 7.7.3.3 UV/visible spectroscopy

UV/visible spectroscopy is maybe the most accessible technique that provides information about the electronic states of SWNTs, and hence functionalization. The absorption spectrum shows bands at *ca.* 1400 nm and 1800 nm for pristine SWNTs. A complete loss of such structure is observed after chemical alteration of SWNTs sidewalls. However, such information is not quantitative and also does not show what type of functional moiety is on the sidewall of SWNTs.

### 7.7.3.4 Nuclear magnetic resonance

NMR can be considered as a “new” characterization technique as far as SWNTs are concerned. Solution state NMR is limited for SWNT characterization because low solubility and slow tumbling of the SWNTs results in broad spectra. Despite this issue, there are still solution <sup>1</sup>H NMR reported of SWNTs functionalized by carbenes, nitrenes and azomethine ylides because of the high solubility of derivatized SWNTs. However, proof of covalent functionalization cannot be obtained from the <sup>1</sup>H NMR. As an alternative, solid state <sup>13</sup>C NMR has been employed to characterize several functionalized SWNTs and show successful observation of sidewall organic functional groups, such as carboxylic and alkyl groups. But there has been a lack of direct evidence of sp<sup>3</sup> carbons on the sidewall of SWNTs that provides information of covalent functionalization.

Solid state <sup>13</sup>C NMR has been successfully employed in the characterization of F-SWNTs through the direct observation of the sp<sup>3</sup>C-F carbons on sidewall of SWNTs. This methodology has been transferred to more complicated systems; however, it has been found that longer side chain length increases the ease to observe sp<sup>3</sup>C-X sidewall carbons.

Solid state NMR is a potentially powerful technique for characterizing functionalized SWNTs because molecular dynamic information can also be obtained. Observation that higher side chain mobility can be achieved by using a longer side chain length offers a method of exploring functional group conformation. In fact, there have been reports using solid state NMR to study molecular mobility of functionalized multi-walled carbon nanotubes.

## 7.7.4 Microscopy

AFM, TEM and STM are useful imaging techniques to characterize functionalized SWNTs. As techniques, they are routinely used to provide an “image” of an individual nanoparticle, as opposed to an average of all the particles.

### 7.7.4.1 Atomic force microscopy

AFM shows morphology on the surface of SWNTs. The height profile on AFM is often used to show presence of functional groups on sidewall of SWNTs. Individual SWNTs can be probed by AFM and sometimes provide information of dispersion and exfoliation of bundles. Measurement of heights along an individual SWNT can be correlated with the substituent group, i.e., the larger an alkyl chain of a sidewall substituent the greater the height measured. AFM does not distinguish whether those functional groups are covalently attached or physically adsorbed on the surface of SWNTs.

#### 7.7.4.2 Transmission electron microscopy

TEM can be used to directly image SWNTs and at high resolution clearly shows the sidewall of individual SWNT. However, the resolution of TEM is not sufficient to directly observe covalent attachment of chemical modification moieties, i.e., to differentiate between  $sp^2$  and  $sp^3$  carbon atoms. TEM can be used to provide information of functionalization effect on dispersion and exfoliation of ropes.

Samples are usually prepared from very dilute concentration of SWNTs. Sample needs to be very homogeneous to get reliable data. As with AFM, TEM only shows a very small portion of sample, using them to characterize functionalized SWNTs and evaluate dispersion of samples in solvents needs to be done with caution.

#### 7.7.4.3 Scanning tunneling microscopy

STM offers a lot of insight on structure and surface of functionalized SWNTs. STM measures electronic structure, while sometimes the topographical information can be indirectly inferred by STM images. STM has been used to characterize F-SWNTs gold-marked SWNTs, and organic functionalized SWNTs. Distribution of functional groups can be inferred from STM images since the location of a substituent alters the localized electronic structure of the tube. STM images the position/location of chemical changes to the SWNT structure. The band-like structure of F-SWNTs was first disclosed by STM.

STM has the same problem that is inherent with AFM and TEM, that when using small sample size, the result may not be statistically relevant. Also, chemical identity of the features on SWNTs cannot be determined by STM; rather, they have to be identified by spectroscopic methods such as IR or NMR. A difficulty with STM imaging is that the sample has to be conductive, thus deposition of the SWNT onto a gold (or similar) surface is necessary.

#### 7.7.5 Bibliography

- L. B. Alemany, L. Zhang, L. Zeng, C. L. Edwards, and A. R. Barron, *Chem. Mater.*, 2007, **19**, 735.
- J. L. Bahr and J. M. Tour, *J. Mater. Chem.*, 2002, **12**, 1952.
- M. S. Dresselhaus, G. Dresselhaus, and A. Jorio, *J. Phys. Chem. C*, 2007, **111**, 17887.
- A. Hirsch, *Angew. Chem. Int. Ed.*, 2002, **41**, 1853.
- M. Holzinger, J. Abraham, P. Whelan, R. Graupner, L. Ley, F. Hennrich, M. Kappes, and A. Hirsch, *J. Am. Chem. Soc.*, 2003, **125**, 8566.
- K. F. Kelly, I. W. Chiang, E. T. Mickelson, R. H. Hauge, J. L. Margrave, X. Wang, G. E. Scuseria, C. Radloff, and N. J. Halas, *Chem. Phys. Lett.*, 1999, **313**, 455.
- V. N. Khabashesku, W. E. Billups, and J. L. Margrave, *Acc. Chem. Res.*, 2002, **35**, 1087.
- F. Liang, L. B. Alemany, J. M. Beach, and W. E. Billups, *J. Am. Chem. Soc.*, 2005, **127**, 13941.
- D. Tasis, N. Tagmatarchis, A. Bianco, and M. Prato, *Chem. Rev.*, 2006, **106**, 1105.
- H-L. Wu, Y-T. Yang, C-C. M. Ma, and H-C. Kuan, *J. Polym. Sci. A. Polym. Chem.*, 2005, 6084.
- L. Zeng, L. Zhang, and A. R. Barron, *Nano Lett.*, 2005, **5**, 2001.
- L. Zhang, J. Zhang, N. Schmandt, J. Cratty, V. N. Khabashesku, K. F. Kelly, and A. R. Barron, *Chem. Commun.*, 2005, 5429.

